UNIVERSITÀ DEGLI STUDI DI TRENTO

DOCTORAL THESIS

Network identification via multivariate correlation analysis

Author:
Diana Elisa CHIARI

Supervisor:
Prof. Leonardo RICCI

A thesis submitted in fulfillment of the requirements for the degree of Doctor of Philosophy

in the

Atomic and Molecular Physics Group
Department of Physics

July 8, 2019

Declaration of Authorship

I, Diana Elisa CHIARI, declare that this thesis titled, "Network identification via multivariate correlation analysis" and the work presented in it are my own. I confirm that:

- This work was done wholly or mainly while in candidature for a research degree at this University.
- Where any part of this thesis has previously been submitted for a degree or any other qualification at this University or any other institution, this has been clearly stated.
- Where I have consulted the published work of others, this is always clearly attributed.
- Where I have quoted from the work of others, the source is always given. With the exception of such quotations, this thesis is entirely my own work.
- I have acknowledged all main sources of help.
- Where the thesis is based on work done by myself jointly with others, I have made clear exactly what was done by others and what I have contributed myself.

Signed: _____

Date: _____

UNIVERSITÀ DEGLI STUDI DI TRENTO

Abstract

Department of Physics

Doctor of Philosophy

Network identification via multivariate correlation analysis

by Diana Elisa CHIARI

In this thesis an innovative approach to assess connectivity in a complex network was proposed. In network connectivity studies, a major problem is to estimate the links between the elements of a system in a robust and reliable way. To address this issue, a statistical method based on Pearson's correlation coefficient was proposed. The former inherits the versatility of the latter, declined in a general applicability to any kind of system and the capability to evaluate cross–correlation of time series pairs both simultaneously and at different time lags. In addition, our method has an increased "investigation power", allowing to estimate correlation at different time scale–resolutions. The method was tested on two very different kind of systems: the brain and a set of meteorological stations in the Trentino region. In both cases, the purpose was to reconstruct the existence of significant links between the elements of the two systems at different temporal resolutions. In the first case, the signals used to reconstruct the networks are magnetoencephalographic (MEG) recordings acquired from human subjects in resting–state. Zero–delays cross–correlations were estimated on a set of MEG time series corresponding to the regions belonging to the default mode network (DMN) to identify the structure of the fully–connected brain networks at different time scale resolutions. A great attention was devoted to test the correlation significance, estimated by means of surrogates of the original signal. The network structure is defined by means of the selection of four parameter values: the level of significance α, the efficiency η_0, and two ranking parameters, R_1 and R_2, used to merge the results obtained from the whole dataset in a single average behavior. In the case of MEG signals, the functional fully–connected networks estimated at different time scale resolutions were compared to identify the best observation window at which the network dynamics can be highlighted. The resulting best time scale of observation was ~ 30 s, in line with the results present in the scientific literature. The same method was also applied to meteorological time series to possibly assess wind circulation networks in the Trentino region. Although this study is preliminary, the first results identify an interesting clusterization of the meteorological stations used in the analysis.

Contents

To Brian Netwrok, who stayed with me all the way through the writing of my thesis. Thank you for all the typos.

Chapter 1

Introduction

Everyday we experiment "relations" with the environment around us. We, as the rest of the world – or the universe – constantly interact with something or someone else in different ways. This happens regardless of who or what is involved in the "relation" and how it is defined.
Let us consider a system of many elements, or *agents*, that, in some way, interact with each other. Their relation establishes a sort of "connection" between the elements involved: it can be expressed as a direct contact, as a long–distance transmission and reception of signals, or as a causal–effect relation. It should be noted that every example just listed exhibits a certain level of "communication" between the two elements involved. However, a "relation" can be defined also in other ways that do not include an actual transmission of information. This can happen for example when two or more elements are triggered by the same underlying phenomenon. Consider to observe the behavior of a group of people getting the same airplane: they have not a direct interaction with each other, nor they communicate to the other passengers their intention to board the plane; nevertheless, at the opening of the gate everybody will join the queue. Even in this case, it is possible to say that these agents are related, or *linked*, even if by some external effect.
If we try to visualize these ideas in a diagram, the result is a *network* in which the elements of a system are represented by the *nodes* and their relations are summarized in graphical *links* between them. The study of system dynamics by means of a network representation is a powerful method to highlight the dependence of the various elements, to understand how the information is transmitted through the system and to infer its dynamics even if a full mathematical representation is too heavy.
This last situation occurs true when the system contains a great amount of elements, mutually dependent, interacting in a non–trivial way. These kind of systems are known as *complex systems* and are present in every field of science and in everyday life: any living thing, for examples, is a complex system, consisting of other complex systems, as the organs and, at a simpler level, the cells. Moreover, such living being can be part of larger complex systems, as the ecosystem in which it lives.
In many complex systems it is easy to identify the interacting elements and the connections between them, in particular when they are "physical": one could think, for example, at the transportation systems – railways, roads, etc – that link together towns and cities. Same goes for a computer network in which the PCs are connected by cables. However, there are other cases in which the elements are still well–defined but their relations are less evident: this is the case of metabolic pathways and protein interaction networks, where the interactions are given by chemical reactions. One can think of planetary systems, where the elements are related one to the other by the gravitational attraction. Finally, there are even more complicated examples, as systems in which neither the nodes nor the links are clearly defined, as in the case of the climate, or systems that show more of these configurations together. This is

the case of the brain which can be observed both from an anatomical point of view, looking at the physical neural patterns connecting different brain regions, and from a functional point of view, when the links are defined on the basis of the synchronized activity of spatially separated cerebral areas (see Paragraph 1.2.2).
In general, the major issue in the study of complex systems is the identification of the links between the nodes. The minimum requirement is to understand which nodes are related and according to which kind of relation, but it is possible to extract other information, as the strength of the links and their direction (i.e. the direction of the information flux).
One of the most distinctive features of a complex system is the amount of "levels" at which it can be studied. Different networks can correspond to the same complex system, depending on the measured observable, the resolution used (*spatial* or *temporal*) and the method chosen to estimate the relations.
Because of this great amount of parameters to set, it is reasonable not to have a one–to–one relation between a system and the corresponding network. However, in order to understand which of these networks are really representative of the system dynamics, it is of major importance to provide reliable statistical tools to obtain robust results in terms of the network structure. This is precisely the framework of this thesis.

1.1 Problem definition

As previously mentioned, to understand the dynamics of a complex system we observe the time evolution of one, or more, of its characteristic physical observable. This is performed by collecting *signals* produced by the elements of the system. In tracking the system evolution at any given moment, a certain value of the observable corresponds to each node location. To better understand this point, we can use a simple example of a complex system. Let us consider a platform held up by pistons having the role to maintain the surface perfectly horizontal, regardless observable measured is the weight in every node location. According to the measured weight, the pistons react with a proper hydraulic push to preserve the platform position. To understand the dynamics of the system, we can observe the reaction of each piston in time. This information is collected in the form of *time series*, one for each node. The analysis of the system time series allows to understand how the elements are related to each other and how their interaction evolves in time. There are a lot of statistical tools to assess connectivity and what they do, in different ways, is to estimate the *similarity* level between the recorded signals: the more the nodes' behavior is similar, the more the nodes will be related. Their similarity can be defined in terms of the correlation or the coherence of their behavior.
As stated above, the framework, and thus the purpose, of this thesis is to widen the set of statistical methods to assess connectivity. The method described here is based on the Pearson's correlation, which addresses the issue of assessing connectivity in a particularly robust way. As an extension of Pearson's correlation, it inherits two main characteristics: its general applicability and its ability to compare the behavior of two time series both *simultaneously* (*zero–delay* cross–correlation) and by considering a time shift (or *lag*) between the two.
In this thesis two main fields of application will be described, whose choice has been performed on the basis of the research interests of the group in which I have worked. No limitation prevent to apply the same approach to any other kind of system. We decided to investigate only zero–delayed correlations, which, in particular

for brain connectivity analysis, allow a better comparability with the results present in the literature. However, further developments of this research could exploit the information provided by a time–lagged analysis.
In addition to the two characteristics previously mentioned, the innovative aspect of the method developed in this thesis consists in studying another fundamental aspect in the assessment of the network structure: the *temporal resolution* at which the network dynamics is observed.
In the following paragraph, I am going to explain why this aspect is so crucial in the network identification.

1.1.1 Time scale resolution

At the beginning of this discussion, I highlighted as, for the same system, it is possible to identify different network structures depending on what characteristic is observed and in which conditions. In this paragraph, I wish to focus on the differences resulting from the choice of the time resolution at which the system is analyzed.
Once again, I am using an example for the sake of simplicity. Let us consider two train stations of two big cities, not necessarily connected to each other. Then, let us monitor the number of passengers passing through the stations at different moments during the day, for a week, assuming to sample the amount of people every five minutes. If we compare contemporary short segments (for example, half an hour) of the two series of acquisitions we will not see any particular similarity between the flux of passengers through the two stations during the observation period. Hence, they result to be not correlated. However, progressively increasing the time interval of observation up to a whole day, it would be possible to identify two peaks in the influx of people through the stations corresponding to the opening and closing hours of the offices. By using this time window, the dynamics of the two systems is much more similar than in the previous case and they can be considered *linked* from a network point of view.
On the other hand, we can decide to monitor the same stations for 10 years, assuming that the two cities – referred to as $C1$ and $C2$ – have been developed in different ways: for example, $C1$ has increased the number of its activities only in the last two years, whereas $C2$ has been a thriving city since twenty years. If we compare the dynamics of the two cities, in terms of people flow through their stations, over the entire period of ten years, we are likely not to observe the same similarities as in the previous case, because they share an analogous behavior only in a short period of time.
As described by this example, the choice of the correct time interval – or *temporal resolution* – Δt to observe the behavior of a system is crucial: if Δt is too small or too large with respect to the period T that characterizes the network dynamics, one could wrongly infer that no relation exists between two or more elements of the set. However, the assessment of the best temporal resolution that outlines the evolution of the network is not a trivial question. For this reason, the method described in this thesis is of particular interest, since it performs a multivariate correlation analysis of the system time series by means of multiple time scale resolutions. This allows for testing two aspects: the best time window to observe the emerging dynamics of the network and whether the resulting network structure is stable according to the choice of Δt.
It should be pointed out that the study of a network at different time scales does not aim at predicting its *evolution*, but rather allows us to look at it from different

perspectives: it is something similar to what happen in photography, when one takes a close–up shot, a full shot or a long shot of the same subject.

1.2 Application fields

In this general overview, I tried to give the research framework in which this thesis is enclosed and the main ideas that justify its contribution. From now on I narrow down the description to the investigation fields in which our method was tested.
A major attention is given to what, up to now, has been the favorite application of the method developed: the reconstruction of *functional brain networks* during *resting–state*, as it will be soon explained in details. The paragraphs from 1.2.1 to 1.2.3 are not intended to be a comprehensive neuroscientific essay: they should give the most relevant elements to better understand the discussion developed in the rest of this thesis, the meaning of the obtained results and possible future applications.
At the end of this introductory discussion, I will briefly mention the second field of application discussed in this thesis, namely climatic networks (see Chapter 6).
I then start from the most studied – and probably least understood – complex network: the *human brain*.

1.2.1 The Human Brain

The brain is the most important organ of the central nervous system in human beings and it is able to process, integrate and manage the information collected by the sense organs. Although it consists of many parts, the cerebral cortex is the area of major interest for brain connectivity analysis, in particular the grey matter that is its outermost region – the nearest to the skull – and contains the majority of the neural bodies and synapses (see Section 3.1.2), namely the main elements involved in neural communication.
Signaling between neural populations produces *brainwaves*: they are macroscopic oscillations in the signals originated by the synchronized activity of groups of neurons and are detectable by acquisition systems sensitive to different physical properties, as electroencephalography (EEG), magnetoencephalography (MEG) and functional magnetic resonance imaging (fMRI). The frequency content of these waves is distributed over a broad range spanning from 0.01 Hz to 1000 Hz, but it is usually classified into bands of interest known as delta (0.01–4 Hz), theta (4–8 Hz), alpha (8–13 Hz), beta (13–30 Hz), and gamma (30–200 Hz) [12, 53]. The functional role of these neural oscillations is still not completely understood although they are present in all animal brains. Most hypotheses about their function suggest that they enhance the communication and information transfer efficiency between groups of neurons or functional networks [12].

1.2.2 Functional connectivity

In the first section of this introductive chapter, I said that there are many ways in which nodes and links of a complex network can be defined, depending on the characteristics of the system itself and what one needs to investigate. The brain is a particularly well–suited example in this sense: it is possible to examine its physical structure and the statistical interdependencies between distinct areas of activation. In the first case, the aim is to reconstruct the anatomical links between various regions of the brain; in the second case, one investigates the *functional connectivity* between different – and possibly distant – brain areas showing a correlated activity:

in other words, regions A and B are functionally connected if they activate together to perform a task. In addition, the *effective connectivity* can also be observed: the link existence between two regions is related to the causal dependence of their activation (region B activates as a consequence of the activation of region A). This definition implies a directionality of the link between the two areas.
This thesis only focuses on the analysis of functional connectivity.
An important characteristic of the brain cortex is that it is organized in functionally segregated regions devoted to specific functions, for example specialized in motor or perceptual processing. However, brain functional connectivity is even more structured, since spatially separated brain regions can cooperate in an integrated way to perform complex tasks.
By means of brain imaging techniques, in particular the functional magnetic resonance imaging (fMRI), it has been possible to highlight which areas activate when a task is executed: this allows to identify both the role of specific regions of the cortex and the functional networks that emerge in response to a stimulus.
It is not completely understood how structural, functional and effective networks are related to each other. The processing of the information and the remote control of distant regions is likely managed at a microscopic level, in terms of bindings between cell assemblies. Despite this, a strict correlation has not yet be found between the anatomical structures and the functional network patterns.
To assess the different kind of connectivity, three kind of imaging techniques are mainly used: the diffusion–weighted magnetic resonance imaging (DW–MRI) for the anatomical structure and the fMRI and MEG to investigate functional and effective connectivity.
The brain has developed a wide range of functional networks to perform different tasks. However, also when it has simply to stay still, it has to be tonically reactive to an external stimulus. This state is also achieved through functional networks, known as *resting state networks*, described in the next paragraph.

1.2.3 Resting State Networks and Default Mode Network

One of the most widely used approaches to understand the functional connectivity of the brain is to observe its spontaneous activity during a resting state. The *resting state* is defined as the condition of stillness while being awake of a subject who does not perform any task.
In 1995, Biswal [7] was the first to discover the existence of an organized brain activity during resting states. In his analysis, he recorded a fMRI acquisition of a subject, asking him to simply enter the scanner and do nothing. Surprisingly, instead of observing a spontaneous and random neural noise, he visualized a pattern of slow synchronized fluctuations of the blood–oxygen level dependent signal (the BOLD signal measured by fMRI, as explained in details in Section 3.5.1) [68]. Such synchronization patters involved regions that are known to cooperate and were recognizable in other subjects undergoing the same scanning procedure. However, Raichle *et al.* [63] were the first who talked of the existence of a new, unknown, brain network, the Default Mode Network (DMN). DMN was the first recognized resting–state network and it was defined as a "baseline state of normal adult brain". It has a leading role from both a physiological and scientific point of view: the neuroscientific community has given a great attention to DMN as a key element to understand brain connectivity.
The DMN is a conscious resting state, which seems to deal with autobiographical memory, introspective thinking, and future planning. It has the important role of a

central hub, managing the cross–communication between the functional brain networks. Although DMN formally represents a state of "idleness" of the subject observed, it is a fully–fledged active state of the brain, that consumes only 5% less of energy compared to a task–solving state. It is a sort of "reactive stand–by" that from a state of rest rapidly switches the brain to an operative state in response to a stimulus [63].
Following the definition by Raichle *et al.* [63] and Gusnard and Raichle [31], the brain physiological baseline corresponds to a lack of activation of a brain region, where "*activation*" is defined as a blood flux increase in that area [31]. During awake resting–state, the brain exploits the 11% of the cardiac output and justifies the 20% of the overall oxygen consumption in the body, despite representing just the 2% of the total weight [31, 63]. A possible reason for such a large amount of energy consumption during rest is that at least the 50% of that energy is used to comply with functional aspects of synaptic transmission [31]. The default functionality of brain baseline is spontaneous and lasts until the brain is involved in a task.
Since its first observation, DMN was mainly studied by means of fMRI, leading to the identification of the most important regions involved in the network. Despite a certain level of variability – across–subject and inter–subject – in the number and kind of brain areas belonging the network, it is possible to single out the functional areas that represent its core constituents. The most important are the posterior cingulate cortex (PCC) and the medial prefrontal cortex (MPFC): PCC is particularly involved in human awareness, attention and memory, whereas MPFC deals with decision making and complex cognitive behaviors.
In addition to DMN, many other resting–state networks (RSNs) have been identified, related to vision, hearing, sensor–motion, and memory. Their typical frequencies are in the order of $\sim 0.01 - 0.1$ Hz [12].
The results obtained in the analysis of resting state connectivity turned out to be very robust against different conditions and subjects, assessing that the human brain is not "inert" or "switched off" in absence of stimuli or tasks. A deep knowledge about brain functionality in resting state is fundamental to understand the impact of some diseases as strokes, or the development of some neurodegenerative pathologies as Alzheimer.
In the early stages of brain connectivity studies, fMRI was the most used technique laying the foundation for any further research. However, more recently the magnetoencephalography (MEG) has given a great contribution in this field thanks to the impressive temporal resolution compared to fMRI, that allows to obtain information about the dynamics of these networks. In the works of de Pasquale *et al.* [17, 55] the authors proposed that the apparent stationarity of the RSNs conceals a more complex non–stationary dynamics. The MEG allows to unveil the temporal and frequency properties of resting state networks while being able to preserve the fundamental topological structure identified by fMRI.

1.2.4 The climate network

As previously mentioned, the statistical method developed in this thesis has a general applicability. Besides resting state network in brain, the other context in which it was tested is the analysis of climate networks. Lorenz in 1963 was the first who described the climate as a complex system [44], but it was only in 2006 that Tsonis *et al.* in their seminal work [78] proposed the complex network approach to model climate dynamics. Also in this field, the standard statistical methods to estimate the

links – and thus, the network structure – aim at assessing the level of similarity between nodes behavior, as explained in details in Chapter 6. The decision to apply our method is justified by the Pearson's cross–correlation being widely used in the scientific literature for the assessment of climate network structures. On the other hand, to our knowledge, no other work addresses the issue to estimate correlation at different temporal resolution. Further extensions of our analysis could then lead to interesting developments in this research field. Chapter 6 provide an extensive report of the preliminary results obtained from wind intensity recordings in the region of Trentino.

1.3 Structure of the present thesis

In order to smooth the reading of this thesis, I provide here a short description of the topics of the following chapters. In Chapter 2 I describe some of the most important statistical methods in time series analysis, with a particular attention to those used in this work. Chapter 3 is devoted to a general overview of magnetoencephalography (MEG) in terms of the biological origin of the MEG signal, the acquisition system, the signal pre–processing and the source–space reconstruction. Then, the core of this manuscript follows: in Chapter 4 the reader can find a detailed explanation of the new method developed during my PhD to estimate the zero–delay cross–correlation of a complex system, while in Chapter 5 the step–by–step description of the algorithm of network reconstruction and the results obtained in functional connectivity are reported. In Chapter 6, I conclude the discussion with a preliminary application of the method to another field of research, the climate network. A summary of the results obtained and possible future perspectives can be found in the Conclusions.

Chapter 2

Methods

In the study of physical phenomena and human activities, the first requirement is to collect data. If we want to analyze the temporal evolution of a phenomenon or a system, the most efficient way is to identify one or more physical dimensions of interest and collect a sequence of observations, temporally ordered and equally spaced in time. This way to arrange data is known as *time series*. Time series have a widespread use in almost every field of knowledge and their analysis has the main goal to describe the underline phenomenon producing such signals. This is performed by the extraction of meaningful statistics and other characteristics of the data.
The goal of the present chapter is to provide an overview of the conventional methods used in the framework of network dynamics.

2.1 Time and frequency domain

A physical process can be described in *time domain*, by observing how the value of a certain quantity varies as a function of time ($h(t)$). Conversely, it can be observed in *frequency* or *spectral domain*, where the process is described by its amplitude in function of frequency ($H(f)$). The two forms $h(t)$ and $H(f)$ can be considered as two representations of the same function. It is possible to switch to one form to the other by using the Fourier transform that decomposes a signal in its constituent frequencies. In continuous form, the Fourier transform is expressed as:

$$H(f) = \int_{-\infty}^{\infty} h(t) e^{-2\pi i f t} dt \,, \tag{2.1}$$

whereas the inverse transformation from frequency to time domain is given by:

$$h(t) = \int_{-\infty}^{\infty} H(f) e^{2\pi i f t} df \,. \tag{2.2}$$

In the event that the time series is periodic, it is possible to evaluate the Fourier transform over a finite interval rather than from $-\infty$ to ∞, where the interval usually corresponds to the fundamental period of the signal.
Unfortunately, in most real cases, we do not manage continuous functions, but rather finite sequences of experimental data, inherently discrete, because sampled at discrete time intervals.
In this case, a discrete form of this transformation exists, with the self–explanatory name of Discrete Fourier Transform (DFT), equivalent in concept to the continuous form, that is expressed as:

$$H(f) = \sum_{k=0}^{N-1} h_k e^{-2\pi i f \Delta} \,, \tag{2.3}$$

where Δ is the sampling time.
As previously mentioned, the continuous form of the Fourier transform can be evaluated over a finite interval when the signal is periodic: the same approach is applied for the DFT that, handling with finite time series of length N, assumes that they are periodic with period N (i.e. $f(N)$ to $f(2N-1)$ is the same as $f(0)$ to $f(N-1)$). It follows that the DFT is evaluated for the fundamental frequency $(1/NT)$ and its harmonics and Eq. 2.3:

$$H(f) = \sum_{k=0}^{N-1} h_k e^{-2\pi i \frac{n}{N} k} \,. \tag{2.4}$$

2.1.1 Signal acquisition, Nyquist-Shannon theorem and the aliasing problem

As previously described, when a signal is sampled, the sampling frequency corresponds to the inverse of the time interval Δ between to successive samples. The correct sampling rate choice is not a mundane question. According to the *sampling theorem*, the minimum sampling frequency to correctly reconstruct the signal (i.e. avoiding *aliasing*) is the Nyquist critical frequency. The theorem says that, if a function $h(t)$, sampled every Δ, is bandwidth limited to frequencies less than a certain f_c, then the function $h(t)$ is completely defined by its h_n samples:

$$h(t) = \Delta \sum_{n=-\infty}^{\infty} h_n \frac{\sin(2\pi f_c(t - n\Delta))}{\pi(t - n\Delta)} \,, \tag{2.5}$$

where f_c is the Nyquist critical frequency, that is defined as:

$$f_s \equiv \frac{1}{2\Delta} \,. \tag{2.6}$$

Problems occur when continuous functions that are not bandwidth–limited are sampled at a frequency less than the critical one: all the power spectral density due to frequencies f ($|f| \geq f_s$) are spouriously moved into the range $-f_s < f < f_s$. This phenomenon is known as *aliasing*. One of the possible ways to avoid aliasing is to know the natural bandwidth limit of the signal or to impose a known limit by means of an analog filter of the continuous function. Otherwise, we have to sample the signal at a sufficiently high rate to have at least two points for each period of the highest frequency present. To verify the sampling accuracy it is enough to check whether the Fourier transform of the signal approaches zero at the sampling frequency. If it does not, the chances are that frequencies components outside the critical range have been folded inside.

An important issue one has to take into account when time series analysis is performed is the *stationarity* of the signal analyzed. Although it is not the proper place to extensively discuss such a huge problem, it is useful to know some details about how stationarity is defined. This is an important question since many statistical tests require that the analyzed signals are stationary in order to give reliable results.

Stationarity, Weak Stationarity and Non–stationarity

There are two possible definition of stationarity: the *strict* or *strong* stationarity and the *wide–sense* or *weak* stationarity.

Given a stochastic process $\{x(t)\}$, it is defined as strongly stationary if its statistical properties do not depend on time, or, in other words, if its joint probability distribution does not change if shifted in time [83]:

$$\{X_{t_1}, X_{t_2}, \ldots, X_{t_n}\} = \{X_{t_1+k}, X_{t_2+k}, \ldots, X_{t_n+k}\}, \quad \forall k, t_1, \ldots, t_n \in \mathbb{R} \text{ and } n \in \mathbb{N}. \tag{2.7}$$

On the other hand, the weak stationarity has a less strict definition: a stochastic process $\{x(t)\}$ is weakly stationary if its first and second moments exist and are independent on time. Moreover its autocorrelation has to depend only on the relative time delay (see Paragraph 2.2.1 for further details).
The determination of the stationarity of a time series is not a minor issue: a lot of works have been devoted to this problem [3, 42, 72, 83] without achieving an unambiguous answer.

2.2 Assessing connectivity

In the literature, it is possible to find plenty of methods developed to quantify the level of similarities between a pair (or more) time series for connectivity analysis. The aim of these techniques is to quantify the statistical interdependence directly from the data. To do this, the most common methods estimates similarities between signals on the basis of their amplitude or phase. Let us take MEG signals as an example, since it is the main field of application of this thesis: the most used statistical methods to assess connectivity are power correlations, mutual information, coherence, phase locking, independent component analysis and many others. In this case, the resulting functional connectivity is not easy to correctly understand: the results are sensitive to modifications of the external conditions (as the different level of signal–to–noise ratio or changes in some locations of a larger network) even though there are not real modifications in neural connectivity [12].
In the following, I will describe some examples of such methods, with a particular attention to those connected with this thesis work. It is not in the scope of this thesis to provide a comprehensive overview of the topic, for which Ref. [12] is suggested.

2.2.1 Linear metrics

Correlation

Correlation is the most straightforward linear metrics to estimates the statistical relationship between two MEG series. Let us consider two stochastic processes $x(t)$ and $y(t)$: the statistical measure that quantifies the level of *similarity* between the two series is known as correlation or *cross–correlation*: it is estimated by directly superimposing the two functions shifted one with respect to the other of a certain time lag t. It follows that the cross–correlation between two continuous functions $x(t)$ and $y(t)$ is a function of the lag t:

$$Corr(x,y)(t) = E[(x_\tau - \mu_{x_\tau})(y_\tau - \mu_{x_\tau})]. \tag{2.8}$$

In general, it is much more convenient to use the normalized form of the correlation (corresponding to the Pearson's correlation coefficient, as explained in the next paragraph), expressed as:

$$Corr(x,y)(t) = \frac{E[(x_\tau - \mu_{x_\tau})(y_\tau - \mu_{x_\tau})]}{\sigma_{x_\tau}\sigma_{y_\tau}}. \tag{2.9}$$

where σ_{x_τ} and σ_{y_τ} are the standard deviations of the two random variables x_τ and y_τ. In this case, the values span between -1 and 1: when $Corr(x, y) \approx 0$, it corresponds to the absence of correlation between the two series. On the other hand, if the correlation term is near 1, the two functions are highly correlated: it means that they are similar, or, given a lag t, they are close copies but shifted by a certain lag. Finally, if the correlation is close to -1 the two time series are highly anticorrelated, according to a proper time lag.
The positive or negative temporal displacement t of the two functions is indifferent, thus it holds:

$$Corr(x, y)(t) = Corr(y, x)(-t)\,. \tag{2.10}$$

In its continuous form, the correlation is defined as as:

$$Corr(x, y) \equiv \int_{-\infty}^{\infty} \overline{x}(\tau + t)y(\tau)d\tau\,. \tag{2.11}$$

where $\overline{x}$ is the complex conjugate of x and, in the case of real functions, $\overline{x} = x$ Some analysis requires that the correlation between the two time series is estimated simultaneously, i.e. with $t = 0$: this is known as *zero–delay cross–correlation* and it will be exploited in our analysis, as described in detail in Chapter 4.
As previously mentioned, in most real cases the time series are not continuous functions but discrete sequences. The discrete form of correlation between two sampled functions x_s and y_s, periodic with period N, is given by:

$$Corr(x, y)[j] = \sum_{j=0}^{N-1} x[j + s]y[j]\,. \tag{2.12}$$

According to the *discrete correlation theorem*, the $Corr(x, y)[j]$ between two real functions x and y can be estimated also by means of their Fourier transforms. To do this, firstly the Fourier transform of both series is calculated, obtaining X_k and Y_k; then one transform is multiplied for the complex conjugate of the other and finally the inverse transform of the final product is computed.
There are different kind of methods to establish correlation as Pearson correlation, Spearman correlation, intra–class correlation, and others. However, the most common one – that is also the method used in this thesis work – is the Pearson correlation. For these reasons it will be the only one described here, whereas for an overview of the other methods Refs. [60] and [12] are suggested.

Pearson's correlation Given two pairs of random variables (x_i, y_i) of length N, the linear correlation coefficient or Pearson correlation coefficient $r_{x,y}$ is defined as:

$$r_{x,y} = \frac{\sum_i (x_i(t) - \overline{x})(y_i(t) - \overline{y})}{\sqrt{\sum_i (x_i(t) - \overline{x})^2 \sum_i (y_i(t) - \overline{y})^2}}\,. \tag{2.13}$$

where $\overline{x}$ and $\overline{y}$ are the mean values of x_i and y_i respectively. One of the major problems of r is that it is not a significant measure of the strength of a correlation *per se*, because it completely ignores the distributions of the x_is and y_is samples. Thus, it does not exist a general solution to compute the r distribution, but some solutions to overcome this problem will be proposed in Section 2.3.

Autocorrelation Another important declination of the correlation definition is the autocorrelation. The autocorrelation of a random process corresponds to the Pearson correlation between values of the process at different times, to verify how much the time series is *similar* (correlated) with itself during time. It follows that the autocorrelation is a function of the time lag.
Given a stochastic process x, the autocorrelation is defined as:

$$A_{x,x}(\tau) = \int_{-\infty}^{\infty} \overline{x}(t)x(t+\tau)dt\,, \tag{2.14}$$

where $\overline{x}(t)$ is the complex conjugate of $x(t)$. In the case of real processes, $\overline{x}(t) = x(t)$.

Wiener-Khinchin theorem Strictly related to autocorrelation is the theorem of Wiener–Khinchin that shows some important properties of this measure. The theorem defines the relation between autocorrelation and the power spectral density $S_{x,x}(f)$ of a process x. The power spectral density describes the distribution of the time series power over the frequencies and it is defined for continuous time series over time, as stationary processes. The power spectral density is defined as:

$$S_{x,x}(f) = X(f)\overline{X}(f)\,, \tag{2.15}$$

that, for real functions, is equivalent to:

$$S_{x,x}(f) = |X(f)|^2 \quad 0 \leq f < \infty\,, \tag{2.16}$$

where $X(f)$ is the Fourier transform of $x(t)$.
The Wiener–Khinchin theorem states that if a x is a weakly stationary process such that its autocorrelation exists and is finite for every value of lag τ, then the following relation holds:

$$A_{x,x}(\tau) = \int_{-\infty}^{\infty} S_{x,x}(f)e^{2\pi i\tau f}df. \tag{2.17}$$

This last equation is obtained from the definition of autocorrelation (Eq. 2.14) and Fourier transforms (Eqs. 2.1) and assesses that the autocorrelation is given by the inverse of the Fourier transform of the power spectral density of the signal.

Coherence

Another very common linear method to estimate functional connectivity is the coherence. It gives information about the degree of coupling between two signals at a certain frequency, quantifying the linear correlations in the frequency domain. The coherency measures the synchronization of two signals on the basis of their phase consistency[Srinivasan, J Neurosci Methods, 2007]: it means that two signals can be out of phase and nevertheless have high coherence if their phase difference remains constant. The coherence between two time series is estimated as:

$$Coh_{xy} = \frac{|S_{xy}(f)|^2}{S_{xx}(f)S_{yy}(f)} \tag{2.18}$$

where $S_{xy}(f) = X(f)\overline{Y}(f)$ is the square intensity of the cross–spectral density of the two signals, calculated by the product between the Fourier transform of the signal x and the complex conjugate of the signal y. On the other hand, S_{xx} and S_{yy} represents the power spectral densities of the two time series x and y respectively. As previously mentioned, Coh_{xy} depends on the frequency band on which the cross–spectral

density is estimated and its values ranges from 0 to 1, where 1 represents the perfect coupling.
This method is highly used for functional connectivity studies, thanks to a techniques that is its direct application, the dynamic imaging of coherent sources: given a reference signal, it is able to localize the sources that are coherent to that signal.
As in correlation case, coherence is prone to false positives due to spurious correlations as well. To overcome this problem, a modified version exists, that is obtained by replacing the cross–spectrum term in Eq. 2.18 with its imaginary part, that, by its very nature, cannot be influenced by zero–lag correlations (see [12]).

2.2.2 Non–linear metrics

Band Limited Power Correlations

Estimating the correlations between amplitudes or power envelopes of band–limited oscillations is a widespread method to measure connectivity. The envelope dynamics evolves in a scale of seconds or minutes and their correlation decreases with the distance but not as fast as the raw signals used to estimate envelopes. In order to calculate the band–limited power of a signal, it is possible to filter the series according to the frequencies of interest or, on the other hand, to apply the Hilbert transformation. This is another very diffused method of brain connectivity analysis, of which it is worth saying a few words.

Hilbert transform The Hilbert transform is a linear operator, that, given a function $u(t)$, transforms $u(t)$ in another function $H(u(t))$ such as:

$$H(u(t)) = -\frac{1}{\pi} \lim_{\epsilon \to 0} \int_{\epsilon}^{\infty} \frac{u(t+\tau) - u(t-\tau)}{\tau} d\tau \,. \tag{2.19}$$

In frequency domain, the Hilbert transform has a very simple representation: it is a multiplier operator and it has the effect of a positive 90° shifting of the negative Fourier components of the function and of a negative 90° shifting of the positive ones. Thanks to the Hilbert transform, it is possible to reconstruct the *analytic signal* of a time series , that is a real–valued function, without negative components, estimated as follows:

$$z_\theta(t) = \hat{Q}_\theta(t) + iH\left[\hat{Q}_\theta(t)\right] \,, \tag{2.20}$$

where $\hat{Q}_\theta(t)$ is the band of interest and $H(\hat{Q}_\theta(t))$ is its Hilbert transform, calculated as in Eq. 2.19.
The Hilbert envelope of the whole signals is calculated as follows:

$$E\left[\hat{Q}_\theta(t)\right] = \sqrt{\left[\hat{Q}_\theta(t)\right]^2 + \left[H(\hat{Q}_\theta(t))\right]^2} \,, \tag{2.21}$$

in order to estimate the statistical interdependence between the brain regions, or, in other words, to analyze the functional connectivity directly in source space, as explained in the following paragraphs.
In this last case, once reconstructed the source space the analytic signal for each voxel and the corresponding envelope are estimated, as seen in Paragraph 2.2.2.
Once obtained the envelopes, it is possible to apply a metric of connectivity between two source locations (or *seeds*) of interest, for example by using the Pearson correlation. This is known as a seed–based approach to connectivity analysis, and requires a priori knowledge about seed locations.

2.2.3 Independent Component Analysis

Another method that is worth mentioning since it is widespread in connectivity analysis is the Independent Component Analysis (ICA). To avoid ambiguities, its description has been placed in a separated section since it is actually a linear decomposition (thus, an intrinsically linear method), but it is often applied to non–linear band–limited power signals, thus being part of non–linear analysis.
ICA is an alternative technique to seed–based approaches, since it is not constrained by a priori knowledge of seeds locations. For example, it is frequently used to identify the noise components in MEG signals, but it produces excellent results in functional connectivity analysis as well.
Let us assume to have a dataset of M subjects: the general method to compute ICA for connectivity analysis is by matrix representation. Once estimated the envelope of the times series corresponding to the n–th voxel of the m–th subject, the matrix $\mathbf{X}$ is a $N \times MT$ matrix where N is the number of source locations and T the length of the resulting envelope. In fact, $\mathbf{X}$ is a concatenated data matrix, representing data from all subjects and acquisitions for a single frequency band of interest.
When we use MEG signals, because of the excellent temporal resolution of the acquisition method, the greatest amount of information are obtained by estimating temporal ICA. To do this, the matrix $\mathbf{X}$ can be express as the result of a linear mixture of independent signals $\mathbf{S}$, where the contribution of each time series is given by a mixing matrix $\mathbf{A}$:

$$\mathbf{X} = \mathbf{AS} \tag{2.22}$$

The elements of the matrices $\mathbf{A}$ and $\mathbf{S}$ are unknown, and can be estimated by only knowing the time series envelopes of $\mathbf{X}$, in an unsupervised way. What we want to know is the $\mathbf{S}$ matrix, by solving:

$$\mathbf{S} = \mathbf{WX} \tag{2.23}$$

where $\mathbf{W}$ is the inverse of $\mathbf{A}$. Estimate $\mathbf{W}$ is not straightforward since $\mathbf{A}$ is unknown, then $\mathbf{W}$ is the result of an iterative process [73]: it starts from random values of its elements that are updated until one independent component is found. The independent components are identified because they are orthogonal to the other transformed signals. This way, independent time series are obtained without an *a priori* selection of a seed voxel.

2.3 Significance Estimation

When a statistical test as those previously described is performed, the aim is to disprove or accept an initial hypothesis. One can take, for example, two signals x and y, in order to check if they are correlated or not. Thus, the corresponding correlation coefficient $r_{x,y}$ is evaluated, according to Eq. 4.4. However, the $r_{x,y}$ value has no relevance in itself to ascertain correlation, but it must be associated to a correspondent *level of significance*. To do this, it is necessary to make an initial assumption H_0 – the *null hypothesis* – and test if it is false or not. In general, the null hypothesis assumes that the assumption to verify does not happen: in our example, H_0 states that no correlation exists between x and y. However, it is necessary to know how likely a certain value of r_{xy} occurs, in the event that H_0 is true. This probability is known as p–value and can be expressed as the conditional probability to observe a certain realization of X given a certain initial hypothesis H_0:

$$p = \Pr(|X - E| \geq |x - E||H_0) \tag{2.24}$$

where X is the continuous random variable representing the observed data, x is a specific instance of X and E is the expected value.
Nonetheless, this probability alone is not enough to determine the correct interpretation of the observed statistics. Let us consider the sampling distribution of the observed test statistics: it can be divided in two parts, the rejection region (or *critical*) and the acceptance region. However, it is necessary to define the critical value that distinguishes the two regions. Such value is known as significance level α and discriminates if the probability of a certain realization of X (in other words, its p–value) rejects or confirms the null hypothesis: if the p–value is below α, so within the rejection region, the hypothesis has to be rejected. According to our example, it means that there is a good chance that a correlation exists.
It is worth noting that rejecting the null hypothesis does not imply that the correlation is necessarily *true*, but only *highly probable*: in other words, there is a probability lower than α that the estimated correlation value corresponds to no correlation between the two signals tested. In the same way, α can be considered as the probability to wrongly reject the null hypothesis. The value of α is not fixed but is chosen according to the nature of the signals and the specific circumstances (e.g. the acquisition conditions). However, there are three commonly used probability thresholds, $\alpha = 0.05, 0.01, 0.001$, corresponding to 95%, 99% and 99.9% chance that the null hypothesis has to be rejected. Clearly, the lower the α value, the more robust the significance of the result.
Thus, a non–zero probability to wrongly confirm or disprove a null–hypothesis exists. This corresponds to errors of different type:

- **type I error**: the rejection of the null–hypothesis when it is "true" (the probability is α),
- **type II error**: the failure to reject a null–hypothesis when it is false (its probability is called β).

The value of α determines the size of the critical region and the choice of its value mainly depends on the "costs" that the occurrence of a type I error produces.
One way to reduce the occurrence of type II errors is by increasing the sample dimension. A higher sample dimension allows to identifies the small differences between the sample statistics and the corresponding true population parameter (as the mean, or the variance). For a certain α, increasing the sample dimension reduces β and the test turns out to be more powerful in correctly rejecting H_0. However, there is a trade–off between the two types of errors: if β decreases, α increases and viceversa.
There are a lot of tests to establish the significance of a result. However, one of the major issue in significance determination is that the distribution of the observed data is generally not known. In most of cases, the null–hypothesis assumes that the population of the sample dataset follows a Gaussian distribution. This hypothesis, that is often too restrictive in real cases (see Paragraph 2.3.3), is increasingly more reliable with large samples, thanks to the central limit theorem [9]. In the following paragraph, I will give a brief introduction about the various kind of tests and their requirements and prerogatives. For a more detailed discussion, see [60] and [9].

2.3.1 Statistical Tests

The first classification of statistical tests is between *parametric* and *non–parametric* tests. In the first case, the main assumption is that there are information about at least one population parameters (as the real mean or variance of the distribution), a condition that is not satisfied by the second group. In the case of non–parametric tests, the model structure of the data distribution is derived from data, for this reason they are also known as *distribution–free methods*).
There are a lot of well–known examples of both groups: the z–test, the t–test, the f–test and others are parametric tests, whereas ranking–based methods as the Kendall's τ, the Kolmogorov–Smirnov test, the Spearman's rank correlation coefficient and many other belong to the non–parametric group.
An alternative approach to non–parametric tests whenever the data distribution is not known is the method of surrogates, discussed in details in Paragraph 2.3.3.
As it will be shown in Chapter 4, the significance tests used in the core part of this thesis work are of two kinds. The first one assumes as null–hypothesis that the process underlying the data is Gaussianly distributed; the second has a less restrictive H_0 and tries to reproduce the behavior of data by means of surrogates with the same amplitude distribution and power spectrum. To not cluttering up the discussion, in the next paragraphs I am going to describe the methods actually used in this work of thesis, necessarily disregarding all other examples of significance tests. For further details about the topic, Ref. [60] is suggested.

Z–test and t–test Two of the most commonly used parametric methods are the **z–test** and the strictly related **t–test**.
The 2–tailed **z–test** is designed to verify if the mean value μ of a distribution is significantly different from a reference value μ_0 (e.g. the true mean of the distribution). The two requirements to use the z–test are that the underlying distribution of the sample dataset is Gaussian and that the standard deviation σ is known. Its statistics is defined as:

$$z = \frac{\bar{x} - \mu_0}{\frac{\sigma}{\sqrt{N}}} \tag{2.25}$$

where $\bar{x}$ is the normally distributed sample mean and N is the dimension of the sample. In the event that the population distribution is not normal, it is still possible to state that the sample mean tends to the Gaussian mean for $N \to \infty$, thanks to the central limit theorem. Normalizing with respect to μ_0, it results a standard Gaussian distribution with mean 0 and unitary variance.
Given a certain confidence level α, the H_0 is rejected if the resulting value of the parameter z is lower than $\alpha/2$ (in the case of a two–tailed test).
In many real cases, the population variance σ^2 is unknown, so the z–test cannot apply. It is necessary to estimate the sample variance according to:

$$s^2 = \frac{\sum_{i=1}^{N}(x_i - \bar{x})^2}{N-1} \tag{2.26}$$

that is the realization of the population variance.
Once the sample variance is calculated, the proper statistical test to determine significance is the **t–test**. It is still parametric and has the same target as the z–test, i.e. it aims at verifying if the mean value of a distribution is significantly different from a reference value. The statistics t is estimated as:

$$t = \frac{\overline{X} - \mu}{s/\sqrt{N}} \tag{2.27}$$

where $\overline{X}$ is the sample mean, μ is the population mean and s represents the sample standard deviation. Its probability distribution is a T–Student with $N-1$ degrees of freedom. The null–hypothesis is verified in the same way as z–test: the estimated value of t is compared with the quantile $\alpha/2$ order (in the case of 2–tailed t–test) of the T–Student distribution with $N-1$ degrees of freedom. If it is lower H_0 is rejected.
However, in real cases it frequently happens that the distribution of the random variables observed is not normal. This is the case of the Pearson correlation coefficient, the statistical parameter of particular interest in this work, as we will see later. A method to overcome this problem is described in the next paragraph.

Fisher transformation Let us consider two time series x and y as in the previous example, and estimate the corresponding correlation coefficient $r_{x,y}$. The sampling distribution is known and changes according to the population mean $\bar{r}$ value. If $\bar{r} \leq 0.4$ the resulting distribution is approximately normal, however for higher values of correlation the distribution exhibits a negative skew. To overcome this problem it is possible to apply a transformation called Fisher's z transformation that converts the correlation coefficient r to a normally distributed variable z, with a standard error given by:

$$se = \frac{1}{\sqrt{N-3}}\,. \tag{2.28}$$

The transformation is performed as follows:

$$z = \frac{1}{2}\left[\ln(1+r) - \ln(1-r)\right] = \operatorname{arctanh}(r)\,. \tag{2.29}$$

This operation allows to obtain a distribution that is normal and with a stable variance independently of the correlation value. Moreover, it is particularly useful for small samples because the Pearson's distribution is particularly skewed in this condition. On the other hand, care must be taken since Fisher transformation is not well suited for too skewed data and in presence of extreme outliers.

2.3.2 Fisher F test

Another method to assess the significance of a correlation observed between two variables relies on the Fisher F–test.
The F–test can be used when the error term in a regression model is normally distributed. It is conceptually similar to the t–test previously described, except that in the F–test case more than two parameters are involved at once when testing the null hypothesis.
One of the possible applications of the F–test is in regression problems. Let us assume that X_i and Y_i are two normal i.i.d. random variables such that $(X, Y) \sim f(x, y)$, with $f(x, y)$ joint population pdf of (X, Y).
One of the requirements for applying the F–test is the homoscedasticity of the $f(y|x)$ *pdf*, i.e. $(Y|X = x) \sim \mathcal{N}(\mathrm{E}(Y|x), \sigma^2)$.

Two possible models can represent the dataset, one (called B) nested in the other one (called A): the model A has p_A parameters whereas the B has p_B parameters and $p_B < p_A$. The model A (B) is said to be unrestricted (restricted or *naive*).
A compact way to express both models is:

$$Y_i = \beta_0 + \beta_1 x_i + \beta_2 d_i + \beta_3 d_i x_i + e_i = \begin{cases} (\beta_0 + \beta_2) + (\beta_1 + \beta_3) x_i + e_i & \text{if } d = 1 \\ \beta_0 + \beta_1 x_i + e_i & \text{if } d = 0 \end{cases} \tag{2.30}$$

where the e_is are the *prediction errors*, with $i = \{1, \ldots, N\}$ and $e_i \sim \mathcal{N}(0, \sigma^2)$. In Eq. 2.30, the parameter d_i allows to switch from one model to the other according to its value: if $d = 0$ all the equation terms different from β_0 and β_1 are null and the the restricted model B is obtained ($Y_i = \beta_0 + \beta_1 x_i$); otherwise, if $d = 1$, the equation preserves all its terms and represents the full (or unconstrained) model A.
For every choice of the p_B parameters, it exists a selection of p_A able to obtain the same regression curve as in model B. The purpose of the test is to verify if the unrestricted model fits the data better than the restricted one that has the intercept as only explanatory term. The difference between the two models is that in B all the parameter coefficients of the explanatory terms present in model A and different from the intercept are considered as equal to zero. The main ideas of the method is that, in any case, the multi–parameter model fits the data better than the naive one, thus the prediction error estimated on the regression model A is lower. In order to verify if A describes data significantly better than B, the F–test is used. The F statistics can be estimated as:

$$F = \frac{\frac{RSS_1 - RSS_2}{p_2 - p_1}}{\frac{RSS_2}{n - p_2}} \tag{2.31}$$

where RSS_i is the residual sum of squares of the i model and n represents the sample dimension. The RSS_i value is estimated as:

$$RSS_i = \sum_{i=1}^{n} (Y_i - \hat{Y}_i)^2 \tag{2.32}$$

where $\hat{Y}_i$ corresponds to the predicted Y_i value, according to a certain selection of parameters.
The null hypothesis H_0 assumes that the two models fits the data equally well. In this case, the F statistic is distributed according to the F–distribution with $(p_2 - p_1)$ and p_2 degrees of freedom: according to the F distribution it is possible to estimate the significance of the F value obtained for the two models, and to evaluate the corresponding p-value.
In this thesis, a surrogate–based test rather than the F–test approach was preferred since it is not immediately clear whether the different random variables of interest satisfy the normality and homoscedasticity hypothesis.

2.3.3 Surrogates

In the case of complex systems, the assumption that the process underlying the signals is gaussian, nonlinear and stochastic is very restrictive, causing false positives or negatives in significance detection. This problem can be partially overcome by using surrogates of the original time series. This method produces stochastic signals that maintain the same distribution and/or spectral properties, according to the algorithm used. As it will be shown in Chapter 4, the algorithm we selected for

surrogates estimation is those developed by Schreiber and Schmitz in 1996 [66] and present in the TISEAN package [35]. It is an iterative algorithm, generating surrogates with the same distribution and power spectrum of the measured signals.
The first version of this algorithm is known as Amplitude Adjusted Fourier Transform (AAFT). It is based on the generation of surrogates of a time series by means of the randomization of the Fourier phases, but maintaining the periodogram of the original time series, as explained by Schreiber and Schmitz in [66].
Let us consider a time series $\{s_n\}$ and an instantaneous, invertible, measurement function h, independent from time. The null hypothesis assumes that the underlying phenomenon producing $\{s_n\}$ is a Gaussian linear stochastic signal $\{x_n\}$, such that $s_n = h(x_n)$.
Then, let $\{g_n\}$ be a random Gaussian reference sequence, sorted in ascending order. According to $\{g_n\}$, the amplitude values of the sequence $\{s_n\}$ are rescaled. The resulting rescaled sequence $\{r_n\}$ is obtained by:

$$r_n = g_{\text{rank}_{s_n}} . \tag{2.33}$$

Let $P_s = \text{rank}_{s_n}$, i.e. the rank order of the $n-$th element of the $\{s_n\}$ sequence; the value of the element r_n is given by the corresponding element of the sorted $\{g_n\}$ series in the P_s position. The surrogates are realized having the same Fourier spectrum of the rescaled data: this is obtained by estimating the Fourier transform of $\{r_n\}$ and by multiplying its complex amplitude by random phases $e^{i\alpha_k}$:

$$\bar{r}_n = \frac{1}{\sqrt{N}} \sum_{k=0}^{N-1} e^{i\alpha_k} |S_k| \exp\left[-\frac{i2\pi kn}{N}\right] , \tag{2.34}$$

where $0 \leqslant \alpha_k < 2\pi$ are independent uniform random numbers. Then, the surrogates are scaled back to have the same amplitude of the original sequence $\{s_n\}$ [74].
Following this process, for a finite N, the surrogates have the same distribution but usually not the same power spectrum. This is due to two factors: firstly, the phase randomization maintains the Gaussian distribution only on average, because of the non–linearity of the amplitude adjustment process (see Ref. [66]); secondly, the Gaussian rank ordering process is not the inverse of the measurement function h. This means that $r_n \neq x_n$ and the rescaling operation produces another Gaussian time series. In both cases, the resulting surrogate power spectra can be altered. In particular, in case of short and strongly autocorrelated sequences, the surrogate spectrum can be slightly flatter. For this reason, a modified algorithm was proposed in Ref. [66] (the *Iterative* AAFT, or IAFFT), that is that actually implemented in the TISEAN package used in this thesis.
It is worth noticing that the null hypothesis of a Gaussian linear stochastic process can be formulated assuming that the first and second order quantities are sufficient to describe any structure in the time series. Surrogates are obtained by random sequences forced to have the same second order properties of the original series (*constrained realization*), since the Wiener–Khinchin theorem states that two time series with the same autocorrelation have the same power spectra.
The linear properties of a time series are specified by the squared amplitude of the discrete Fourier transform:

$$|S_k|^2 = \left| \frac{1}{\sqrt{N}} \sum_{n=0}^{N-1} s_n^{(k)} e^{i2\pi kn/N} \right|^2 , \tag{2.35}$$

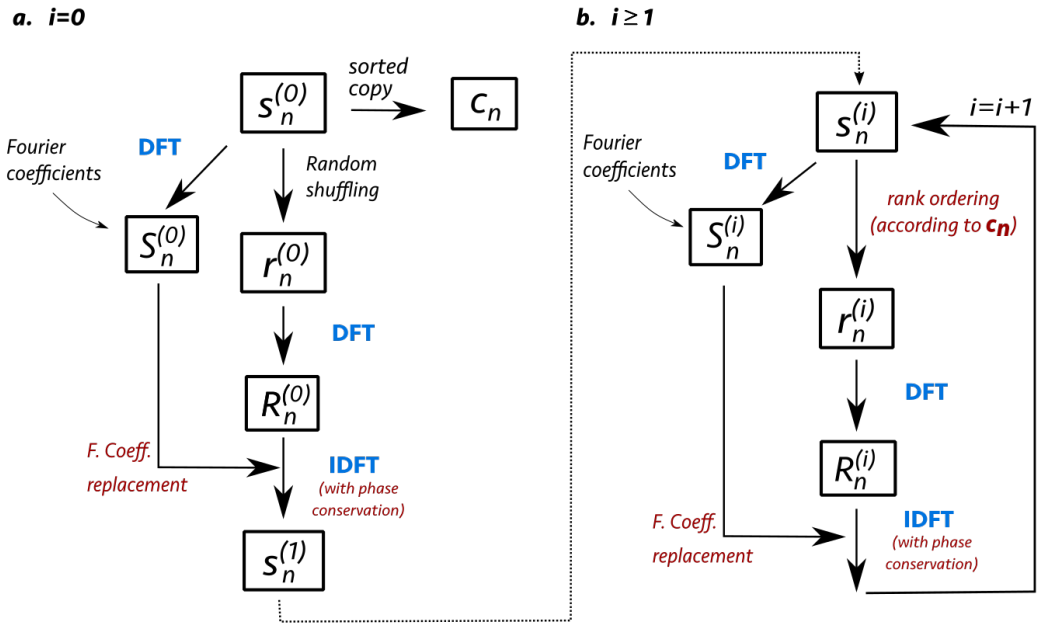

FIGURE 2.1: TISEAN surrogates algorithm.

that is the periodogram estimator of the power spectrum. The refined IAAFT algorithm allows to obtain, at every iteration step, two sequences, one with the correct distribution and the other with the correct Fourier amplitudes.

Let us show some details about the IAAFT calculation steps. A graphical representation of the algorithm is given in Figure 2.1. Given a measured signal $\{s_n^{(0)}\}$, the discrete Fourier transform is estimated, according to Eq. 2.4. The resulting squared Fourier amplitudes $\{S_k^{(0),2}\}$ are obtained according to Eq. 2.35.

In addition, a copy of $\{s_n^{(0)}\}$, but sorted in ascending ordered, is stored as $\{c_n\}$. The first step of the iteration ($i = 0$) consists in a random shuffling without replacement of $\{s_n^{(0)}\}$: the series produced is $\{r_n^{(0)}\}$. It has the same amplitude distribution as $\{s_n^{(0)}\}$ by construction and coincides to $\{c_n\}$ if it is reordered. Then, the DFT of the $\{r_n^{(0)}\}$ is calculated, obtaining the corresponding Fourier amplitudes $\{R_k^{(0)}\}$. In order to produce a series $\{r_n^{(0)}\}$ preserving the spectral properties of $\{s_n^{(0)}\}$, the squared Fourier amplitudes $\{R_k^{(0),2}\}$ are replaced with $\{S_k^{(0),2}\}$.

The i–th surrogate version (for now, $i = 0$, see Figure 2.1a) is estimated by applying an inverse discrete Fourier transformation. Thanks to this constrained transformation, the phases are kept and a series with the desired power spectrum is obtained, although it is no more guarantee that the distribution value of $\{s_n^{(i)}\}$ is the same as $\{s_n^{(0)}\}$. At the end of the first phase of the algorithm, $s_n^{(1)}$ is obtained. Then, $s_n^{(1)}$ enters the loop: the series, that from now on I will generally call $s_n^{(i)}$, is rank ordered according to $\{c_n\}$. The ranking result is $\{r_n^{(i+1)}\}$ (see Figure 2.1b). For every i–th iteration, the transition from $\{r_n^{(i)}\}$ to $\{s_n^{(i+1)}\}$ is necessary to obtain power spectrum conservation. However, it is defined by the authors themselves [66] as a *crude filter* in Fourier domain, because the Fourier amplitudes are simply replaced with the desired ones.

The amount of iterations is determined by the number of necessary steps to obtain surrogates with the best approximation distribution and power spectrum.
All the iterative process aims at reaching a convergence towards a fixed point such that $\{r_n^{(i+1)}\} = \{r_n^{(i)}\}$. Although the distribution and power spectra requirements cannot be completely satisfied in a finite N, they are built to have exactly the same data distribution (without replacement) and the power spectra as similar as possible to the original series. Once reached the fixed point, the remaining discrepancy between $\{r_n^{(\infty)}\}$ and $\{s_n^{(\infty)}\}$ can be considered as a measure of the method accuracy. One can require a maximum possible discrepancy of the resulting power spectrum, in order to reject the result if it does not satisfied the condition.

2.3.4 Bonferroni correction

It can happen that several dependent or independent statistical tests have to be performed on the same set of data. This might increase the probability to identify false positive errors, since the occurrence of at least one significant result due to chance increases with the number of the hypothesis tested. The Bonferroni correction is designed to correct this effect, by reducing the significance level α to a more stringent value according to the number of hypothesis tested. Thus, each hypothesis is tested at a significance level of α/k, where k is the overall number of the considered hypotheses. Let us consider a set of k hypothesis H_i each one with a corresponding p–value p_i. According to the Bonferroni correction, each p_i has to be lower than α/k. The overall probability to reject at least one true hypothesis, producing a type I error, is known as *familywise error rate* (FWER). Thanks to Bonferroni correction FWER is lower than α, as justified by Bonferroni's inequality, that states:

$$P\left(\bigcup_{i=1}^{k} H_i\right) \leq \sum_{i=1}^{k} P(H_i)\,. \tag{2.36}$$

Thus, it results that:

$$P(\text{some } H_i \text{ passes})|H_0) \leq \frac{\alpha}{k} \tag{2.37}$$

One possible drawback of the method is that, although the type I errors are reduced, the probability that type II errors occur increases.

Given this brief overview of the main statistical tools to investigate network connectivity, I am going to introduce the theoretical background to understand the origin of the signals that will be mainly used in this thesis: the *magnetoencephalography*.

Chapter 3

Magnetoencephalography

The magnetoencephalography (MEG) is a non–invasive brain imaging technique, particularly suited to investigate the global properties of the brain [32]. MEG accesses real–time information about biomagnetic fields related to neural activity. It performs a direct measure of such activity, in contrast to functional magnetic resonance imaging (fMRI) that depends on an indirect source of information, the hemodynamic response. This prerogative ensures a particularly high temporal resolution ($\sim$ 1 ms) of MEG compared to fMRI ($\sim$ 1 s). Thus, MEG is particularly suited to investigate neural network dynamics.
MEG is sensitive to the same neurophysiological phenomena as the electroencephalography (EEG), i.e. the electromagnetic fields produced by the electric currents during neural activities [59]. However, MEG has a better sensitivity to weak signals, because the neuromagnetic fields are slightly attenuated by the brain tissue and the skull, unlike electric potentials measured by EEG [32]. MEG also has a better spatial resolution (10–15 mm), achievable without using algorithms to model head conductivity as complex as EEG requires.
In light of the above, MEG is a reliable tool to obtain new information about the human brain organization and to understand its functional mechanisms.
In this Chapter, I present the biology of the neural activity sources and the methods and instruments used to acquire their signals. Then, a general overview of how such signals are elaborated to reconstruct a map of source locations will follow. Although deepening these aspects are out of the scopes of this work, it is important to give some information about the steps producing the signal we analyze, to better understand its characteristics. In the second part of the chapter, I briefly describe other common methods used in the study of neural activity. Some neurophysiological considerations about functional brain networks are given in the last section, with a particular focus on resting state networks. A dedicated paragraph is devoted to one of those networks of particular interest for our purposes: the Default Mode Network.

3.1 The MEG Signal

3.1.1 A bit of history

Magnetoencephalography, currently very popular worldwide, did not develop from a dedicated field of investigation. It was the result of the merging between two parallel research fields, one devoted to the study of the quantum phenomena related to low–temperature superconductors and the other interested in the physiological origins of the biomagnetic signals. Researches related to quantum phenomena produced extremely sensitive sensors of magnetic field, the Superconductive Quantum

Interference Device or SQUID, described in Section 3.2.1. In parallel, a growing interest in biomedical signals was developing: in 1968 – before SQUIDs were invented – a physicist, David Cohen, by using a copper induction coil detector, was the first one to measure a MEG signal. However, the detector had a low sensitivity and a lot of noise, and the shielding towards the environment was not sufficient. A major breakthrough was the idea to use the SQUID as a MEG sensor: the project was proposed by Cohen and the SQUID's father, the physicist/engineer James E. Zimmerman, who measured the first MEG signal produced by a human heart in a magnetically shielded room at the MIT. The results of their work were published in 1970 [16] and they proposed possible applications of the SQUID in the medical field. Two years later Cohen released the first work about MEG signal recording in a human brain [15].
Initially, the first configurations of MEG acquisition systems had just one SQUID sensor to perform subsequent measures of the magnetic field outside the brain in different positions. However, the process was excessively complicated and a multisensor array was proposed to cover a larger head portion. The present configuration, as I will explain in the following, consists of 300 sensors dipped in a helmet–shaped vacuum flask. The helmet surrounds the most of the head surface, allowing to acquire a great amount of MEG recordings rapidly and efficiently.
Recently, MEG has been used in many clinical researches in mental disorders, anomaly conditions as epilepsy, or cases of neural reorganization as a consequence of traumas or strokes. Let us now give a look to the physiological processes inducing the MEG signal.

3.1.2 A biological point of view

To better understand the nature of the signals measured by MEG, it is important to know what is their biological origin.
Let us consider a group of neurons. A fundamental prerequisite for neural signaling is the presence of a potential difference of -67 mV to the extremes of the neural cell. The potential difference is maintained thanks to a different concentration of sodium and potassium ions between the inside and outside of the cell: this way, the inside of the membrane is negatively charged compared to the outside.
To understand the neurotransmission mechanism, let us start by considering the elementary process involving two single neurons (see Fig. 3.1). The "first" neuron (known as *pre–synaptic*) receives input signals of different natures (chemical, electrical, ...) from the nearby neurons. When the sum of these signals reaches a certain threshold, an action potential spikes. Borrowing the effective definition of Mosier [52], an action potential is an "*all–or–nothing*, regenerative, directionally propagated, depolarizing nerve impulse". "All–or–nothing" means that whenever the sum of the input signals overcomes the voltage threshold of -55 mV, no matter of how much, the depolarization wave begins and reaches the maximum amplitude of 30 mV. The depolarization is due to a rapid influx of Na^+ ions that locally neutralize the negative charge in the first portion of the axon membrane, before passing to the next one. This causes a depolarization wave along the whole axon up to its terminals. Such wave always goes from the pre–synaptic to the "second" (*post–synaptic*) neuron. This is ensured by the shape of the action potential curve. As shown in Fig. 3.2, after reaching the depolarization maximum, the repolarization process is followed by a hyperpolarization phase. The axon region is then shielded from the one following it, communicating the depolarization pulse in one direction only. When the impulse reaches the axon terminal, it induces the release of neurotransmitters

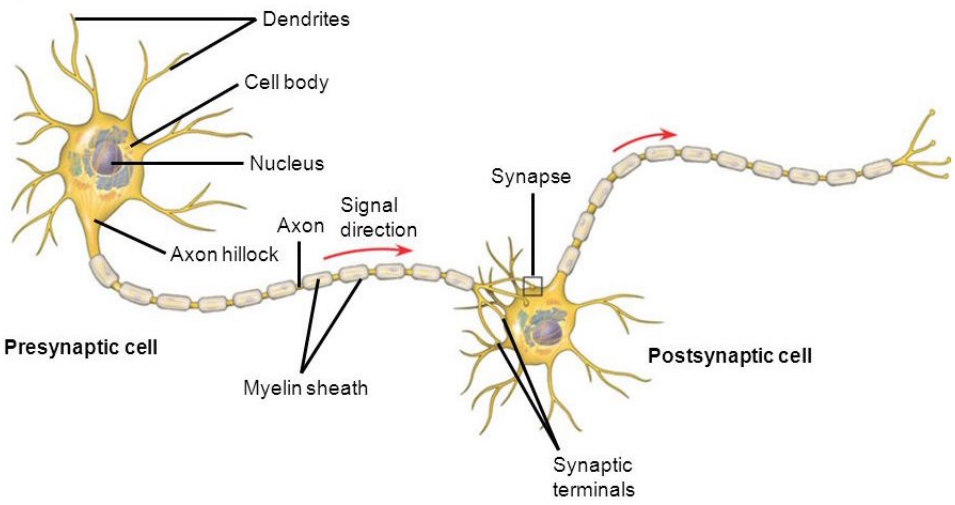

FIGURE 3.1: A pre–synaptic and post–synaptic neurons structure: when the amount of signal collected by the dendrites of the pre–synaptic neuron from the nearby neurons overcomes the critical threshold of -55 mV, the pre–synaptic neuron fires an action potential. The polarization wave produced by the action potential runs along the axon towards the post–synaptic neuron. Once it reaches the synapses, excitatory or inhibitory neurotransmitters are released through the pre–synaptic membrane. Then, the neurotransmitters bind to the post-synaptic receptors inducing a post–synaptic potential.

in the cleft between the two neurons, a.k.a. the synapse. The most common excitatory neurotransmitter is the glutamate, processed thanks to the energy provided by glycolysis and sugar oxydation. The role of oxygen in brain functionality is extremely important to identify activated areas in the brain, as will be explained in Section 3.5.1.

After their release, glutamate molecules bond with the receptors on the the post–synaptic neuron. These bonds, opening ionic gates, can cause a depolarization in the membrane of the second neuron, triggering a post–synaptic potential. The actual signal to which MEG is sensitive is the summation of many post–synaptic potentials produced by a group of neurons firing together. Conversely, the pre–synaptic action potential is not measurable, even if many neurons fire simultaneously. Once again, this effect is due to the shape of the action–potential (see Fig. 3.2), that is by its very nature biphasic. It means that, after a positive rise of the potential curve, a rapid fall to negative values will follow. Moreover, the pre–synaptic potential is a very short–living phenomenon (1–2 ms). Thus, the action potentials should be perfectly synchronized to have a positive summation, or, in other words, the curves should be perfectly superimposed, a very unlikely circumstance. Otherwise, they cancel each other out and the resulting amplitude is suppressed. In the post–synaptic potential case, everything is easier: a positive summation is possible thanks to the monophasic nature of the signal and to its longer duration compared to the pre–synaptic one. However, only these two characteristics would not be sufficient to make the neural signal detectable, because, in order to obtain a sufficient signal strength, the dendritic trees (see Figure 3.3) need to be oriented in parallel. This way, the post–synaptic currents generated by the apical dendrites travel to the neuron soma (see Fig. 3.1) and can sum up. It is worth keeping in mind that we do not measure all the neural activity since inhibitory interneurons are present and are not oriented in the

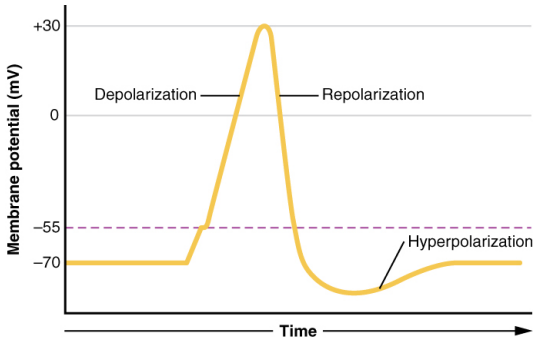

FIGURE 3.2: Action potential wave shape. The membrane of a neuron not involved in any signal transmission is polarized with a differential potential of -67 mV. When the dendrites collect signals, the membrane progressively depolarizes. If the membrane level of depolarization overcomes the critical value of -55 mV, a depolarization wave starts reaching the maximun value of 30 mV. Then it decreases, reaching a hyperpolarized state: this condition ensures that the action potential spreads only towards the post–synaptic neuron.

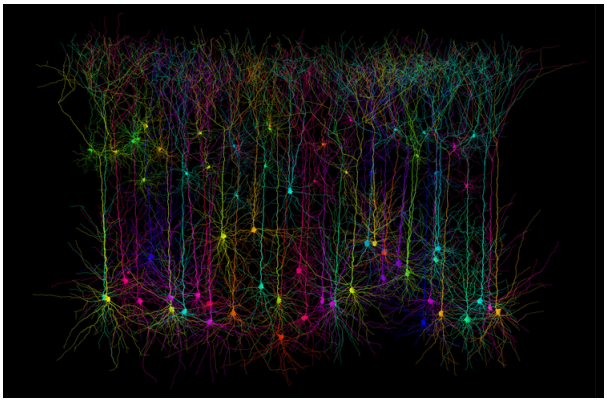

FIGURE 3.3: Synthetic representation of dendritic trees [40].

same direction of the other neurons: they have a "negative" contribution to the overall measured brain signal. MEG and EEG, despite being direct measures of the brain activity, are not able to distinguish between these opposed contributions of different physiological processes and this represents one of their limitations. The same considerations apply to fMRI, relying on measures of hemodynamic signal variations. They are considered as an expression of the brain activity but the real physiological origins are not completely understood.

3.1.3 The current dipole approximation

Besides the physiological considerations, a major problem in brain imaging reconstruction is the localization of the neural sources engaged in neural communication. It is not possible to locate the source of the single post–synaptic current, but only to localize the elementary region where a small population of a few tens of thousands of neurons fires together, with an overall intensity of $\sim$ 10 nA. The behavior of this "collective current" is modeled by using the *current dipole approximation*: it is the classical model of magnetic field sources in MEG and it is useful to simulate the flux of magnetic field through a small area [32, 39]. The current dipole model is the simplest one on a spatial level, because any generic current can be estimated by a

linear sum of current dipoles induced by elementary regions. This is justified by the linearity of the Maxwell equations in the source currents [32, 39].
In physics, a current dipole represents a wire of infinitesimal length carrying current, which strength is given by the dipole moment p. In the case of neural currents, the current dipole approximation assumes that the current sources occupy a relatively localized region, concentrated in a single position $\mathbf{r_0}$ [39]. Considering $\mathbf{p}$ as the current dipole moment, it is defined as:

$$\mathbf{p} = \int \mathbf{J}^P(\mathbf{r}')d^3r' \tag{3.1}$$

where $\mathbf{J}^P$ represents the current density due to the sum of the currents produced by the post–synaptic potentials. Such currents are integrated in the small elementary volume (few mm^3) containing few thousands of neurons. The final, cumulative current is also known as *primary current*: $\mathbf{J}^P$ passes through neurons and membranes and represents the interesting signal in neuroscience. In principle, other currents might contribute to the outside magnetic field: the *return* or *volume current* $\mathbf{J}^R$, an extracellular current going passively through the electrically conductive medium around the neurons. It depends on the local conductivity σ of the medium and on the electric field intensity E, so it can be express as $\mathbf{J}^R = \sigma\mathbf{E}$. Then, the overall current is given by the linear sum of the contribution of both the primary and the return currents:

$$\mathbf{J} = \mathbf{J}^P + \sigma\mathbf{E} \tag{3.2}$$

The electric current can flow in closed loops or can discharge in particular points. In any case, the overall charge is maintained thanks to the charge density continuity equation:

$$\nabla \cdot \mathbf{J} + \frac{\partial \rho}{\partial t} = 0\,. \tag{3.3}$$

where ρ is the charge density (in $[Cm^{-3}]$).
Recalling the differential form of the Gauss Law:

$$\nabla \cdot \mathbf{E} = \frac{\rho}{\epsilon_0}\,, \tag{3.4}$$

it is possible to replace both Eq. 3.2 and Eq. 3.4 in Eq. 3.3, obtaining:

$$\nabla \cdot \mathbf{J}^P + \nabla\sigma \cdot \mathbf{E} + \omega_0\rho + \frac{\partial \rho}{\partial t} = 0\,. \tag{3.5}$$

Here, $\omega_0 = \frac{\sigma}{\epsilon_0}$ represents the characteristic frequency of the different neural regions, according to the conductivity value σ of each region. For any brain tissue, this frequency is much larger than the characteristic frequencies of the neural activity, that range between $1 - 1000$ Hz. Even for the skull, which has the lowest conductivity, ω_0 is in the order of 10^9 Hz.
The characteristic conductivity value is not known for every brain location, so, in a semi–realistic head model, a unique approximated σ value is assigned for each region. The brain, the skull and the scalp are the macro–regions considered to be homogeneous and to have approximately the same σ (see Fig. 3.4). Inside these regions, the electrical conductivity is assumed to be constant, i.e. $\nabla\sigma = 0$. An useful approximation is to assume that the head and its internal regions have a spherical geometry. This way, σ only depends on the distance to the center and the brain, the

skull and the scalp can be considered as concentric spheres. Thanks to this approximation, it is possible to obtain fair estimations of the external electric potential V and magnetic field $\mathbf{B}$. Under these conditions and looking at the Eq. 3.5, it follows that:

- far from the primary current $\nabla \cdot \mathbf{J}^P = 0$, hence any other charge must fall off with time following the exponential trend $\exp[-\omega_0 t]$,
- in the location of the primary current, the charge remains as long as the current flows, then, when $\mathbf{J^P} = 0$, it decades as $\exp[-\omega_0 t]$,
- if $\omega_0 \gg$ neural activity frequency, then $\partial\rho/\partial t$ is negligible compared to $\omega_0\rho$ term.

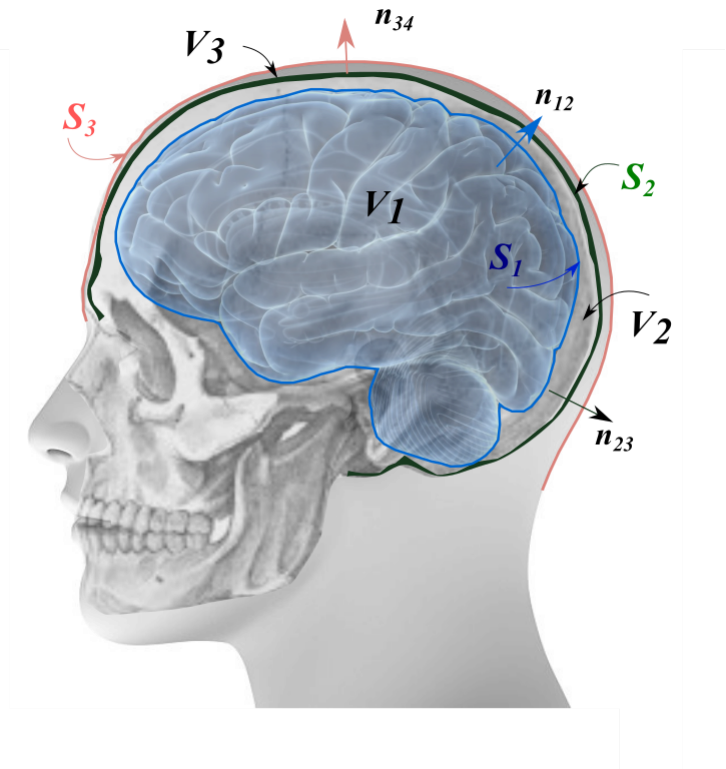

FIGURE 3.4: Schematic representation of the main cerebral regions: the brain (or cortex) (V_1), the skull (V_2) and the scalp (V_3). A separating surface S_{ij}, oriented according to the corresponding versor $\mathbf{n}_{ij}$, is associated to each pair of adjacent volumes, V_i, V_j.

Assuming that the term $\partial\rho/\partial t$ is negligible, the Eq. 3.5 can be expressed as:

$$\nabla(\mathbf{J}^P + \sigma\mathbf{E}) = 0\,. \tag{3.6}$$

The main requirement for the **low–frequency quasi–static approximation** is the term $\partial\rho/\partial t$ is negligible in the case of neural currents. This approximation allows to neglect all the derivatives in time and therefore to rewrite all Maxwell equations in a quasi–stationary form to describe the behavior of neural currents. This is possible because of the spatial scale, frequencies and medium properties of the model that ensure that the system has negligible inductive, capacitive and displacement effects. Although it is not in the scope of this work going into the math details about the

modeling of the neural magnetic field sources, I will summarize few fundamental steps to better understand this approximation and its effects on the magnetic field **B** definition in the neural case. Further details about this topic can be found in the comprehensive books by Hamalainen [32] and Supek and Aine [39].
Let us consider the Maxwell–Ampère equation, that describes the mutual relation between a current and the associated magnetic field:

$$\nabla \times \mathbf{B} = \mu_0 \mathbf{J} + \frac{1}{c^2} \frac{\partial \mathbf{E}}{\partial t} . \tag{3.7}$$

The last term of the equation represents the displacement current, essential term to ensure charge conservation. Nevertheless, in the low–frequency quasi–static approximation such term is negligible. Since both the electric and magnetic fields are time–dependent on the primary current $\mathbf{J}^P$ and the maximum frequency of interest of the neural currents is $\omega \approx 1$ kHz, the time–derivative of Eq. 3.7 is limited as well. Moreover, according to the dipole current definition in Eq. 3.2, the contribution of $\sigma\mathbf{E}$ (where $\sigma = \omega_0 \epsilon_0$) make the term $\mu_0\mathbf{J}$ in Eq. 3.7 larger than $\partial\mathbf{E}/\partial t$ by a ratio ω_0/ω (where $\omega_0 \gg \omega$) [39].
Now, it is possible to estimate the external magnetic field produced by **J** in a generical sampling point $\mathbf{r}'$ [39]. To do this, the Biot–Savart Law (solution of Eq. 3.7) is used, that describes the magnetic field generated by a density current flowing through an infinitely narrow wire:

$$\mathbf{B}(\mathbf{r}) = \frac{\mu_0}{4\pi} \int \mathbf{J}(\mathbf{r}') \times \frac{\mathbf{r} - \mathbf{r}'}{|\mathbf{r} - \mathbf{r}'|^3} d^3 r' . \tag{3.8}$$

The formulation is equivalent to:

$$\mathbf{B}(\mathbf{r}) = \frac{\mu_0}{4\pi} \int \mathbf{J}(\mathbf{r}') \times \nabla' \frac{1}{|\mathbf{r} - \mathbf{r}'|} d^3 r' , \tag{3.9}$$

because $\nabla'(1/|\mathbf{r} - \mathbf{r}'|) = (\mathbf{r} - \mathbf{r}')/(|\mathbf{r} - \mathbf{r}'|^3)$. For ease of reference, from now on $\mathbf{R} = \mathbf{r} - \mathbf{r}'$.
To prove this assumption, we can move forward from from Eq. 3.9, knowing that $\mathbf{J} \times \nabla(1/\mathbf{R}) = (\nabla \times \mathbf{J})/\mathbf{R} - \nabla \times (\mathbf{J}/\mathbf{R})$:

$$\mathbf{B}(\mathbf{R}) = \frac{\mu_0}{4\pi} \left[\int \frac{\nabla \times \mathbf{J}}{\mathbf{R}} dv - \int \nabla \times \frac{\mathbf{J}}{\mathbf{R}} dv \right] . \tag{3.10}$$

The second integral term can be considered negligible if $\mathbf{J} \to 0$ fast enough for $\mathbf{r}' \to \infty$. Since we are in a quasi–static regime, **E** is a conservative field ($\mathbf{E} = -\nabla V$). Thus, we have $\mathbf{J} = \mathbf{J}^P - \sigma \nabla V$ and thanks to the relation $\nabla \times (a \nabla b) = \nabla a \times \nabla b = -\nabla \times b \nabla a$, we obtain:

$$\begin{aligned} \mathbf{B}(\mathbf{R}) = \frac{\mu_0}{4\pi} \int \frac{\nabla \times (\mathbf{J}^P - \sigma \nabla V)}{\mathbf{R}} dv = \frac{\mu_0}{4\pi} \int \frac{\nabla \times \mathbf{J}^P}{\mathbf{R}} dv - \int \frac{-\nabla\sigma \times \nabla V)}{\mathbf{R}} dv = \\ = \frac{\mu_0}{4\pi} \int \frac{\nabla \times (\mathbf{J}^P + V \nabla \sigma)}{\mathbf{R}} dv \end{aligned} \tag{3.11}$$

By using the approximation of homogeneous σ for each brain volume, it follows that the ohmic term given by $V\nabla\sigma$ vanishes and the only contribution to the magnetic field is given by the primary source $\mathbf{J^p}$.

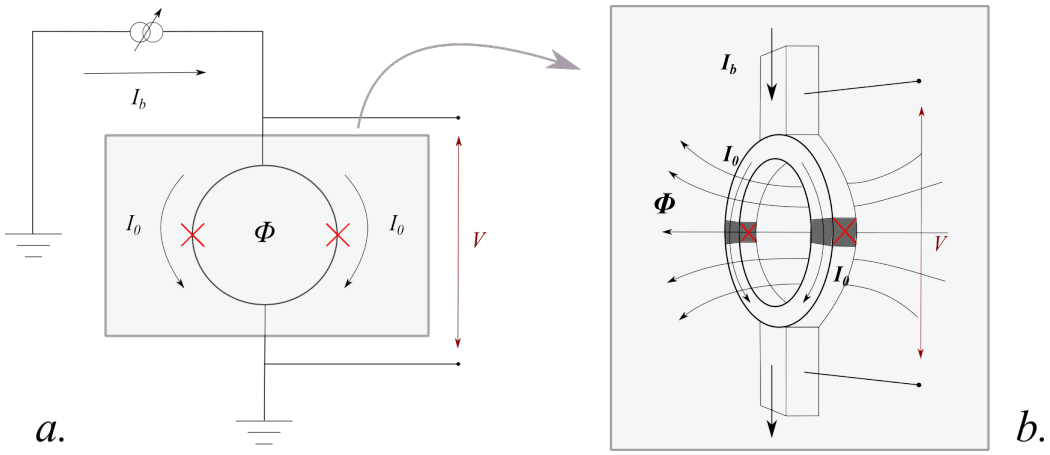

FIGURE 3.5: SQUID ring circuit. Two Josephson junctions (indicated by an "×") are connected in parallel in a superconducting ring.

3.2 MEG signal acquisition

As previously mentioned, we are able to measure the neural magnetic fields if a cortical patch satisfies two conditions: there are enough neurons firing more or less at the same time and their currents are oriented along the same direction.
Thanks to Maxwell equations, it is possible to reconstruct the direction and orientation of such magnetic fields, but their intensity is very low. Thus, a highly sophisticated acquisition system is necessary. This is achieved by means of signal amplifiers, highly sensitive magnetic sensors and by reducing as much as possible the environmental noise. In the following, I give a short overview of the system elements.

3.2.1 Superconductive Quantum Interference Devices

The most important part of the MEG acquisition system is the Superconductive Quantum Interference Device (SQUID). A SQUID is a magnetic flux to voltage converter and a detector of the magnetic flux concatenated to its main component, a low–temperature superconductor ring. This is the most common device configuration used in MEG scanners, known as dc SQUID: it consists in a superconducting ring, with a diameter of $\sim$ 0.1 mm, interrupted by two superconductive junctions, connected in parallel, as I will explain in the following (Fig. 3.5). Such configuration has the best performance in noise reduction and a simpler readout electronics compared to its radiofrequency counterpart (rf SQUID) [32].
It is a very delicate sensor, because the electrostatic shocks and strong magnetic fields can deteriorate its performances [41]. For these reasons the whole acquisition apparatus must be located in a shielded environment, isolated from noise as much as possible.
In the following, the four superconductive phenomena on which the SQUID functioning is based will be introduced:

- the complete loss of electrical resistance below the critical temperature T_c,
- the perfect diamagnetism because of the absence of magnetic flux inside the superconductor below the critical, temperature T_c,
- the magnetic field quantization inside a superconductive ring,
- the Josephson effect.

The most of MEG systems use low–temperature Nb–based SQUIDs. The Niobium (Nb) cooled down below its critical temperature $T_c = 9.2$ K has a superconductive behavior. Moreover, it is a refractory and reliable material when exposed to repeated thermal cycles between room temperature and 4.2 K, the actual working temperature. The basic element of a SQUID is the Josephson junction ($Nb/AlO_x/Nb$), that allows to exploit macroscopic quantum phenomenon, the Josephson effect. This is a phenomenon related to superconductivity: a current flows indefinitely, without an applied voltage, through a Josephson junction or another kind of not-superconducting link (weak link). Although looking into quantum mechanics and mathematical details related to the SQUID functioning is out of this thesis purposes, it is still worth giving a general idea about how this device works and what is the origin of the sensor output we actually use in our work.
A Josephson Junction (JJ) is made of two superconducting stripes - the electrodes - in Nb divided by an insulator of AlO_x. The JJ is based on the tunnel effect through an insulator layer: the subtle insulator region is the tunnel barrier and behaves in different ways according to temperature. For $T < T_c$, Nb becomes superconductive and behaves like a Bosonic condensate: it means that, under the critical temperature, the overall interaction between two electrons becomes slightly attractive because of the electron interaction with the ionic lattice of the metal. This phenomenon enables the formation of electron pairs (a.k.a. Cooper pairs) that behave as a single Bosonic system. The Cooper pairs underpin the superconductivity phenomenon and allow a current through the tunnel barrier, without generating any dissipation and resistance[1].The maximum value of this spontaneous supercurrent is known as critical current I_c.
Another important characteristic of a superconductor is that when it is cooled down under its critical temperature T_c and put in an external magnetic field $\mathbf{B}_{ext}$, every magnetic flux line is expelled from the bulk of the superconductor, remaining confined within the ring [22]. This behavior is known as the *Meissner effect*. Once $\mathbf{B}_{ext}$ is turned off, a current I_Φ is induced inside the ring maintaining the flux constant through it. This current does not decay thanks to the superconductor null resistance and it is estimated as $I_\Phi = -\Phi/L$, where L is the ring inductance [22]. In these conditions, another quantum effect emerges, the *flux quantization*: the trapped flux inside the superconducting ring can assume only discrete values, existing only as integer multiples of the quantum magnetic flux $\Phi_0 = h/2e = 2,07 \times 10^{-15}$ Wb [22, 32].
It results that if an external magnetic field $\mathbf{B}_{ext}$ is applied perpendicularly to the junction, the maximum superconducting current flowing through the junction has a periodic value, depending on the magnetic flux contained in the junction [37]. Its period is $h/2e$, equal to the quantum magnetic flux value.
In order to polarize the SQUID ring, a bias current I_b is externally injected. Only if $I_b \geq 2I_c$, the system is in its operative state, between the superconducting behavior and the resistive one. In this state, both the largest voltage swing (maximum output value) and gain $dV/d\Phi$ (signal amplification) are guaranteed [62]. Fixed $I_b \geq 2I_c$, if an external flux Φ_e is coupled to the ring, the ΔV across the SQUID loop changes. The voltage fluctuates periodically, with period Φ_0 and according to Φ_e values, providing a method to quantify external flux variations.
To simplify the measure, it is possible to use an external feedback coil to keep constant the magnetic flux through the superconductive ring, locking the SQUID in a fixed point of the voltage–flux characteristic curve (its operating point) [22, 62]. The

[1] This concepts are effectively explained in a video–lecture given by John Clarke [58].

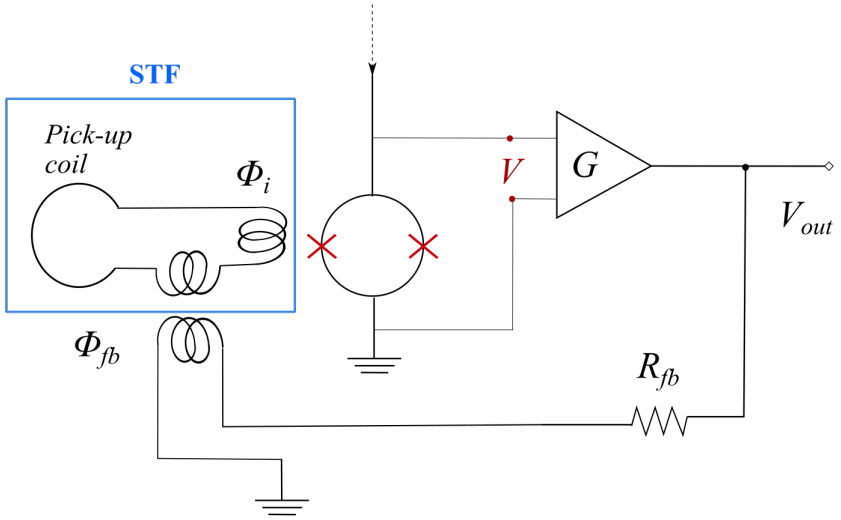

FIGURE 3.6: MEG sensor circuitry. The central ring is the SQUID, with the Josephson Junctions marked with red crosses. In the blue square is highlighted the superconducting flux transformer, consisting in a pick–up coil that collects the brain signal, and two multiturn input coils, one coupled with the SQUID loop and the other with the feedback coil.

SQUID operates in *flux–locked loops* (FLLs) and, thanks to a proper read–out electronics, the output voltage becomes linearly proportional to the input flux change [22, 41, 62]. There are two advantages in using this system: firstly, the sensor answer is linear and secondly, the device can be used on a wider dynamic range ($\sim 10^5\Phi_0$). The feedback coil compensates Φ_e reducing the magnetic field excursions around the SQUID operating point. To obtain the least total variation of the magnetic flux inside the SQUID, the loop gain of the FLL must be as larger as possible. Thanks to this feedback, large magnetic field fluxes can be applied without deflecting SQUID from its operative state [62]. The circuit is shown in Fig. 3.6.

3.2.2 Superconducting flux transformers

To guarantee an effective measure of the weak MEG signal by using a SQUID, a *superconducting flux transformer* (SFT) is necessary. It comprises 2 coils: the first is the pick–up coil and the second is a multiturn input coil coupled with the SQUID loop [41](see Figure 3.6). The whole system is in superconducting material in order to guarantee the complete absence of both circuit resistance and induced magnetic field.The main purpose of the pick–up coil is to increase SQUID sensitivity. The coil is located as close as possible to the head and it has an area $\geq$ 1cm^2: this ensures a larger impedance ($0.1 - 2\mu$H) than the SQUID loop ($\sim 10^{-10}\mu$H) and thus a larger voltage response to small currents. The SQUID itself cannot be enlarged too much because the intrinsic flux noise increases with SQUID inductance; at the same time, its loop sizes must be greater than $\sim 100\mu$m to ensure an effective magnetic flux coupling with the input coil.
Operationally, when a magnetic field applies to the flux transformer, the pick–up coil detects it and a screening current starts flowing through the circuit. Then, such current is turned into magnetic flux through the input coil coupled with the SQUID. In a

typical design, a magnetic field of 0.5 nT measured by the pick–up coil corresponds to $1\Phi_0$ in the SQUID [41].
It follows that the pick–up coils are fundamental components of the sensor circuitry and they have to be chosen carefully. There are two most common pick–up coil classes for MEG signal detection, the **gradiometers** and the **magnetometers**.
The gradiometers can have two possible configurations, axial and planar. The first one has an optimal sensitivity to deep sources, but a complex assembly process. The second one is better suited for shallow sources, but only when the current dipole axis is perpendicular to the field derivative direction of the gradiometer. However, the most common used pick–up coil in magnetoencephalography is the magnetometer: it has an optimal sensitivity both to deep and superficial sources, although it is very susceptible to environmental noise.

3.2.3 Magnetic Shielded Room

The correct choice of pick–up coil configuration depends largely on how well the MEG scanner location is shielded by noise. Unfortunately, in most cases, the apparatus is located in urban environment, as hospitals or laboratories, where the background noise is several orders of magnitude greater than the brain signal. In facts, neural magnetic fields are extremely low signals, $\sim 10^6$ times lower than the Earth's magnetic field ($\sim 50\mu$T). In many cases, the acquisition systems are located in magnetically shielded rooms (MSRs), trying to reduce environmental noise. All the instruments that can produce magnetic field (as control electronics, computer for signal processing and analysis, an so on) are kept outside to avoid interference during the measurements. Nevertheless, the insulation is not perfect because of the necessary holes to pass instrumentation wires. In most cases MSR are made in Ni-alloy.

3.2.4 System configurations

The acquisition system do not consists, obviously, in a single sensor (SQUID and SFT), but in array of hundreds of sensors. For MEG measurements, the standard configuration is shown in Figure 3.7: it consists in a helmet–type sensor array, dipped in a liquid–helium dewar, that cools down the superconducting elements under their critical temperature.
There are different configurations in which the MEG apparatus can be designed. According to this and to the acquisition needs, there are also different position of the subject during signal recording, an important aspect to take into account to reduce artifacts due to head movements. Some systems are realized to perform supine acquisitions; in other cases the subject is seated. As previously mentioned, the acquisition can be performed during the execution of different tasks or simply at rest. In this last case, the subject can be asked to close the eyes or to fix a luminous point. The resting–state MEG recordings used in this work were acquired with the subjects at rest, supine and with open eyes, fixing a red crosshair on a dark background [61].

3.3 The MEG scanner

The data used in our analysis belongs to the open–access databases of the Human Connectome Project (HCP) [1]. We were interested in MEG time series of healthy subject in resting state condition. The release manual of HCP data (available at [61]) explains that the acquisition of our dataset were performed by using a whole–head

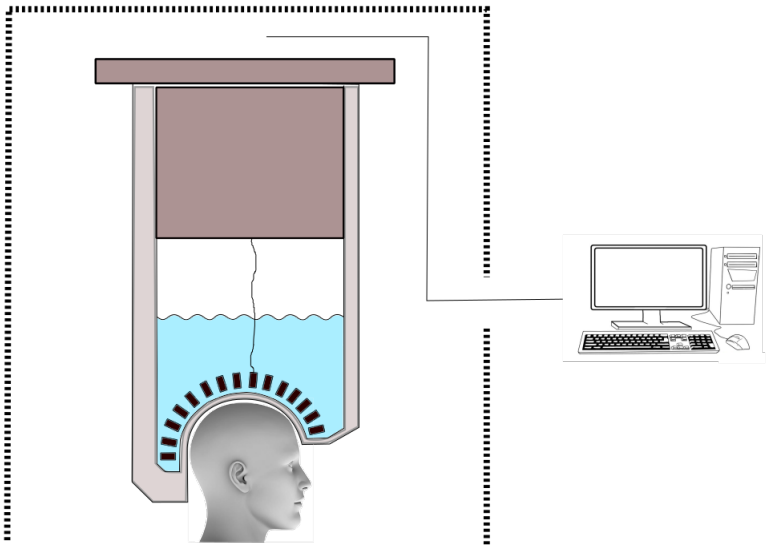

FIGURE 3.7: Schematic representation of MEG acquisition system.

Whole-head MAGNES 3600 – Technical specifications	
RMS noise	$\sim$5 fT/$\sqrt{\text{Hz}}$
Sampling rate	2034.5101 Hz
Electrode impedence	<10 kΩ
Bandwith	400 Hz
HPF (high pass filter)	DC
Acquisition Mode	continuous
Data encoding	delta

TABLE 3.1: Technical specification of whole-head MAGNES 3600 MEG scanner. The magnetic flux sensitivity (expressed in root mean squared -RMS- noise) is an average value in the white noise range ($>$ 2Hz). The intrinsic noise limiting factor of a magnetometer is the thermal noise of the SQUID itself, other contributions are negligible [32].

MAGNES 3600 (4D Neuroimaging, San Diego, CA) scanner. The system is located in a MSR in the medical campus of the Saint Louis University and is equipped with 248 magnetometer channels with 23 reference channels (18 magnetometers and 5 gradiometers). System technical specifications are shown in Table 3.1.
Together with MEG acquisition, other recordings are synchronously performed: two channels are devoted to electroculography (EOG), one to electrocardiography (ECG) and four to electromiography (EMG). All these acquisitions are essential to remove artifacts in MEG signals.
The subjects are in supine position during the recording. The crown of the head touches the posterior part of the MEG dewar, without pressure and the whole back of the head and the front part until the eyebrows is inside the dewar. The rest of the face is free.
For each subject an MRI anatomical acquisition is independently performed as well. In order to co–register MEG data to MRI structural scans it is necessary to define a subject system reference by using location coils. Three-anatomical positions are used

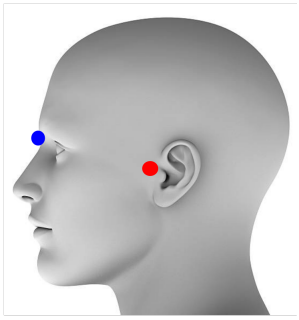

FIGURE 3.8: Positions of the reference sensors for MEG signals co–registration. The red point identifies the pre–auricular position and the blue one the nasion.

as reference, the nasion and the two pre–auricular points (see Figure 3.8).

3.4 Source space reconstruction: Forward and Inverse Problems

The most important issue in MEG is the reconstruction of the source space from the recorded signals. To do this, the resolution of two fundamental problems have to be addressed: the Forward Problem and the Inverse Problem. Both of them will be briefly described in the following paragraph in order to give some ideas about the source reconstruction process. For further details, the books of Hamalainen [32] and Supek and Aine [39] are still recommended.

The Forward Problem The forward problem (FP) resolution is of major importance to compute the spatiotemporal activity of the neural sources. Its resolution allows to estimate which can be the source distribution that is able to produce the external magnetic fields (MEG), recorded by a finite set of sensor locations [51]. It is fundamental to solve this problem to estimate a possible pattern of source localization.

FIGURE 3.9: Stylized representation of activated neural sources and of the fields produced by them. Above the head, the helmet–shaped array of SQUID sensors.

As mentioned above, the electromagnetic sources of interest for MEG are the primary dipole currents. They represent the neural activity areas related to cognitive, motor and sensory processes.
Consider $\mathbf{r}$ as the spatial location of the current dipole and assume a sampling position $\mathbf{r}'$ to measure the magnetic field: the contribution of the primary current to Eq. 3.11 can be approximated by:

$$\mathbf{J}^P(\mathbf{r}) = \mathbf{p} \times \frac{\mathbf{r} - \mathbf{r}'}{|\mathbf{r} - \mathbf{r}'|^3}, \tag{3.12}$$

equivalent to:

$$\mathbf{J}^P(\mathbf{r}) = \mathbf{p}\delta^3(\mathbf{r} - \mathbf{r}'), \tag{3.13}$$

where $\mathbf{p}$ is the moment of the single current dipole assumed to produce $\mathbf{J}^P$ and δ is the Dirac delta function.
The magnetic field lines of a single current dipole are shown in Fig. 3.10.

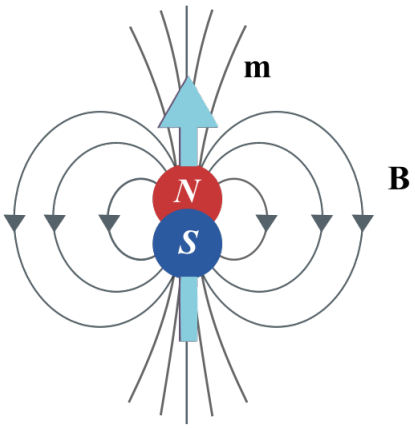

FIGURE 3.10: Graphical representation of the magnetic field produced by a current dipole. The blue arrow represents the dipole moment.

Since the magnetic field has two components, one radial $\mathbf{B}_R$ and one tangential $\mathbf{B}_T$, it is important to specify the geometry used to model the subject head. This allows to understand the different contribution of the two components in the resulting magnetic field outside the brain and their influence in the correct sources localization. For the sake of simplicity, the geometry used is the spherical approximation. However, in some conductors with a finite geometry, as the spherical one, the volume current generates a magnetic field equal and opposite to that produced by the primary current: it means that only the tangential components produce a magnetic field detectable outside the head, whereas the radial ones are externally silent (Fig. 3.11).
A real brain is constituted by different tissues that are characterized by inhomogeneous conductivity values (σ). Nevertheless, for the sake of simplicity, the simplest and common model of the human head approximates its main tissues (brain, skull and scalp) as concentric spherical volumes, each one with a constant value of conductivity.
The influence of dipole orientation on the resulting $\mathbf{B}$ with respect to the conductor geometry is explained by the Sarvas formulation:

$$\mathbf{B}(\mathbf{r}) = \frac{\mu_0}{4\pi F^2}\left[F\mathbf{p} \times \mathbf{r}_0 - (\mathbf{p} \times \mathbf{r}_0 \cdot \mathbf{r})\nabla \mathbf{F}\right] \tag{3.14}$$

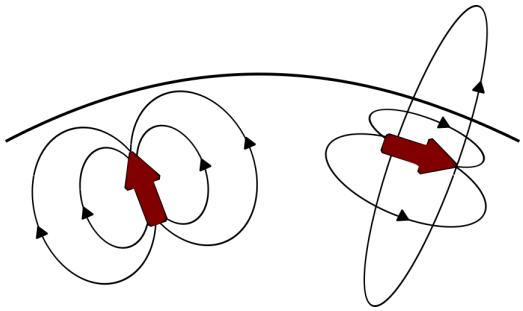

FIGURE 3.11: Magnetic flux lines of a magnetic source inside a spherical conductor. In the picture is shown that, for a radial source, the magnetic flux lines cannot go outside the conductor, resulting externally silent. On the contrary, a source tangentially oriented produces the external strongest signal to pick up.

with $F = a(\mathbf{r} \cdot \mathbf{a} + ra)$ and $\mathbf{a} = \mathbf{r} - \mathbf{r}_0$. In Eq. 3.14, $\mathbf{p}$ represents the dipole, $\mathbf{r_0}$ its brain location and $\mathbf{r}$ the position of the sensor.
The Sarvas formula is the standard tool for the resolution of the forward problem, allowing to estimate the magnetic field produced by a current dipole [33]. It defines the spherical model, that is independent from the radial component of the dipole and from the return current contribution, that is considered only implicitly in the formulation.

The Inverse Problem The second, but no less important, problem in source space reconstruction is that known as Inverse Problem (IP). It aims at localizing the source neural currents starting from the electromagnetic fields measured outside the head. The source space reconstruction is the actual target of the whole analysis. This prompts the question as to why is necessary to compute the forward problem. The reason is that, no matter the quality of the data of the amount of available sensors, there will always be a part of information externally non–measurable. Such effect is clarified by the Helmholtz condition: it states that is impossible to reconstruct the current distribution of a conductor body only by measuring the external electromagnetic field. This is due to the presence of magnetically or electrically silent sources inside the conductor. Some examples of these troubling geometries are, as in the MEG case, a current dipole oriented along the radius inside a spherical conductor. In this case, the dipole results magnetically silent. Alternatively, a loop in a conductor produce an external $\mathbf{B}$ that can be measured, but its electric potential V is null outside the conductor. Moreover, there are configurations of current distributions that are both magnetically and electrically silent, or that are too deep with respect to the conductor surface. Thus, it is necessary to solve the forward problem to obtain a possible distribution of the source locations; then, by starting from that distribution, the resolution of the inverse problem tries to reproduce the measured signals. The advantage in measuring MEG signals is that the magnetic field is able to pass through regions with null electric conductivity, in contrast to what happen to the electroencephalographic (EEG) signals.
In general, solving an inverse problem is a method to obtain information about a physical object or system by using indirect measures. The problem consists in the reconstruction of the primary currents $\mathbf{J}^P$ (the field sources) distribution, by measuring the magnetic field and, where necessary, the electric potential.
At this stage, I will consider only the magnetic field information. Given a N number of MEG sensors, the inverse problem can be written as a set of integral equation as:

$$f_i(t) = \int_V \mathbf{L}_i(\mathbf{r}') \cdot \mathbf{J}^P(\mathbf{r}', t) d^3r' + \xi_i(t), \quad i = \{1, \ldots, N\} \,, \tag{3.15}$$

where f_i represents the signal measured by the i–th sensor, whereas $\mathbf{L}_i(\mathbf{r})$ is a vectorial function, known as *lead field*. It represents the sensor response to the unit current dipole in the r position, and depends on $\sigma(\mathbf{r})$ and on the configuration coil of the magnetometer. The integration is estimated on the volume V occupied by the current and the last term ξ_i represents the noise relating to the i–th sensor.
Since the number of available sensors is much smaller than the current dipoles to model (10^2 sensors against to 10^4 dipoles) and that it is impossible to externally measure silent sources, such inverse problem is ill–posed. In general, an ill–posed problem can have three possible outcomes:

1. the solution does not exist,
2. there is not a single solution,
3. the solution changes dramatically with small variances of the initial conditions.

Unfortunately, the reconstruction of MEG sources in Eq. 3.15 can express all three possibilities, that is:

1. it may not exists a single primary current distribution $\mathbf{J}^P$ corresponding to the measured data,
2. there may be more than one possible current distribution able to arise that measured data,
3. the result of Eq. 3.15 could be extremely sensitive to little variations of the measured data.

Aware of those questions, the resolution of the inverse problem is set as follows.
As mentioned above, the neural currents are considered in terms of known sources, and, in particular $\mathbf{J}^P$ can be represented as the sum of an infinite sum of single current dipoles, as clear extension of Eq. 3.13:

$$\mathbf{J}^P(\mathbf{r}) = \sum_{j=1}^{M} \mathbf{p_j} \delta^3(\mathbf{r} - \mathbf{r}_j) \,, \quad j = \{1, \ldots, M\} \tag{3.16}$$

where $\mathbf{r}_j$ represents the locations of the M dipole sources. Then, we replace Eq. 3.16 in Eq. 3.15, obtaining:

$$f_i(t) = \sum_{j=1}^{m} L_i(\mathbf{r}_j) \cdot \mathbf{p}_j(t) + \xi_i(t) \,. \tag{3.17}$$

The signal is the product of the lead field $L_i(\mathbf{r}_j)$ and the current dipole $\mathbf{p}_j(t)$, both referred to the $\mathbf{r}_j$ position. At this point there are two possibilities: the dipole locations are known thanks to anatomical data obtained by MEG imaging techniques [verificare], then $\mathbf{p}_j$s can be found by solving a linear equation system; in the other case, the locations $\mathbf{r}_j$ are unknown variables and the problem becomes non–linear.
To simplify calculations, it is possible to express Eqs. 3.17 in matrix form as:

$$\mathbf{f} = \mathbf{K}\mathbf{q} + \xi \,, \tag{3.18}$$

where $\mathbf{f}$ is the column vector of the measured data and $\mathbf{q}$ that of current dipoles, whereas $\mathbf{K}$ is the *gain matrix*. The $\mathbf{K}$ elements are the lead field function components,

for every sensor and for every current dipole spatial component. The resulting matrix dimension is $N \times 3M$, where N is the number of sampling points (i.e., the sensors) and M represents the dipole locations (that must be considered in their 3 spatial components):

$$\mathbf{K}(\mathbf{r}_1, \ldots, \mathbf{r}_M) = \begin{bmatrix} (L_1(r_1))_x & (L_1(r_1))_y & \ldots & \ldots & (L_1(r_M))_x & \ldots & (L_1(r_M))_z \\ (L_2(r_1))_x & (L_2(r_1))_y & \ldots & \ldots & (L_2(r_M))_x & \ldots & (L_2(r_M))_z \\ \vdots & \vdots & \vdots & \ddots & \vdots & \vdots & \vdots \\ (L_N(r_1))_x & (L_N(r_1))_y & \ldots & \ldots & (L_N(r_M))_x & \ldots & (L_N(r_M))_z \end{bmatrix} \tag{3.19}$$

Many possible algorithms to solve the inverse problem have been proposed [cit]. However, regardless the kind of method used, the aim is to minimize the cost function:

$$||\mathbf{f} - (\mathbf{Kq} + \xi)||_2^2 \tag{3.20}$$

Despite the refinement in the reconstruction algorithms, because of the ill–posed nature of the inverse problem, many kind of errors can happen as I will briefly explain in the following.

3.4.1 Space blurring, source–leakage and artifacts

In order to study connectivity, MEG signal correlations can be performed either in the sensor space, by directly using the sensor recordings, or in the source space, by reconstructing the source locations and their corresponding signal. However, it is quite inadvisable to perform any analysis in the sensor space, because of many issues that might occur during the acquisition. For example, although MEG signal suffers little effects of volume conduction, the signal of a single dipole can be recorded by multiple sensors, in the same way as a single sensor can receive more than one signal from different sources [54] (simplified explanation is showed in Figure 3.9).
This effect is known as field spread and it greatly influences the sensor space, that it is consequently not well-suited for connectivity analysis. Moreover, in sensor space the sensitivity to environmental and physiological noise is particularly high. To contain field spread effects, the source–space projection is used. The accuracy in spatial reconstruction is limited, because of the ill–posed nature of the inverse problem, that aims at reconstructing the activity of 10^4 brain voxels by relying on the signals recorded by 10^2 sensors. This problem can produce a spatial coupling of neighboring regions, with a resulting time related behavior. This is due to the fact that the signal produced by a point–like dipole source is spread, by the reconstruction process, on different voxels. In other words, the reconstructed sources could result as highly correlated not because of a real relation between them, but since they share components of the same sensor signal that the reconstruction process assigned to different source locations. Nevertheless, many works related to source space reconstruction states that, given a certain set of assumptions, a reasonable reconstruction accuracy ($5 - 8$ mm of spatial resolution) can be obtained [13]. Moreover, source space projection strongly improves the signal–to–noise ratio.
The source leakage is an effect that affects only exactly zero–phase lag cross–correlations. Although it could be easily removed by simply neglecting that kind of correlations, not all the zero–lag correlations are meaningless and it is therefore not convenient to *a priori* remove all of them. As it will be shown in Chapter 4, in our case, correlations evaluated at zero–lag are the most informative ones, compared to greater lags.

On the other hand, during the source reconstruction other problems can take over. For example, the source mislocalization, that is due to errors in the solution of the forward problem (e.g. the projection of an extended source as a single dipole) or the spatial blurring, where the projection of a source location is spread across a finite volume. The signal spreading can produce an interdependence between the signals belonging to different sources, since the signals produced by a source can "leak" in the estimated signals of another source during the reconstruction process. This effect is known as *source leakage*. It is stronger for deep dipoles, that produce field patterns spatially diffused, and for neighboring sources. Furthermore, it depends from the signal–to–noise ratio of the MEG data. For all these reasons, leakage assessment is not a trivial operation, in particular, in the case of resting–state recordings, because it is not possible to compare the signals with any activity baseline [54].
Recently, many methods to limit this problem were realized: the major part tries to overcome this issue by disregarding zero–lag interaction between sources, that can be due to instantaneous signal spread during the reconstruction process and not to a real correlated activity.
There are three kind of possible correlations: **true correlations** that corresponds to real interactions; **artificial correlations** that are false positive and are the result of reconstruction errors; **spurious correlations** that are the side–product of significant couplings but completely misplaced. Other problems that can affect MEG data are related to the extreme sensitivity of the SQUID sensors, since the recordings are particularly prone to be affected by artifacts, due to environmental or physiological sources [10]. The most common physiological artifacts are eye blinking and heartbeat. They are identifiable for the amplitude and periodicity of their signal, although these characteristics are not always enough to clearly recognize them. The effect of the artifacts can be controlled by accurate experimental design and by removing the most "contaminated" data. As far as it concern the heartbeat, a method to identify its signal is by recording an ECG simultaneously with the MEG acquisition and comparing the wave shapes. The Independent Component Analysis (ICA) is a common algorithm used to separate the contribution of the various sensors and identify the signals affected by artifacts. This technique is data driven and assumes that the observations are a linear superposition of M statistically independent source signals, where M is the number of sensors [10](see Section 2.2.3). We preprocessed the dataset used in this work, by means of the open–access software Brainstorm (see Paragraph 3.4.2), that exploits the ICA algorithm to detect artifacts. In our case, the algorithm was used only to removed the heartbeat component: the heart contribution is particularly easy to identify, and, thanks to the ICA, it can be deleted almost completely before performing the source–space reconstruction. No other components of the signals are altered by this operation, included those related to source leakage. In addition to ICA, there are other methods for artifact rejection as principal component analysis (PCA), factor analysis, state space filtering and so on, which explanation is out of the scope of this thesis but major information can be found in Ref. [12].

3.4.2 The Brainstorm software

To perform the source space reconstruction and the analysis of the artifacts, we used an open–source application developed with MATLAB. It is thought specifically for the elaboration of the great amount of data produced by EEG and MEG to study brain connectivity. Thanks to this software it is possible to perform analysis from

multimodal dataset, constituted by MEG and simultaneous EEG recordings, 3D location of the sensors, anatomical MRI acquisition of the subject's head, or others. The software workflow is constituted by the review and process of MEG and EEG recordings. It is during this phase that is possible to identify the presence of noisy or malfunctioning sensors or any other kind of interference. As mentioned in the previous paragraph, there are two main sources of noise affecting the recordings: the first is the environmental one, due for example to the vibrations of the building in which the MEG apparatus is located and to the power lines with frequencies $50 - 60$ Hz; the second is the noise caused by physiological phenomena, as heartbeats, eye blinking or breathing. According to the nature and amount of noise, frequency filters and specific spatial projections are used to reduce its effect.
Brainstorm is adopted to solve the forward and inverse problems in source space–reconstruction. Starting from the MEG and EEG neural currents, the software uses forward models with boundary elements method (BEM)to estimate the corresponding head model. Then, one of the inverse modeling methods available on Brainstorm are applied to reconstruct the distribution of the cortical sources producing the set of EEG and MEG recordings.
This application also provides tools to perform more advanced analysis of the neural signals, by spectral or time–frequency decompositions, functional connectivity measures, statistical inference and so on. However, we did not exploit these functionality since this part of the analysis was carried out by means of self–developed C softwares.

3.5 Outside MEG: an overview of brain imaging methods

In this part of the Chapter, I will give a general overview of other two most important imaging methods besides MEG used to study brain connectivity. The aim of this digression is allowing an easier comparison between the functional connectivity achievements present in the literature and our results. Firstly, I will introduce the functional magnetic resonance imaging, the pioneering technique in functional connectivity studies; secondly, the electroencephalography, that, measuring the electric potentials produced by neural currents, is the electrical counterpart of MEG.

3.5.1 fMRI and BOLD signal

The functional magnetic resonance imaging (fMRI) is one of the most important method to identify dynamical patterns of brain connectivity. The physiological bases that induce changes in neural activity are basically two: firstly, the magnetic properties of the hemoglobin, depending on whether it carries oxygen – oxyhemoglobine – or not – deoxyhemoglobin; secondly, the substantial growth of the blood flux when the local neural activity increases [14, 43]. As previously mentioned, fMRI is not a direct measure of the neural activity, unlike the electromagnetic signals EEG and MEG. The key process observed to identify the neural activity is the oxygen consumption resulting from the activation of certain regions, or, in other words, the blood oxygenation level. Ogawa in 1990 was the first to hypothesize that such level was a measurable signal and that it would be possible to track its changes. This quantity is known as Blood–Oxygen Level Dependent (BOLD) signal. The hemoglobin, i.e. the protein constituting the blood, carries oxygen, that is a crucial element since it is involved in glucose oxidation, the greatest energy source for brain functionality. When a brain region activates, it calls for oxygenated blood. During oxygen metabolism,

hemoglobin loses its oxygen molecules turning into deoxyhemoglobin, which has different magnetic properties compared to its oxygenated form [56]. This process induces a modification in blood magnetic susceptibility. The difference in magnetic susceptibility between blood vessels carrying deoxyhemoglobin and normal tissues nearby produces magnetic field local distortion. This is due to the fact that the oxyhemoglobin is diamagnetic and the deoxyhemoglobin is paramagnetic. Therefore, the increased amount of deoxyhemoglobin produces a general BOLD signal reduction. Nevertheless, paradoxically, there is an increment in BOLD signal when neural activity increases. During neural activity the amount of oxygen consumption (the oxygen metabolic rate) is much lower than the great volume of still oxygenated blood flowing to the brain because of the activation. Such effect produces an overall decrease in deoxyhemoglobin concentration compared to oxyhemogloblin. The peak in the BOLD signal arises $\sim 4-6$ s after the activation, and then decreases below the baseline when there is a reduction in the blood flow, i.e. the neural activity ends up. The sluggishness of BOLD response is due to the brain vasculature that is not able to react sufficiently fast to the energy demand. Its response is approximately linear with the stimulus, but in some cases there can be deviations from linear behavior due to saturation or refractory effects, e.g. when subsequent stimuli are separated by less than 5–6 s .
Even though the physiological origin of the BOLD signal are more or less known, it is the result of a mixture of effects and the exact contribution of the cerebral blood flown and volume, and of the cerebral metabolic rate of oxygen consumption are not well understood. Moreover, on short time scale the blood dynamics covers the effect of the temporal dynamics of functional connectivity, preventing from the assessment of a clear correlation with the electrophysiological signals. Finally, fMRI is affected by respiratory and heartbeats artifacts, as it happens in the MEG case, that can induce spurious correlations.

fMRI and MEG

The determination of a direct, measurable correlation between BOLD and MEG signal is still an open issue [43, 82]. Although both techniques are measures of neural activity, MEG is mainly correlated to the neural spiking activity in terms of neuronal firing rate; on the other hand, fMRI seems to follow the synaptic activity caused by local processes [43].As previously mentioned, some current sources can be magnetically silent outside the brain: this can be due to their orientation and/or position inside the head or because they are inhibitory neurons. Thus, MEG acquisition system cannot take into account the effects of such currents [25]. However, such currents produce electromagnetic fields that have an actual effect on physiological processes and could be more evident by observing the changes in BOLD signal. As a consequence, it happens that fMRI and MEG results do not coincide, because of the different underlying physiology and physical bases of the techniques. In a recent work of Garces *et al.* [25], they performed a comparison between structural (or, anatomical) networks and functional networks. The first ones were identified by Diffusion Weighted Imaging (DWI), a technique that is able to highlight the fibers bundles of the white matter, i.e. its structural organization; the second ones by using fMRI and MEG. From this study emerges a higher similarity between the structural connectivity and the functional networks found out by MEG acquisitions – filtered at α, β and θ frequencies- - compared to fMRI. Nevertheless, MEG and fMRI shows similarities that uphold the correlation between the two techniques.

The spiking activity seems highly correlated with the electromagnetic signals. It identifies the high–frequency range of brain electromagnetic signal (300–500 up to 6000 Hz) and represents an aggregate signal arising from local spiking activity [47]. "Local", in this context, means a recording volume of 200 μm of radius.
The MEG signal records directly the magnetic fields produced by the synchronous activation of a population of neurons, whereas the BOLD signal seems to be approximately proportional to a local neural activity measure, mediated on several millimeters of spatial extension and several seconds of period [34]. This local neural activity is known also as *local field potentials* (LFP). The LFPs are correlated both with the spiking activity and subthreshold integrative processes occurring, for example, in dendrites. However, the direct measure of this kind of signal is not feasible. The LFPs are the low–frequency components of the brain electromagnetic signal (8–200 Hz) and represent the spatial and temporal overlapping of the synaptic input of a population of neurons [47]. A problem of LFP measure is that it is not possible to exactly determine the brain region where the activity occurs by using "external" methods, as fMRI, because the sufficient spatial resolution is achievable only by a in–brain electrode implantation [14]. On the other hand, MEG is a more suitable method to highlight neural communication regions because it directly measures the actual product of their activation.

3.5.2 EEG

The electroencephalography (EEG) is an electrophysiological technique to globally characterize brain electrical activity [11, 50] by using electrodes directly applied on the scalp [57]. EEG measures the electrical potential difference between two electrodes located in different places on the scalp. A conventional EEG has a clinical setting of 21 electrodes equally spaced [2]. The technique has an excellent temporal resolution (1 ms), very useful in studies of brain dynamics [11]. It is used alongside other neurodiagnostic test to verify the presence of abnormal brain patterns [2], i.e. by checking for epileptic disorders [75], by finding out epileptic features and seizure focus, or by identify metabolic or sleep diseases, dementia, brain death, and so on [57]. Although there are examples of functional connectivity studies by means of EEG information [5], this method is not very efficient since it has the same high temporal resolution as MEG, but there are much larger effects of volume conduction and no information about source locations, producing a lot of difficulties in a correct interpretation of signal correlations in sensor space.

EEG and MEG

Both EEG and MEG are fundamental in the study of cognitive process dynamics thanks to their high temporal resolution. They play an important part in brain connectivity measures, both physical and functional. The two methods are related because their signal source is the same (the neuronal ionic currents produced by biochemical processes), but each one is sensitive to a different component of the electromagnetic field [69].
Compared to fMRI, EEG and MEG have a much better temporal resolution, whereas their spatial resolution is not equally competitive ($\sim$ 1 cm and $\sim$ 1 mm, respectively for EEG/MEG and fMRI).
An important aspect for EEG and MEG signals is their mutual independence. This property ensures the complementarity of brain electrical activity information provided by the two techniques.

This is justified by the Helmholtz theorem that states that a general vector field $\mathbf{A}(\mathbf{r})$, that approaches zero when $\mathbf{r} \to \infty$, can be represented by the sum of two vector fields $\mathbf{X}(\mathbf{r})$ and $\mathbf{Y}(\mathbf{r})$, one irrotational ($\nabla \times \mathbf{X} = 0$) and one solenoidal ($\nabla \cdot \mathbf{Y} = 0$). These requirements are satisfied for an electromagnetic field: the electric field is conservative ($\mathbf{E} = -\nabla V$) because of the quasi–static approximation [51], and the magnetic field is solenoidal (condition that is always true). Thank to such theorem gives us the guarantee of the independence of the two components, and thus, of the two acquisition methods.

3.6 MEG in brain connectivity

As described in the Introduction, brain connectivity can be defined in different ways, according the characteristics –anatomical or functional– observed. As regards functional connectivity, it studies the way the different brain regions communicates and their role in normal brain functionality. Since the seminal work by Biswal *et al.* [7], the most used technique to investigate brain connectivity is fMRI. However, in recent years MEG is living its moment of glory: thanks to a more advanced technology, in terms of hardware and computer processing power, together with improved modeling algorithms, a broad, interregional scale of observation and an unbeatable spatial and temporal resolutions (1 ms and 5 mm respectively), it results to be a powerful method to obtain novel insights in human brain functioning and connectivity [53]. Thanks to these characteristics and the advantage to be a direct measure of the electrophysiological brain activity, MEG results to be particularly suited in the study of resting state networks (see Section 1.2.3). Many works tried to reproduce the functional connectivity patterns obtained with fMRI by using MEG. De Pasquale *et al.* in their work of 2010 [17] showed that two well–known RSN in fMRI, the DMN and the DAN (see Section 1.2.3), were recognizable by using MEG signals as well. Brookes *et al.* in 2011 were the first to test the MEG capability to identify functional connectivity networks during resting state independently from fMRI, demonstrating the neural basis of their spatial patterns. It follows that fMRI and MEG methods are related since both measure neural activity, however the underlying physiological phenomena producing the measured signals are different. For these reason, the connectivity patterns obtained with the two techniques are not completely overlapping although very similar. In order to better understand difference and similarities of resting state structures obtained by such methods, Garces *et al.* [25] compare the functional connectivity results achieved by fMRI, MEG with another imaging technique, the diffusion weighted imaging (DWI), used to assess the anatomical structure. Although their level of comparability changes according to the signal frequency band used in the analysis, it emerges that the three method are related but they give information of complementary nature. Resting–state spatial patterns have a stable structure across subjects, as we saw in Section 1.2.3. Nevertheless, a certain level of inter–subject variability is still present, due to gender, age, presence of pathology, and genetic characteristics. This was identified by using fMRI as a sort of functional connectiviy fingerprint of the subject, but it was recently confirmed by Demuru *et al.* [18] by means of MEG signals. Some attempts to estimate connectivity between MEG acquisitions in the sensor space were performed but without a great success, because of field spread effects between the acquisition channels: it prevents from a perfect one-at-one correspondence between the signal source and the sensor, that receives overlapping signals from multiple source locations, as explained in 3.4.

3.7 Pre–processing of a MEG recording

In this chapter, I gave a general overview of the most important aspects concerning magnetoencephalography, in terms of physiological origins of the signal detected, acquisition system and reconstruction methods. The result of all these steps is the MEG signal that is actually used in the measures of functional connectivity. At this point, it possible to join this digression to what I discussed in Chapter 2. The methods for times series analysis described there are absolutely general and applicable to any kind of time series, MEG signals included. However, it is often necessary to perform some additional pre–processing steps before proceeding with connectivity analysis.
In the following, I am going to describe such steps.

3.7.1 A MEG time series

A MEG raw recording is a time series of few minutes of length (6 min for resting–state acquisition up to 14 min for task–drive stimulations), sampled at a rate of 2034.5 Hz in the case of the Human Connectome Project (HCP) hardware (see 3.3) for a total amount $> 7 \cdot 10^5$ points. A MEG signal is the result of the magnetic field modulation produced by the neural currents. It is characterized by intrinsic oscillations over a broad range of frequencies (from 0 to 1000 Hz) both in resting–state and during task [12]. These oscillations are organized in frequency bands that modulate in different ways in response to a stimulus. For these reasons, in some studies [13, 17] statistical analysis are performed after a signal pre–filtering, in order to separate the contribute of the various bands. Such frequency bands are divided in delta ($0.01 - 4$ Hz), theta ($4 - 8$ Hz), alpha ($8 - 13$ Hz), beta ($13 - 30$ Hz), gamma ($30 - 200$ Hz) [12, 53].

Filters and other cleaning

When a MEG acquisition is performed, two kinds of approach can be followed. The first estimates brain connectivity analysis in *sensor space*, by directly using the signals acquired by the MEG sensors. As described in Section 3.4.1, this approach has a lot of drawbacks, as high sensitivity to noise, artifacts and extremely low spatial resolution. On the other hand, the second method is based on the reconstruction of the source space and of the signals produced by each of them. However, before proceeding with the source space reconstruction, as explained in Section 3.4, it is necessary to clean the time series up by the noise contribution and the physiological artifacts, since they could spoil the reconstruction process.
Since the power line is one of the major sources of environmental noise, it is necessary to remove the main transmission frequency (60 Hz in our case) and all its upper harmonics (namely 120, 180, 240,300 Hz). This is performed by means of a notch filter, i.e. a band–stop filter that rejects or attenuate the frequencies within a narrow stopband range B, without affecting all the others above and below B. Then, a high pass filter is applied to remove all the frequencies below 0.3 Hz.
In this phase, artifacts and spoiled acquisitions due to malfunctioning sensors are removed as well. By using the open–source software Brainstorm (see Paragraph 3.4.2) it is possible to visualize the time series recorded from all the sensors, checking their shape: if they look flat or their waveform is completely different from the other acquisitions they can be manually marked as “bad channels”, excluding their recordings from the following operations of source–space reconstruction.

The last operation is related to the removal of artifact signals produced by physiological phenomena (see Paragraph 3.4.1). To facilitate the cleaning operation, electrocardiographic (ECG) and electroculographic (EOG) recordings – simultaneously acquired with MEG signals– are available for every HCP subject (see Paragraph 3.3). This way, it is easier to recognize the recordings affected by heartbeats or eye–blinking respectively, by comparing the ECG/EOG waveforms with the recording shapes. Here again, the artifact detection is performed by using Brainstorm.

Signal processing

After the pre–processing operations, MEG signals are ready to be used in connectivity analysis. In many cases, other operations are performed before proceeding with the source–space reconstruction (see Section 3.4) and the measure of brain connectivity. For example, the most common one is the filtering of the signals according to delta, theta, alpha, beta and gamma band frequencies. Then, it is possible to move on with the truly interesting part of the analysis: the reconstruction of brain networks. The most used methods to estimate brain connectivity were presented in Chapter 2, whereas in Chapter 4 the statistical method developed during my PhD work is presented.

Chapter 4

Cross–correlation analysis of MEG signals

In Chapter 3 I talked about magnetoencephalography, its basic functioning and acquisition system and its biomedical applications. As I previously explained, MEG is a powerful tool in the study of brain network dynamics, thanks to its high temporal resolution and a whole–head coverage of the acquisition system. In the last decade, MEG has been frequently used to investigate resting state networks (RSNs), that have a great functional and clinical relevance because of their importance in understanding the nature of the connectivity between brain regions [13].
Functional MRI (fMRI) has always been the most popular tool to investigate neural connectivity. During the last decade, a lot of works focused on the comparison between fMRI and MEG results, by testing the existence of a correlation between the two signals. An issue comes from the lack of a complete understanding of the physiological correlation between neural activity and blood–oxygen level dependent (BOLD) signal (see Section 3.5.1), because it is still not clear whether the functional networks measured by means of hemodynamic signals had also an electromagnetic origin [13, 17]. Another observation arose from such comparison: MEG signal behavior seems to mirror fMRI results, but MEG high temporal resolution pointed out the non-stationarity of the electromagnetic signal. It means that it is not always possible to observe the same fMRI functional neural networks by merely estimating correlations between the whole MEG signals recorded from the different brain voxels, but a better reconstruction is possible by evaluating correlation over an optimal window width. It follows that the particular functional network configuration we observe is strictly dependent from the time resolution we use to investigate it.
De Pasquale et al [17] addressed the comparison between both imaging techniques in the study of two particularly robust and well–studied RSNs, the DMN and the DAN (see Paragraph 1.2.3). Starting from the correlation maps estimated on fMRI acquisition, the authors identified the brain regions belonging to the two RSNs, with the goal of verifying the existence of a significant correlation between MEG recordings picked up from the same regions pointed out by fMRI. The signals actually used in the calculations (as it will be described shortly) are source–space, wide–band, power time series calculated from the original recordings. For each RSN, MEG correlation maps are obtained starting from the MEG power time series corresponding to 4 regions, referred to as *seeds*, identified by fMRI. Then, the correlation between the low frequency fluctuations of the power time series of the seed voxels and other nodes of the set, both included and external to the RSNs, was estimated.
From this analysis, a different connectivity network topography compared to fMRI results emerged. To understand the origin of such differences, de Pasquale et al investigated the temporal dynamics of the power fluctuations, by observing their

correlations at different time scales. It came out that those fluctuations are non–stationary: the correlations between brain regions change on timescale of tens of seconds. By analyzing the spectral properties of the correlations, the authors found out an optimal temporal window (*epoch*) of 10 seconds: this value was justified because of the presence of a moderate peak at the frequency $f \sim 0.1$ Hz ($1/f \sim 10$s) in the spectral analysis of both RSNs, estimated for every subject and mediated over the whole sample. They corroborate this result by means of an algorithm (maximal correlation window, MCW) that identifies the optimal temporal epoch by which the correlation within a subset of nodes belonging to each RSN is maximized and, at the same time, is minimal with a node considered external to the network. The correlation map estimated by using a 10 s correlation epoch maximize the similarity with the map obtained by fMRI.
The work of de Pasquale et al was of inspiration for ours to better define the selection of an "optimal window" in order to compute the cross–correlation and to possibly further improve the statistical robustness.
We proposed a new method to estimate cross–correlation between signals recorded from a set of nodes and to determine the presence of links between those nodes, in order to reconstruct a network.

4.1 Dataset and preprocessing

We started collecting a dataset of 5 subjects randomly selected from the free access database Human Connectome Project (HCP, see Paragraph 3.3). Three $\sim$ 6–minute long resting–state MEG recordings are available for each subject, along with an MRI brain anatomy, an electrooculographic (EOG) and an electrocardiographic (ECG) recordings.
Each MEG recording has 248 components, one for each sensor of the MEG scanner (see Paragraph 3.3), sampled at a rate $f_s = 2034.5$ Hz. For the resolution of the inverse problem and the reconstruction of the source–space, the open–source Matlab application Brainstorm was used. It relies on an Independent Component Analysis (ICA) algorithm to automatically classify MEG components and, by also relying on EOG and ECG, to recognize the presence of artifacts in the MEG recordings. Finally, we manually checked the presence of malfunctioning sensors (*bad channels*) in order to exclude them from the source–space reconstruction process.
After the "clean–up" of the recordings, we proceeded with the reconstruction of the source–space density current vectors $\mathbf{J}^p$, as discussed in Chapter 3. Each current vector $\mathbf{J}_i^p$ is estimated with regard to a cubic brain volume element (voxel) of 4 mm of side. Partitioning the whole brain volume with respect to this voxel size leads to an overall number of elements of order 10^4 voxels. Because there are just 248 MEG recording (one for each sensor) to reconstruct 10^4 current elements, the information given by the $\mathbf{J}^p$ is unavoidably redundant. Nevertheless, this method is performed in order to produce a MEG map that is comparable with those generated by other imaging techniques.
We then selected the same set of 12 brain voxels as described in the work by de Pasquale et al [17], whose coordinates are reported in Table 4.1. In contrast with their approach, we decided not to give any priority to any specific subset of those voxels [17]: we considered all the nodes as having the same weight.
By following a signal pre–processing method similar to that performed by Ref. [17], for each node we estimate the power time series $p_n[i]$ by using a moving average:

Node label	x(mm)	y(mm)	z(mm)
1	-43.0	-76.0	35.0
2	51.0	-64.0	32.0
3	-3.0	-54.0	31.0
4	-2.0	50.5	1.7
5	-13.1	51.5	23.4
6	-22.2	19.3	51.1
7	2.0	52.6	23.5
8	-23.2	-23.0	-18.0
9	-56.6	-25.1	-16.9
10	-2.0	-55.2	10.1
11	30.3	-12.8	52.6
12	9.0	42.0	53.0

TABLE 4.1: Brain coordinates [17] of the 12 nodes considered in this work. Coordinates are given according to the MNI152 coordinate system [48].

$$p_n[i] = \frac{1}{2a+1} \sum_{\ell=ib-a}^{ib+a} |\mathbf{J}_n^p[\ell]|^2 \,, \tag{4.1}$$

where $2a+1$ is the averaging box and $a = b = 40$. The moving average produces a downsampling of the original time series, leading to a sampling rate of $f_p = f_s/b = 50.8625$ Hz, which corresponds to a sampling period of $1/f_p \sim 20$ ms. Because ib is the averaging window center and there are 40 points laying on both its sides, the actual averaging window spans about 40 ms and shares half of its points with the previous and the following windows. Finally, we removed from each time series the initial 4 s to avoid transient effects, thus obtaining a resulting power time series of 18225 points (358.3 s). An example of a power time series is shown in Fig. 4.1.

4.2 Correlation Analysis

To describe our method, let us consider two power sequences corresponding to two generic nodes m and n. Rather than estimating the correlation across the whole time series, windows of different width are considered. We define as a window the set of points as:

$$F_w[k] = \{i | k_0 + 24k - 12w < i \leqslant k_0 + 24k + 12w\} \,, \tag{4.2}$$

where $k_0 = 1440$ is an offset on the window center position ensuring that also the largest possible window is completely inside the time series. The parameter w defines the window width, whereas k corresponds to the window center. The two parameters take on the values $w = \{1, \ldots, 120\}$ and $k = \{0, \ldots, 639\}$. Windows with the same k share the same center, regardless of the their width. The minimum window width is $N = 24$, which is equivalent to ~ 0.47 s. It follows that the range of possible window width is from 0.47 s to 57 s. The time corresponding to the window center is calculated as $(1440 + 24k) \cdot 0.02$ s (or, more simply, $(60 + k) \cdot 0.47$ s).
The general correlation term, $C_{n,m}(\tau, w)[k]$, is then defined as:

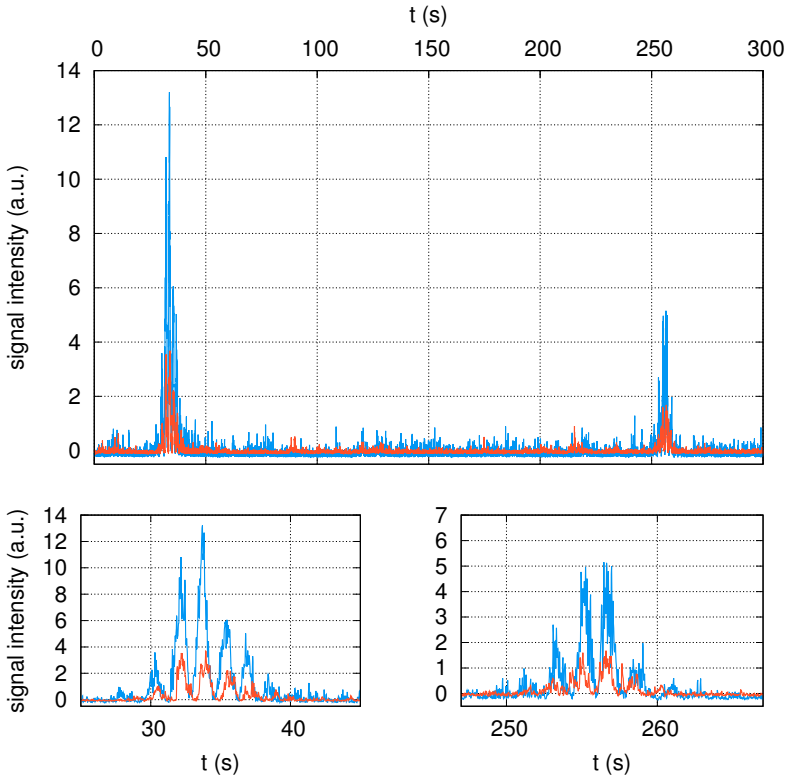

FIGURE 4.1: Two power time series corresponding to the nodes 1 and 2. In the bottom plots, the correlation events visible in the above graph are magnified, showing an oscillatory, burst–like behavior.

$$C_{n,m}(\tau, w)[k] = \sum_{\forall i \in F_w[k]} \delta p_n[i] \cdot \delta p_m[i+\tau]\,, \tag{4.3}$$

where

$$\delta p_n[i] = p_n[i] - \langle p_n[i] \rangle\ ,$$
$$\delta p_m[i] = p_m[i] - \langle p_m[i] \rangle\ ,$$

and τ is the time delay between the windows used in correlation estimation, as explained in Section 2.2.1.
The angular brackets in the previous equations represents the sample mean of the $24 \cdot w$ elements inside the window.
As discussed in Chapter 2, the Pearson correlation coefficient is defined as:

$$r_{n,m}(\tau, w)[k] = \frac{C_{n,m}(\tau, w)[k]}{\sqrt{C_{n,n}(0, w)[k] \cdot C_{m,m}(0, w)[k+\tau]}}\,. \tag{4.4}$$

In our work, only **zero–delay cross–correlation** is used in order to highlight the simultaneous communication between brain regions. This choice is justified because the communication direction is not known. However, attention has to be paid to the use of this approach due to the possible presence of spurious correlations as a consequence of source–leakage effects (see Paragraph 3.4.1). To overcome the problem, instead of solving Eq. 4.4 for $\tau = 0$, we evaluated the correlation value $r_{n,m}$ as the mean value between the Pearson coefficients obtained for $\tau = \pm 1$:

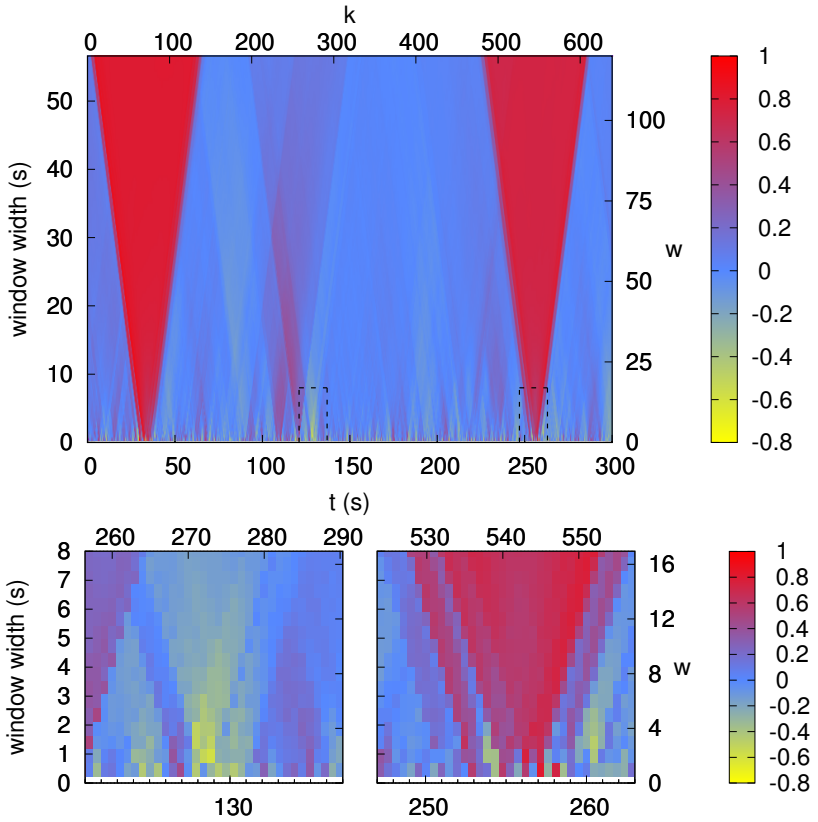

FIGURE 4.2: (above) Correlation coefficient diagram estimated from the two time series in Fig. 4.1. The $r_{n,m}$ values are in function of the correlation window center position k (x axis) and window width w (y axis). (below) Two magnifications of the above diagram (pointed out by dashed squares). Correlation coefficient values are mainly positive, with few exceptions (an example is shown in the bottom left square, that magnifies the time series epoch around $\sim$ 130s). In the bottom right square, a magnification of the lower part of a *funnel*–like structure (see Paragraphs 4.2.1 and 4.2.1) is displayed. It corresponds to the correlation event occurring in the time interval $250 - 260$ s, as shown in Fig. 4.1. For $w < 1 - 2$ s, some negative correlations (due to noise fluctuations) are present but they completely disappear for wider window widths that, conversely, highlight the strong correlation between the two segments of the time series.

$$r_{n,m}(w)[k] = \frac{r_{n,m}(-1,w)[k] + r_{n,m}(1,w)[k]}{2}. \tag{4.5}$$

In other words, Pearson correlation coefficient is taken as the mean of the Pearson correlation coefficients estimated on two windows shifted with respect to each other by 20 ms. An equal weight is assigned on the two components because, as already stated above, the communication direction between the brain volumes is supposed to be unknown. A 20 ms time interval is sufficient to suppress spurious correlations arising from source leakage, because their typical time scale is $\sim$1 ms: such interval does not interfere or spoil the analysis of the network dynamics, which is supposed to occur on time scales 2 orders of magnitude longer. Further elements that justify this choice are discussed in Paragraph 4.3.
In Figure 4.2 an example of a correlation diagram is shown.

Two main causes of correlations can be identified:

- noise fluctuations: in this case the correlation is "phony" and it exists only at small window width. Since the neighboring windows do not *confirm* the presence of a significant correlation, widening the window size causes the correlation to vanish.
- real correlations: in this case a real correlation event occurs, which develops over a time interval ξ and is characterized by the corresponding frequency $1/2\pi\xi$. To identify the correlation, the window width w must be at least $\sim \xi$ and the sampling rate of the signal has to be $< \xi/2$. By widening w, the correlation remains visible until w is so large that the correlation energy become negligible as compared to noise.

It is worth noticing that "true" correlation events can be mistaken for noise only if their signal–to–noise ratio is very low (comparable to the noise) and there are few occurrences. Let us assume that a real correlation between a pair of nodes exists but it consists of events with a very small duration in time. By enlarging w, the contribution of a correlation event remains significant until it is washed out by the noise, as it will be further explained in Paragraph 4.2.1. Moreover, if the events are not too far apart, enlarging the window the correlation will not decrease, since it will be "confirmed" by the next event. Thus, the correlation is visible even for larger windows. However, as it will be explained in Paragraph 4.2.3, the amount of such kind of events should be present in at least the 50% of correlation windows to define the existence of a link between the two nodes. The method proposed in this thesis prevents from identifying isolated couplings as significant and stable links.

4.2.1 Dependence of correlation coefficient from the window width

The dependence between the correlation coefficient and the window width can be explained as follows. Let us consider two independently and identically distributed (i.i.d.) time series $p[i]$ and $q[i]$ sharing a common peak–like signal at $i = i_0$. The two series can be described by the following equations:

$$\begin{aligned} p[i] &= \sqrt{S}\delta[i - i_0] + u[i]\,, \\ q[i] &= \sqrt{S}\delta[i - i_0] + v[i]\,, \end{aligned}$$

where $\sqrt{S}$ is the peak intensity, $\delta[i - i_0]$ is the Dirac–delta–like sequence, equal to 1 for $i = i_0$ and 0 otherwise. The series $u[i]$ and $v[i]$ are random noise sources with vanishing mean and variance equal to $\mathcal{N}$. In Figure 4.3 an example of $p[i]$ and $q[i]$ and their relative correlation diagram is shown.
Recalling Eq. 4.3, it is possible to estimate the correlation terms C_{pq}, C_{pp} and C_{qq}. Starting with C_{pq}, we have:

$$\begin{aligned} C_{pq}(0, w)[k] &= \sum_{\forall i \in F_w[k]} \left(p[i] - \langle p[i] \rangle\right)\left(q[i] - \langle q[i] \rangle\right) = \\ &= \sum_i \left[\left(\sqrt{S}\delta[i - i_0] + u[i]\right) - \left\langle \sqrt{S}\delta[i - i_0] + u[i] \right\rangle\right] \times \\ &\qquad \times \left[\left(\sqrt{S}\delta[i - i_0] + v[i]\right) - \left\langle \sqrt{S}\delta[i - i_0] + v[i] \right\rangle\right] . \end{aligned} \tag{4.6}$$

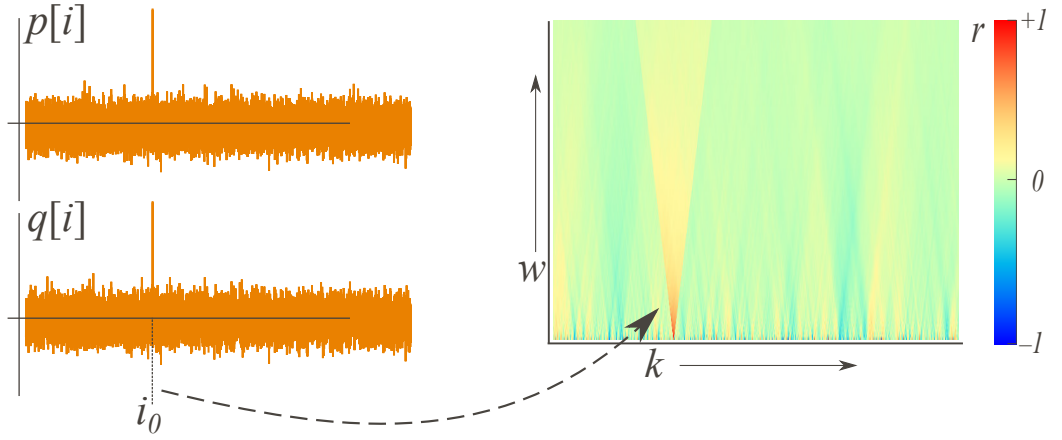

FIGURE 4.3: (Left) Examples of i.i.d. time series $p[i]$ and $q[i]$, sharing a common peak–like signal at $i = i_0$. (Right) The correlation diagram estimated on the two time series. The funnel–like structure (pointed–out by the arrow) corresponding to the correlation event is clearly visible in the diagram.

By knowing that the sample mean of the random noise sources vanishes, it follows:

$$\left\langle \sqrt{S}\delta[i-i_0] + u[i] \right\rangle = \sqrt{S}/N\,,$$

and then,

$$C_{pq} = \sum_i \left[\sqrt{S}\left(\delta[i-i_0] - \frac{1}{N}\right) + u[i]\right]\left[\sqrt{S}\left(\delta[i-i_0] - \frac{1}{N}\right) + v[i]\right] =$$
$$\sum_i \left[S\delta[i-i_0] + \frac{S}{N^2} - 2\frac{S}{N}\delta[i-i_0]\right] + \sqrt{S}\sum_i \delta[i-i_0]\,(u[i]+v[i]) + \sum_i u[i]v[i]\,. \quad (4.7)$$

which leads to:

$$C_{pq} = S\left(1 - \frac{1}{N}\right) + \sqrt{S}\,(u[i_0] + v[i_0]) + \sum_i u[i]v[i]\,. \quad (4.8)$$

Assuming that the number N of points inside the window is large ($N \geqslant 24$), the $\frac{1}{N}$ ratio is negligible compared to 1. Moreover, if the signal to noise ratio is high enough we can neglect the terms $u[i]$ and $v[i]$ connected to the noise. Then, the correlation between the series $p[i]$ and $q[i]$ can be approximated to:

$$C_{pq} \approx S\,. \quad (4.9)$$

By using the same approach, we estimate the C_{pp} correlation term as follows:

$$\begin{aligned} C_{pp}(0,w)[k] &= \sum_{\forall i \in F_w[k]} \left[\sqrt{S}\delta[i-i_0] + u[i] - \frac{1}{N}\sqrt{S} - \langle u[i]\rangle\right]^2 \\ &= S\left(1 - \frac{1}{N}\right) + \sum_i u^2[i] + 2\sqrt{S}\,(u[i_0] - \langle u[i]\rangle)\,. \end{aligned} \quad (4.10)$$

Once again, since $\langle u[i]\rangle$,$\langle v[i]\rangle = 0$, we can rewrite the equation as:

$$C_{pp} = S\left(1 - \frac{1}{N}\right) + 2\sqrt{S}\left(u[i_0] - \langle u[i]\rangle\right) + N\left(\langle u^2[i]\rangle - \langle u[i]\rangle^2\right) \approx S + \mathcal{N}N\,, \quad (4.11)$$

where $(\langle u^2[i]\rangle - \langle u[i]\rangle^2)$ is equivalent to the time series variance $\mathcal{N}$, and $(u[i_0] - \langle u[i]\rangle)$ can be neglected.
The previous considerations are clearly valid for C_{qq} as well and thus we have:

$$C_{qq}(0, w)[k] \approx S + \mathcal{N}N\,. \quad (4.12)$$

Once obtained all correlation terms, the resulting correlation coefficient, according to Eq. 4.4, is:

$$r_{pq} \approx \frac{S/\mathcal{N}}{S/\mathcal{N} + N}\,. \quad (4.13)$$

Eq. 4.13 justifies the presence of the funnel–like structures in the correlation diagrams. Once the peak is inside the sliding window, its contribution to the correlation does not depend on N, provided that $S/\mathcal{N} \gg N$. When instead $S/\mathcal{N} \leqslant N$, the peak contribution progressively vanishes as $1/N$. The previous considerations are generally valid for every time–bounded signal that is described by a finite sum of δ–like contributions.

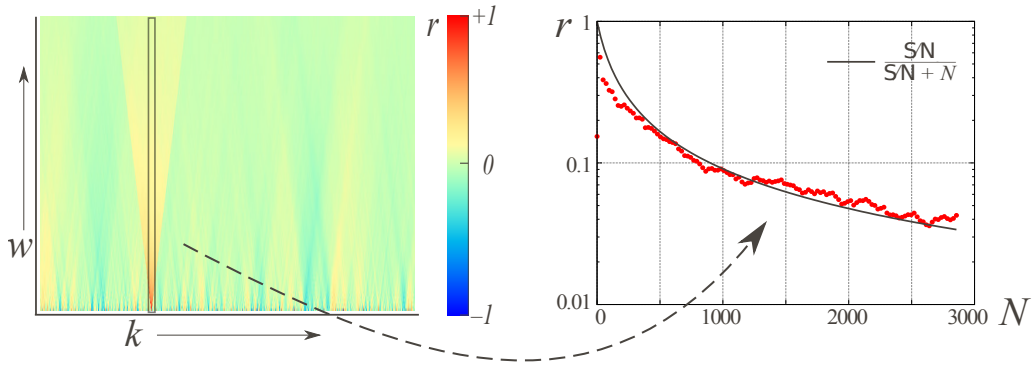

FIGURE 4.4: (Left) The correlation diagram estimated on the two time series $p[i]$ and $q[i]$. The funnel–like structure is highlighted by a black rectangle. (Right) Correlation coefficient r values against the number of points N in the correlation windows are shown (red dots). In the same graph, Eq.4.13 is plotted, showing the same trend as our example r values.

Another way to check the dependence of the correlation coefficient from the window width relies on a frequency domain approach. We again consider two real–valued time series $p[j]$, $q[j]$ with zero mean and unitary variance sampled with a sampling period T. The zero–delay cross correlation estimated on a window w of N elements indexed from 0 to $N-1$ is given by:

$$r = \sum_{j=0}^{N-1} p[j]q[j]\,. \tag{4.14}$$

By assuming $p[j]$ and $q[j]$ to be periodic with period NT, they can be expressed by means of their discrete Fourier transform (DFT) $P_k[j]$ and $Q_k[j]$ (see Chapter 2), we have:

$$P_k[j] = \sum_{j=0}^{N-1} p[j]e^{\frac{2\pi ijk}{N}}\,, \tag{4.15}$$

$$Q_k[j] = \sum_{j=0}^{N-1} q[j]e^{\frac{2\pi ijk}{N}}\,. \tag{4.16}$$

For the sake of simplicity, considering N as an even number, r can be expressed as:

$$r = \frac{1}{N}\sum_{k=-\frac{N}{2}}^{\frac{N}{2}-1} P_k[j]Q_k^*[j]\,, \tag{4.17}$$

where we used the standard DFT properties $Q_{N-k} = Q_{-k} = Q_k^*$, which is valid for every real–valued sequence.
In Eq. 4.17 the correlation coefficient is given by a comb of frequencies ranging from 0 to $1/2T$ (the Nyquist frequency) with a frequency resolution of $1/NT$ (see Figure 4.5). Since we are using standardized times series, it results that $P_0 \approx Q_0 \approx 0$, which means that the lowest frequency contribution is given by the $k = \pm 1$ elements corresponding to $1/NT$ frequency. This condition implies that only sequences evolving in a time scale between $2T$ and NT contribute to correlation and it justifies the need of a window width sufficiently large to enclose all the correlation event period.

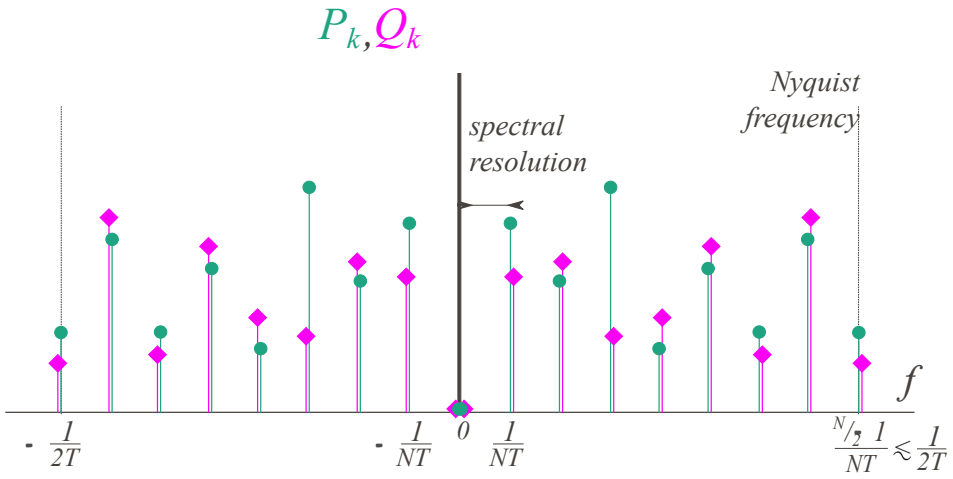

FIGURE 4.5: Representation of the Fourier transforms P_k, Q_k. The frequencies involved in the estimation of the correlation coefficient r span from 0 to the Niquist frequency $1/2N$, with a frequency resolution of $1/N$.

4.2.2 Correlation significance

Once we obtained correlation diagrams as in Fig. 4.2, it is then necessary to assess the reliability of each single correlation value estimated given a (k, w) pair. The significance evaluation of $r_{n,m}(w)[k]$ is performed by considering two different null hypothesis. The first one, $H_{0,G}$, assumes that the sequences producing $r_{n,m}$ are i.i.d. Gaussian random noise sources. The advantage of this assumption is that the p-value can be estimated analytically. Unfortunately, such hypothesis is realistic only considering very small windows. The second null hypothesis assumes that every pair of sequences is generated by two independent noise sources with the same distribution of amplitudes and approximately the same power spectrum (see Section 2.3.3). The last null hypothesis is far more realistic then the first one, but much more computationally demanding.
It is worth clarifying that the goal of both hypotheses is not to to verify whether some windows result to be significantly correlated with respect to a given significance level α but if the correlation is significant in each single window.
Detailed calculations on significance estimations are reported in the following section.

P–value estimation

Gaussian p–value To estimate the Gaussian p–value, we start by stretching the correlation coefficient r via Fisher transformation (see Chapter 2), obtaining $r' = \operatorname{arctanh}(r)$. Then we normalize the result on a variance $1/(N-3)$, and consider the new random variable $z_0 = r'\sqrt{N-3}$ as normally distributed. N represents the number of elements in a $F_w[k]$ window.
An alternative approach in estimating Gaussian p–value consists of using the correlation coefficient distribution:

$$f(r) = \frac{(1-r^2)^{\frac{N-4}{2}}}{B\left(\frac{1}{2}, \frac{N-2}{2}\right)}, \tag{4.18}$$

where $B(x, y)$ is the Euler beta function (see Chapter 2). Such distribution has zero mean and a variance $\sigma^2 = \frac{1}{N-1}$. Since $N = 24\ w$ (with $w = \{1, ..., 120\}$), the distribution can be approximated to a normal one thanks to the central limit theorem (see Chapter 2). It follows that it is possible to estimate a p–value for the normally distributed variable $z_1 = r\sqrt{N-1}$.
Comparing the two variables z_0 and z_1, we have that $z_0 > z_1$ for $r \gtrsim \sqrt{\frac{3}{N}}$, which corresponds to p–values slightly less than 0.05. Since our significance threshold to determine correlation existence is $\alpha = 0.01$, we decide to rely on the most conservative choice and thus to use z_1.
The final correlation term $r_{n,m}(w)[k]$ is the result of the average of two correlation terms shifted from each other by 20 ms (see Eq. 4.5). The two r, estimated for $\tau \pm 1$, are normally distributed and mutually independent, and distributed according to $\sim \mathcal{N}(0, (N-1)^{-1})$.
It follows that the correlation term $r_{n,m}(w)[k]$ in Eq. 4.5 is distributed as $\sim \mathcal{N}(0, (N-1)/2)$ and the p–value can be finally estimated by:

$$p_G = 1 - \Phi\left(r\sqrt{2(N-1)}\right),$$

where Φ is the normal cumulative distribution.

P–value through surrogates Considering a pair of sequences, 1000 surrogate pairs are generated such that they have the same value distribution and a similar power spectrum [66, 67]. Given a surrogate pair, the algorithm estimates a correlation value $r_{n,m}$ as a function of (k, w) pair and computes the correlation diagrams. The p–value of the original time series pair is obtained by ranking the respective correlation term, for a certain (k, w) selection, with respect to the surrogate correlation terms estimated for the same (k, w) pair, and by normalizing the rank position by 1000.
It results that the $H_{0,s}$ hypothesis is actually more realistic than the Gaussian one because the surrogate p–values for all the (k, w) pairs are systematically greater than the ones evaluated with the Gaussian method.
Looking at the p–value diagrams (Fig. 4.6), it is clear that the number of windows with a significant correlation increases with the window dimension. As discussed in 4.2.1, this phenomenon is due to the fact that a correlation event is much more visible over longer time scales and can be therefore identified by wider temporal windows.
Another example of correlation analysis is shown in Figure 4.7. The two time series correspond to a stronger correlated pair of nodes than in the case shown in Figures 4.2 and 4.6. Such strong correlation is clearly visible from the correlation diagram that shows a greater amount of funnel structures than in the previous case. Moreover, the p–value diagram obtained by means of surrogates strongly confirms the significance of those correlations.

To sum up: thanks to the surrogates method, it is possible to generalize the null hypothesis to represent systems which are more realistic than simple Gaussian processes, as in the previous paragraph. Each surrogate is realized by assuming that it is produced by the same process of the original time series: this is provided by forcing the surrogates to have the same amplitude distribution and autocorrelation of the original time series. Thus, for each pair of original time series it is possible to realize an arbitrarily large amount of their surrogates . They will be independent from each other by construction (see Paragraph 2.3.3). This way, it is possible to estimate the distribution of the correlation coefficients for each pair of nodes and calculate the p–value of the original $r_{n,m}$ as previously explained. The significance of each correlation coefficient is calculated independently for each pair of nodes, without the need to estimate a null model.

4.2.3 Efficiency

Once the correlation diagrams and their corresponding p–value diagrams are obtained, in order to reconstruct a network it is necessary to find a way to determine the existence of a link between each couple of nodes (represented by their corresponding time series) and, if such link exists, at which window width w it emerges. To do this, we introduce the *efficiency* parameter $\eta(w, \alpha)$ that measures the efficiency of a given window width w to detect correlations over with a certain significance level α.
The efficiency parameter is estimated directly from the p–value diagram (see, for example, Fig. 4.7): given a certain window width w, the efficiency $\eta(w, \alpha)$ represents the percentage of windows in which the correlation between the two time series is significant (see Fig. 4.8).
Setting a threshold η_0, the first $w = W$ such that $\eta(W, \alpha) = \eta_0$ represents the minimum time scale with which a node pair can be considered to be correlated. It is also possible that a pair of nodes never reaches the threshold (see Fig. 4.8). In this

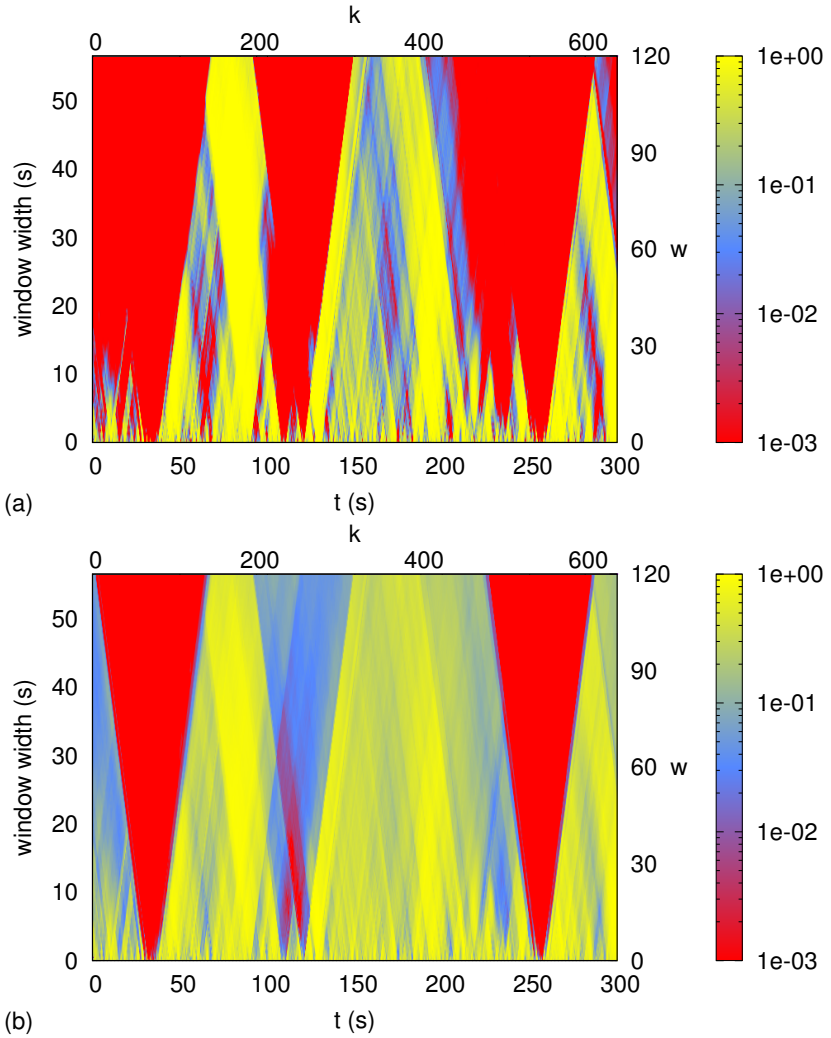

FIGURE 4.6: p–value diagrams related to correlation values in Fig. 4.2, evaluated by two different null hypothesis. In Fig. (A), p-values estimation is performed assuming i.i.d. Gaussian white noise sources according to Eq. 4.19 ($H_{0,g}$). In Fig. (B), the null–hypothesis used ($H_{0,S}$) assumes that the two time series are produced by two surrogate independent random noise sources having the same value distributions and power spectra of the original ones.

condition W cannot be defined and the link between the two nodes is deemed to be not existing.
For our purposes, we decided to set $\eta_0 = 0.5$: it means that, for a given W, a link between a pair of nodes is deemed to exist when the majority of the sliding windows shows a significant correlation, as expressed by α.
The shape of the efficiency function is strictly related to the structure and amount of the previously described *funnels* (see Par. 4.2.1), observed in the correlation diagrams. The η function condense information about the dynamics of the observed system, and, although an analytic description is still lacking, it is possible to make some general consideration.
Let us consider the case described in Paragraph 4.2.1: two i.i.d. time series sharing a single correlation event. Let w be the smaller window width that is large enough to contain the correlation event. In the corresponding p–value diagram, such window corresponds to a significant correlation value. For larger windows, the correlation

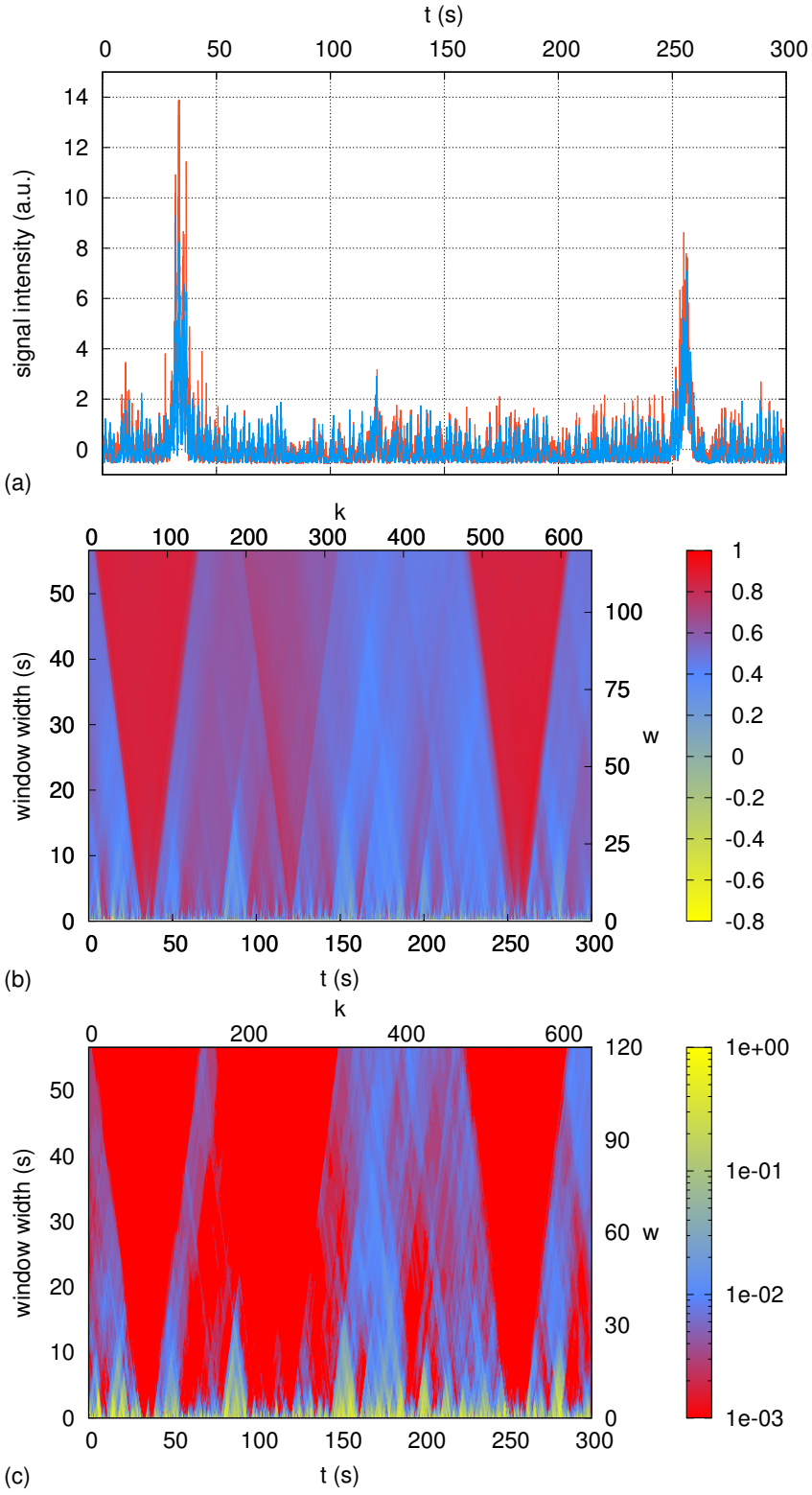

FIGURE 4.7: Correlation analysis of time series corresponding to (3,8) node pair. On the top, there are the two time series used, below their correlation diagram and at the bottom the corresponding p–values, estimated according to $H_{0,S}$

.

is still identified but progressively damped by the increasing energy contribution

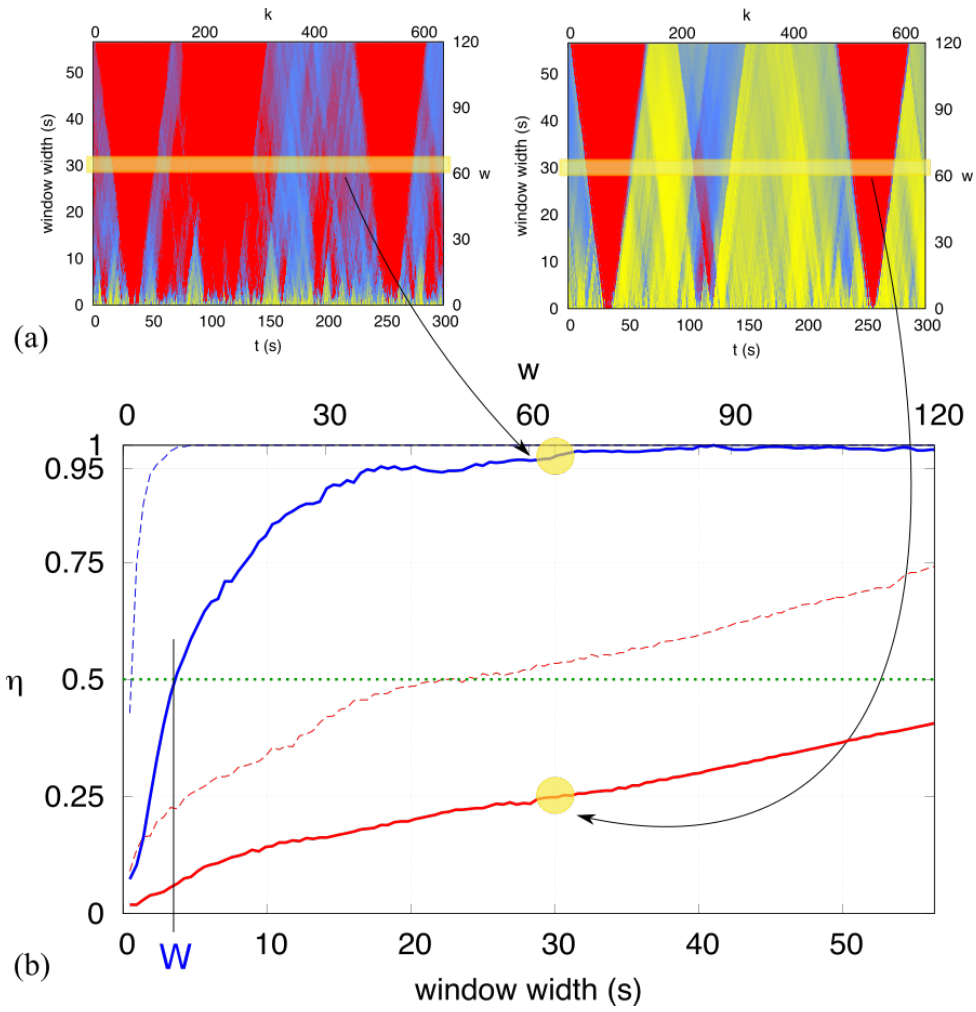

FIGURE 4.8: **a.** The p–value diagrams of the node pairs (1,2) and (3,8). In both diagrams, the p–values corresponding to the correlation windows of 30 s–width are highlighted in yellow. The efficiency value for a certain value of w and α is given by the fraction of windows in which the correlation is significant (i.e. the amount of windows with a corresponding p–value $< \alpha$). In Fig. b., the values of η corresponding to $w = 30$ for both pair of nodes are marked with a yellow circle. **b.** Efficiency trend in function of the window width w for two different couple of nodes ($(1,2)$ pair is marked in red, $(3,8)$ in blue). The dashed line identifies the efficiency values obtained following the null hypothesis $H_{0,G}$, the bold line the $H_{0,S}$ one. Depending on the η_0 selection, it is possible that some pairs never reaches the threshold, determining the absence of link between the two nodes whatever the temporal resolution used to observe the correlation. On the other hand, if the curve crosses the threshold at a certain W (highlighted in blue in the **b**), such W identifies the minimum window width at which a significant correlation (i.e. a link) exists. In Fig. b. the threshold $\eta_0 = 0.5$ used in this work is marked with a green, dashed line.

of the background noise. In such condition a decrease of the correlation coefficient as N^{-1} is expected. This effect is reflected by the behavior of the efficiency that, after reaching its maximum, is expected to progressively decrease. The effect is not evident neither in correlation diagrams nor in the efficiency trends shown in the previous figures, but it can be seen in the yellow and purple curves shown in Figure 4.9.

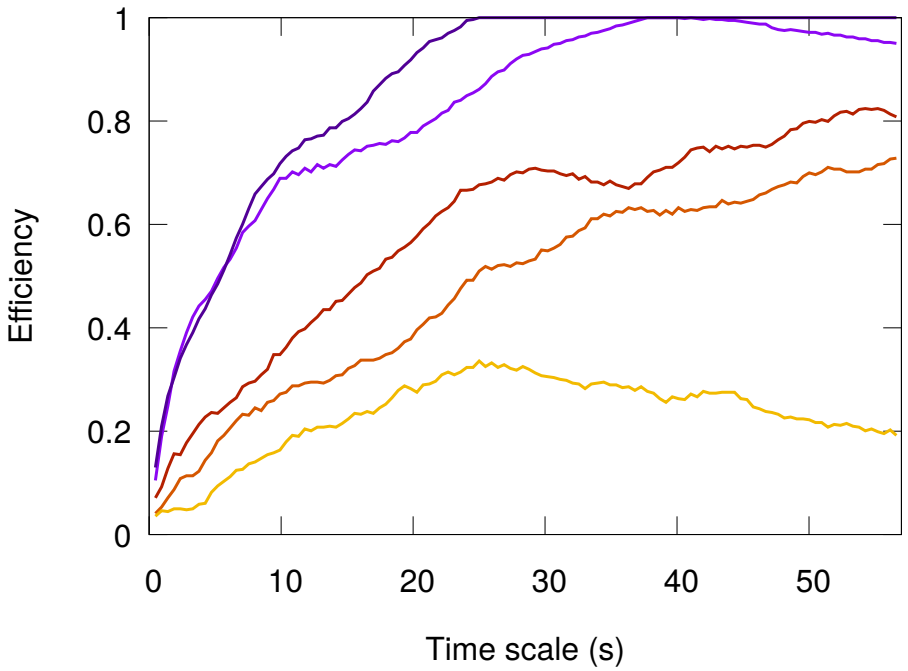

FIGURE 4.9: Examples of efficiency curves. The yellow curve describes the occurrence of few, weak and spurious correlation events: this is justified by its low value of efficiency even in its maximum point and by its decreasing immediately after such maximum. The other four curves identify stronger correlations, although their efficiency increases at different speeds. The slopes of the curves are strictly dependent on the amount of funnels present in the p–value diagrams, i.e. the amount of significant correlation events. The higher the number of funnels, the steeper the curve slope.

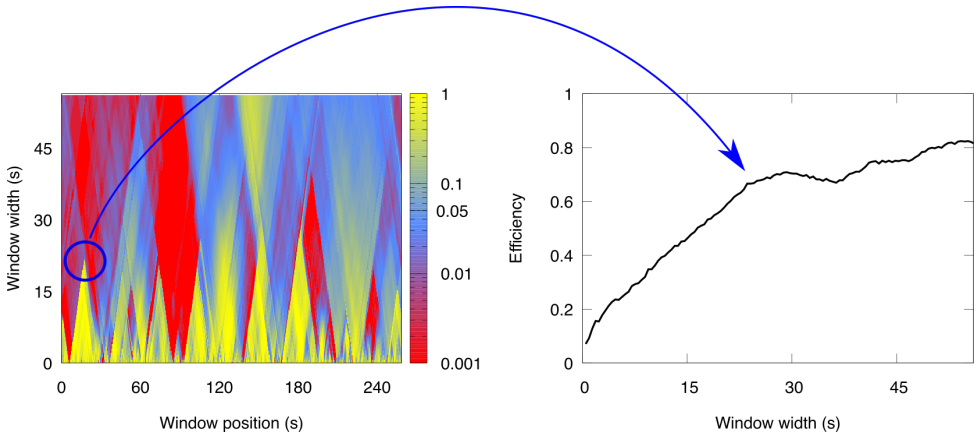

FIGURE 4.10: Diagram of p–values corresponding to the red curve in Figure 4.9. It provides an example of an efficiency curve whose slope changes due to overlapping funnels.

The lack of any decrease in Figure 4.9 in the other examples shown can be interpreted as follows. If the considered pair of time series has multiple correlation events, by increasing w there is a greater probability to include more than one event. This mechanism compensates the expected washing out of the correlation coefficient due to the contribution of the background noise. A decrease might be visible by using

larger w, then those used in this analysis because of the limited length of the recordings. Otherwise, the efficiency value keeps increasing or saturates at a certain value if events continue to happen.
Also the slope of η can change as a function of w, according to the amount of correlation events inside the window. As it is clearly visible in the examples shown in Figure 4.9 , the efficiency has seldom a linear trend with a constant value of angular coefficient. This configuration is possible only in case of few, separated correlation events, that, in the p–value diagram correspond to not–overlapping funnels (see the right p-value diagram in Figure 4.8). An approximately linear increasing is described by the orange curve in Figure 4.9, and by the red one in Figure 4.8.
The other three curves show a slope reduction: this happens when two or more p–value funnels start to overlap. An example of this behavior can be seen in Figure 4.7c or in Figure 4.10.
In this last case, it is possible to see few correlation events (red funnels) at small windows. In some cases, the correlation remains significant even for larger w (the red funnel "grows" towards the top of the diagram); otherwise the correlation events is washed out by the effects of the noise contribution or anti–correlated events (the funnel fades). For $w \sim 20$ an overlap of funnels is visible. An overlap happens when more than one correlation event is included in the same window: in this case, the amount of significantly correlated windows is not directly proportional to the number of funnels but it is reduced because the same significantly correlated window describes more than one event. This justifies the slope change of the η curve, highlighted in Figure 4.10.
Finally, the dark–blue curve shows another feature, that it can be seen also in the blue one in Figure 4.8. After the increasing phase, it reaches its maximum value and saturates, remaining approximately constant.
According to the results showed in this thesis, it is possible to hypothesize the efficiency behavior for an infinitely long time series spanning over an infinitely large window width interval. For $w \to \infty$, once the efficiency has reached its maximum value, η starts decreasing but with a speed that depends on the properties of the system. It could happen that the function reaches a *plateau* and remains stable within a certain interval of window widths: it means that the amount of windows in which the time series are significantly correlated remains almost constant.
It is possible to identify a range of window widths in which the correlation process can be considered as *stationary*. The identification of this range of stationarity is further confirmed when more recordings of the same system are available, as it will be explained in Section 5.1.
It is worth noticing that the method described in this thesis cannot be used to infer any information about the dynamics of a single time series, because it relies on the assessment of the "collective behavior" of at least a pair of acquisitions. For example, two identical non–stationary processes will always be correlated, so that their efficiency η is equal to 1 for every w and therefore stationary. On the other hand, two i.i.d. stochastic time series, stationary by definition, will never show a significant correlation.
A crucial parameter is the efficiency threshold η_0. According to the choice of η_0, it is possible to identify an interval of time scales within which $\eta \geqslant \eta_0$, i.e within which the link between the considered pair of nodes exists. Let W be the window width at which the efficiency curve overcomes the thresholds η_0. The interval is then given by $W \leqslant w \leqslant W_l$. The variable W_l is defined as the maximum window width at which the link efficiency is $\geqslant 0.5$.

It is worth noticing that in both case studies showed in this thesis work, W_{max} represents the maximum window width used in the analysis ($\sim$ 60 s for the brain networks – see Chapter 4 – and $\sim$ 40 days for the wind time series – see Chapter 6). This does not necessarily mean that, for even larger windows, η would become smaller than η_0; it is only the observational limit determined by the nature of the measurements. It is reasonable to hypothesize that, in different conditions and systems, $W_l < W_{max}$, where W_{max} identifies the largest observational window width or, conversely, that $W_l \to \infty$ for stationary correlated processes. Moreover, the amplitude of the interval $W \leqslant w \leqslant W_l$ is dependent on the selection of the threshold η_0, because it determines the value of W.
These considerations can be exploited in further analysis, for example by using the information provided to define the value of the efficiency threshold, or to classify the pair of nodes according to the presence or not of regions of stationarity, their duration or their asymptotic value.

4.2.4 An estimate of the efficiency curve fluctuations

The surrogates production described in Paragraph 2.3.3 is a stochastic procedure and consequently prone to statistical fluctuations. For each pair of nodes a p–value diagram is obtained by generating 1000 surrogates of the considered node pair. This means that there is not a unique realization of η for each pair of time series, but there can be variations according to the stochastic fluctuations of the generated set of surrogates. To estimate the amount of these fluctuations, 100 sets of 1000 surrogates each are generated for two sample pair of nodes, in order to have 100 possible realizations of the efficiency curve for each pair. In Figure 4.11 the results are shown.

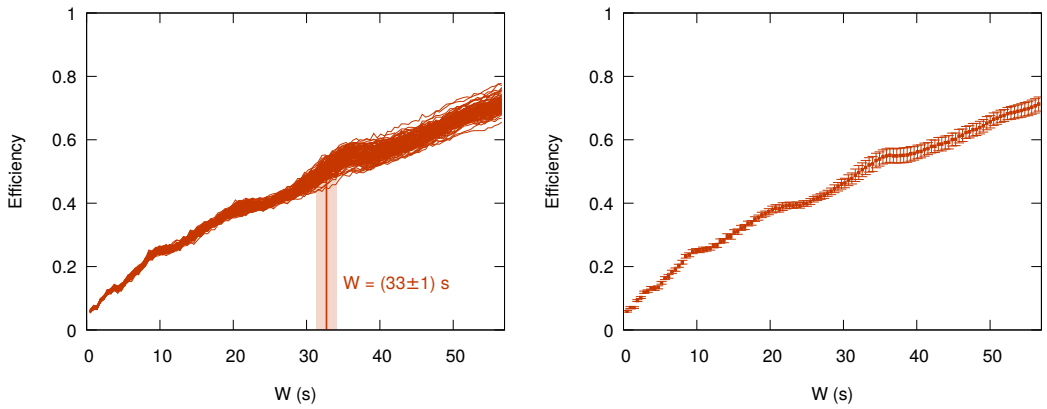

FIGURE 4.11: (Left) A set of 100 efficiency curves obtained for $\tau = 0$. The average $W(\eta_0, \tau = 0)$ and the corresponding standard deviation are reported. (Right) Average efficiency curve with the estimated error bars.

The same method is used to estimate the error bars of the W values in Figure 4.12.

4.3 Choice of the time lag τ to source–leakage removal

By exploiting the information provided by the efficiency function described in the previous paragraph, it is now possible to discuss an aspect which was only briefly commented on Section 4.2, i.e. the way the zero–lag correlation is handled in this analysis. As mentioned before, the correlation between each pair of time series is

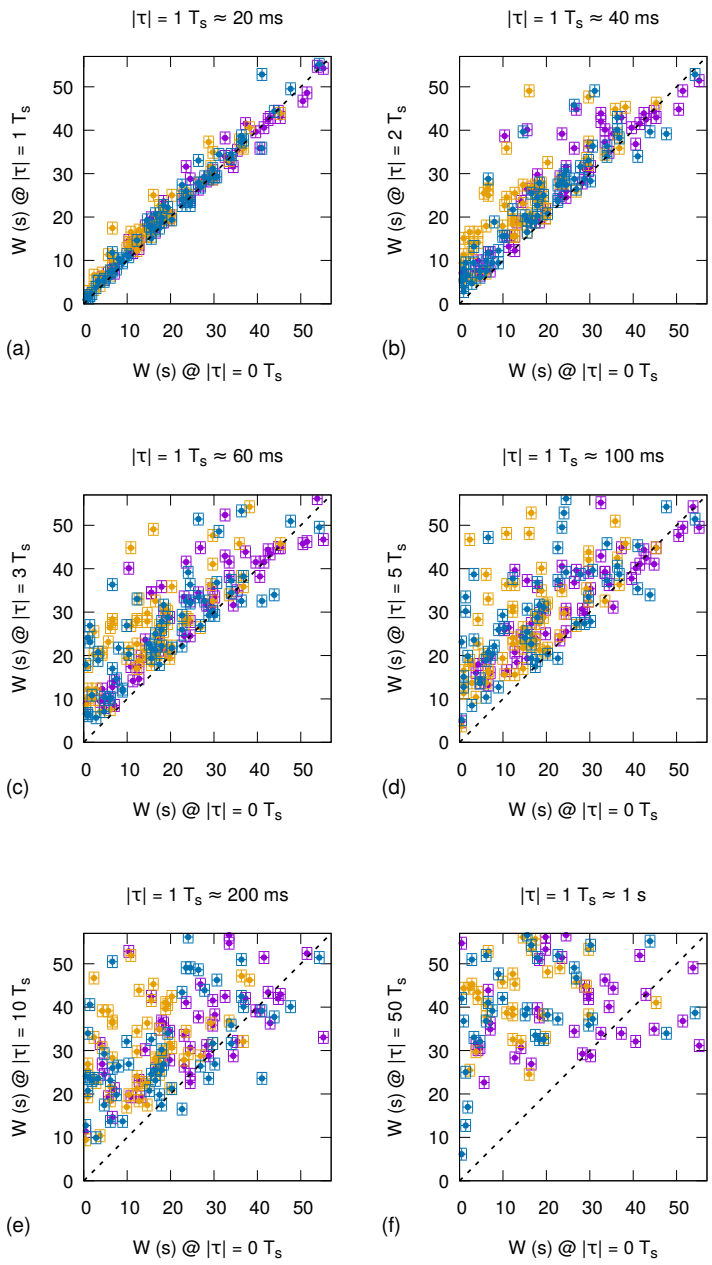

FIGURE 4.12: Comparison between the minimum correlation window $W(\eta = \eta_0)$ obtained with $\tau = 0$ and $\tau = \pm 1, \pm 2, \pm 3, \pm 5, \pm 10, \pm 50$ for every pair of nodes of the set in Table 4.1. The results reported refers to a single subject with three MEG recordings. The yellow, purple and blue colors of the points refers to the three different recording. For $\tau = 0$ and $\tau = \pm 1$ there are not significant difference in the values of W. Increasing the time lag, even the W become larger until it is impossible to observe a significant correlation for any of the investigated windows. For this reason the amount of points in the last two graphs is substantially decreased.

estimated at zero–lag, since the communication direction is not known. However, zero–lag correlations can be affected by spurious contributions, due to reconstruction errors that in the literature are known as source leakage (see Paragraph 3.4.1).

To remove this effect, the zero–lag correlation was estimated by averaging the correlation coefficients calculated with time lags $\tau = \pm 1$ *Ts*, where *Ts* is the sampling time of the time series approximately equal to 20 ms. Since the lag ($\sim$ 20 ms) is short compared to brain dynamics and to the autocorrelation time of each singe node, it turns out to be sufficient to remove instantaneous and perfectly synchronous events without destroying real correlation events, which span much wider temporal intervals ($\sim$ 10 s, see for example Figure 4.1).
To prove these arguments, a correlation analysis at different time lags was performed. We tested values of τ, expressed in *Ts*, equals to $0, \pm 1, \pm 2, \pm 3, \pm 5, \pm 10, \pm 50$. In Figure 4.12 the results for a single subject and three MEG recordings are shown.
To compare the different choices of τ, the efficiency curves for each pair of node, recording and τ choice were calculated. In this way, it was possible to obtain all W values such that $\eta = \eta_0 = 0.5$, i.e. the smallest window widths at which the pair of time series are deemed to be significantly correlated and a corresponding link to exist, (see Paragraph 4.2.3). In Figure 4.12, the coordinates of each point represents the W value characteristic of a node pair obtained for $\tau = 0$ (x axis) and that obtained for the same node pair by using the other values of time lag (y axis). If the two configurations are not significantly different, $W(\tau = 0) \sim W(\tau \neq 0)$, the points are expected to lay on the diagonal dashed line drawn in the plot. This is what happens in the first graph in Figure 4.12: with the exception of few outliers, the majority of points has approximately the same value of abscissa and ordinate, confirming the lack of a significant difference between the results obtained with $\tau = 0$ and $\tau \pm 1$. On average, the difference between the points and the $y = x$ line is 1.5 ± 0.2, (0.2 being the standard error). It follows that there is a risk of overestimating the value of $W(\eta_0)$ of 2 s at most, which does not affect significantly the result. The result also confirms that no real correlation event is destroyed by the averaging operation. However, for the same reasons, there is no evidence that the source leakage affects significantly the data.
On the other hand, the increase of τ produces a shift of all points in the upper–half of the plot: this highlights an average increase of the minimum window width necessary for identifying a significant correlation, independently from the recording or the pair of node considered. The effect is related to the autocorrelation of the signal: if the autocorrelation time is greater than the delay τ the cross–correlation coefficients are unaffected by time–shifts of the two time series by $\pm\tau$.
The contrary occurs if the delay τ overcomes the autocorrelation time.
In Figures 4.12 e–f, the effect is well visible: in many cases it is impossible to find out a value of W, i.e. no link exists. This is the reason of the significant decrease of the amount of points in the last two graphs. To sum up, the averaging operation is dangerous for any choice of $\tau \geqslant 2$, whereas it does not risk compromising the information about real correlations when $\tau \pm 1$.

4.3.1 Non–zero delay cross correlations

It is worth remarking that, in this work, the problem of non–zero–delay cross correlations was not addressed because of two main reasons. First, there were no information about the directionality of the communication between the nodes. Second, the application of the algorithm described in this thesis to investigate the optimal time lag would be computationally very demanding. A way to tackle with this problem would rely on the application of *a priori* knowledge about the system dynamics to pre–set a proper delay and then carry on with the analysis. This is, however, out of the scope of this thesis.

Chapter 5

Network Identification

The correlation method explained in Chapter 4 has a general applicability to every kind of dynamical systems. For this reason, in the first part of this Chapter I am going to describe the steps we use to reconstruct networks by assuming to handle with a generic system. Then, in the last paragraph, we will discuss the specific results obtained with our dataset of MEG recordings, described in Section 4.1, to identify fully–connected resting state brain networks.

5.1 Single system approach

Single recording Let us consider M nodes of a generic dynamical system, each node producing a time series. Following the steps described in the previous Chapter, correlation, p–value and efficiency diagrams for each node pair of the set are obtained. Thanks to the efficiency diagrams, we know the minimum time scale w at which each pair of nodes (j_1, j_2) overcomes the efficiency threshold η_0, i.e. we know the W_{j_1,j_2} value that corresponds to a link appearance.
It is, then, it is possible to build a $M \times M$ symmetric matrix $\hat{W}(\eta_0, \alpha)$ with $M(M-1)/2$ independent time scale values W_{j_1,j_2}. The diagonal matrix elements are equal to zero and if a link between a node pair does not exist, the corresponding element W is deemed to be missing. An example of a time scale matrix is shown in Figure 5.1.
Once the $\hat{W}$ matrix is obtained, it is possible to look for fully connected networks. There is not a one–to–one correspondence between each matrix $\hat{W}(\eta_0, \alpha)$ and the fully connected networks we can obtain, because this operation varies according to the time scale resolution W we want to observe. At this stage, we have to convert the time scale matrix into a binary one: once a certain W_0 of interest is fixed, all the values $W_{j_1,j_2} \leq W_0$ are mapped onto the value 1, while the elements $W_{j_1,j_2} > W_0$ are mapped onto the value 0. Therefore, all the links labeled with 1 represents the fully connected network configuration that it is possible to identify at the W_0 time scale of observation.

Multiple recordings Let us now assume to have multiple recordings of the same dynamical system and the same set of nodes, acquired in similar conditions. In this case, we want to find a way to merge all information in order to extrapolate the average behavior of the system in a certain condition.
To do this, we apply the same operations described above for a single recording to the whole set of m available time series recorded for each node. We then obtain m $M \times M$ time scale matrices $\hat{W}_m$, one for each recording (see Figure 5.3).
Before merging the information carried by the m matrices, it is worth noting that some W_{j_1,j_2} elements can be missing, a situation that occurs when the link between the (j_1, j_2) pair does not appear in the observed temporal range. Missing links are not

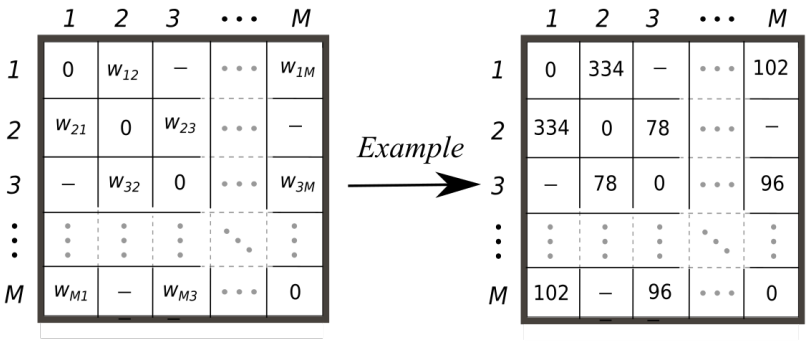

FIGURE 5.1: Example of time scale matrix $\hat{W}(\eta_0, \alpha)$. On the left, the matrix is reported in its generic form, whereas, on the right, an example with fictitious time scale values is shown. A time scale matrix is symmetric and its diagonal values are equal to zero (a node exhibits a link with itself at any time). Missing links between two nodes are identified by the "–" symbol.

uncommon. For example, in the case of MEG dataset (see Section 4.1), the percentage of unavailable network links for all the 15 $\hat{W}$ matrices of the sample varies between 5% and 79%, with an average of 33%. To guarantee the most conservative approach, given a pair of nodes if there is a single missing value, the link is considered as not existing for that pair of nodes.

It is then necessary to define the merging procedure. Having a number m of $\hat{W}$ matrices, there are m W_{j_1,j_2} values for each pair of nodes (j_1, j_2); a unique matrix of time scales describing the average behavior of the system dynamics is then desirable. Due to the scarcity of available recordings, the presence of missing values, and in general, the fact that we do not know the distribution of the correlation time scales, both the sample mean and the sample standard deviation of the W_{j_1,j_2} values, are not reliable statistics. Therefore, we decided to merge the information by using an order statistics, which, in addition, can be easily tuned to assess the confidence level. For every system, the m $\hat{W}$ matrices merge in:

$$W_{\text{merge};j_1,j_2}(\alpha, \eta_0, R_1) = R_1^{th}\text{largest}\left\{W_{i;j_1,j_2}(\alpha, \eta_0) | i = 1, \ldots, m\right\}, \tag{5.1}$$

where $R_1 = \{1, \ldots, m\}$ is the order parameter, that can range from the largest ($R_1 = 1$) to the smallest ($R_1 = m$) value of the window widths w that lead to a significant correlation in the pair (j_1, j_2). The choice of the R value corresponds to the level of conservativity required for the analysis. The most conservative approach is $R_1 = 1$ which ensures that all the nodes are correlated in each one of the m recordings. The higher the R_1 value, the more prone to outliers is the choice. As previously mentioned, in presence of missing values in at least one of the subject recordings, the link is considered as not existing.

There can be many effects justifying the lacking of links. At this stage of the analysis it is not possible to clearly discriminate between statistical and neurophysiological reasons, although a crucial contribution is surely given by the selection of parameters previously discussed. Since the main goal of this work was to test the capability of the method to produce robust results, we decided to be extremely conservative: for example, in many cases, a missing link between a pair of nodes is due to a single recording out of three that does not have a significant w. In these cases it is reasonable to think that a coupling exists, maybe for very large windows, but it is not

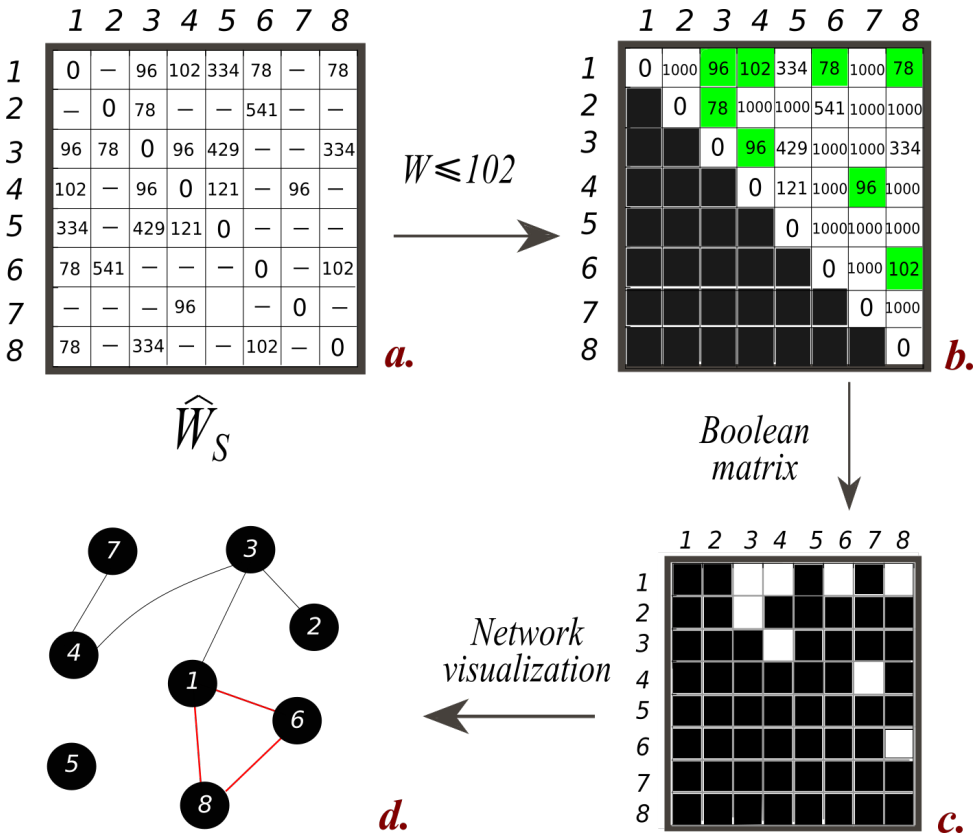

FIGURE 5.2: **From a time scale matrix to a network.** Once a matrix of time scales is estimated (***a.***), it is necessary to choose a window width of observation W_0 to identify fully–connected networks. Thus, all the links emerging at time scales $W \leq W_0$ are considered in the network structure. In our example, $W_0 = 102$. The resulting matrix is shown in ***b.***: all the values lower than W_0 are highlighted in green. Since it is symmetric, the relevant information is contained in half of the matrix. The null values on the diagonal are ignored, because self–links are not considered. Moreover, the "–" symbol, identifying missing links, is replaced by an arbitrary value (in our case, 1000), higher than the maximum window width used in the analysis: in our algorithm, it guarantees that such links cannot be observed at any time scale resolution. In ***c.***, the matrix is transformed to a boolean matrix. All "green values" are replaced by ones (white squares), whereas all others by zeros (black squares). In ***d.***, a graphical representation of the network structure identified by the binary matrix is shown. An example of fully–connected network is emphasized by red–colored links.

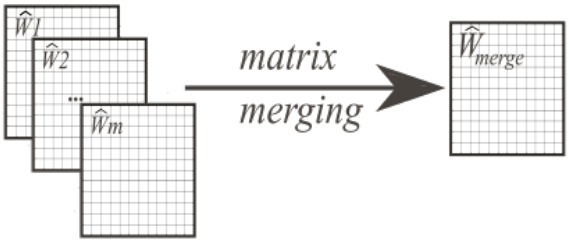

FIGURE 5.3: Merging of time scale matrices $\hat{W}$ obtained by multiple recordings of the same system.

enough robust to fulfill the significance requirements in every acquisition. Nevertheless, since it is not possible to find a shared W such that the correlation exists in every recording the link is marked as missing. This problem could be partially overcome if one has a great amount of MEG recordings of the same subject, allowing to reconstruct a distribution of the W values. In this condition, instead of using the maximum W one could use a lower ranking order statistics.
The versatility of the method allows to investigate different expressions of the neural dynamics by tuning the parameter values: the particular conservative configuration proposed in this thesis permits to investigate strong and stable correlations between a pair of time series. The conservativeness is a consequence of the choice of the efficiency threshold η_0, that requires that the majority of the correlation windows corresponds to a significant p–value in order to identify the existence of a link. This also explains why some links result to be missing.

To sum up: the system has an associated matrix, whose elements are the largest of the minimum window widths for which the links between each pair of nodes – if any – start to appear. The choice of the largest W value for each pair of nodes j_1, j_2 ensures that the observed links are always present by using window widths $W_{\text{merge};j_1,j_2} \leq w \leq W_l$. The variable W_l is defined as the maximum window width at which the link efficiency is still $\geqslant 0.5$, as discussed in Paragraph 4.2.3. The definition of $W_{\text{merge};j_1,j_2}$ by means of multiple recordings, acquired in separated times, ensures that the intervals of w values in which the links exist are a general and descriptive feature of the system, not dependent on the particular conditions or times of the acquisition.

5.2 Network robustness

Up to now, we defined a method to identify the presence of a fully connected network by using single and multiple recordings of a node set belonging to a generic dynamical system. The network structures assessed by means of this method depend on the selection of three parameters: the significance threshold α, the efficiency threshold η_0 and the order parameter R_1. Their values can be tuned according to the level of conservativity we want to apply to the analysis and the characteristic of the examined network.
To impose higher conservativity, parameters α and η_0 have to be large and R_1 small. In this condition, a smaller amount of links are present than in the case of a more liberal choice of parameters. In the case of our MEG recordings, we decided to follow the most conservative approach by setting $R_1 = 1$. By analyzing a set of multiple

recordings of the same system, it is possible to obtain different values of W in which a link between the same pair of nodes is observed. Although these values are in general similar, by choosing the largest value of W we guarantee that the link is observed in all the available recordings. Using this approach, there is a lower probability that the links obtained are the results of phony correlations, thus providing a robust and reliable network structure.

5.3 Multiple systems

So far, we dealt with a single dynamical system with one or multiple recordings of its nodes. For each system, we have a $\hat{W}_{merge}$ matrix of time scales describing the average behavior of the system. In case there is only one recording, $\hat{W}_{merge}$ coincides with $\hat{W}$. For the sake of simplicity, we will refer to such matrix as $\hat{W}_S$, where S identifies the system.
It is often possible to have many systems of the same nature (e.g.,different human subjects), in which we observe the dynamics of the same set of elements. Assuming that systems with a similar nature have a similar behavior, one can apply the same approach used above to merge matrices $\hat{W}_S$ of different systems and identify an "average" subject or system. Please refer to Figure 5.4 for a graphical representation.

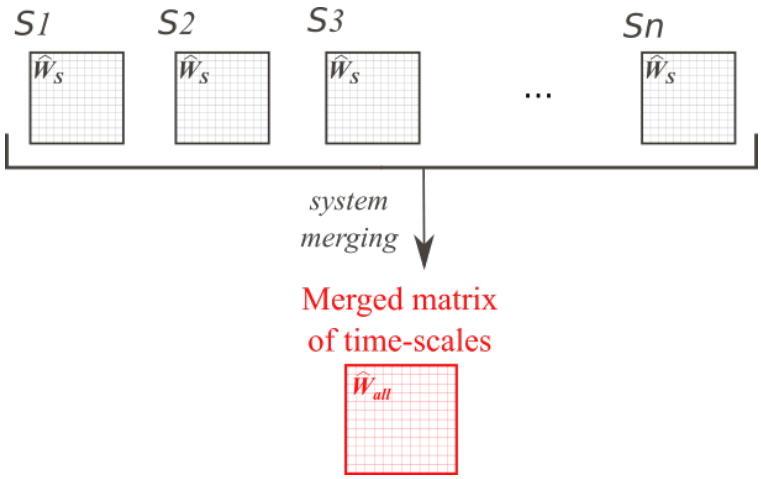

FIGURE 5.4: Merging of time scale matrices $\hat{W}_S$ obtained by multiple systems of the same nature.

To do this, for the same reasons as in the previous case, we rely once again on order statistics:

$$W_{\text{all};j_1,j_2}(\alpha,\eta_0,R_1,R_2) = R_2^{th}\text{largest}\left\{W_{S,i;j_1,j_2}(\alpha,\eta_0,R_1)|i=1,\ldots,n\right\}. \tag{5.2}$$

In this case, R_2 ranges from 1 to n, where n is the number of systems.
Similarly as in the single system case, $\hat{W}_{all}$ is useful to check the existence of fully connected networks as a function of a certain W_0, and to verify which are the significantly connected nodes. In other words, this means to check if $W_{\text{all};j_1,j_2} < W_0$ holds for every (j_1, j_2) pair. As in the previous case, the network structure changes according to the choice of W_0. To obtain the network configuration corresponding to a certain selection of W_0, $\hat{W}_{all}$ is converted to a boolean matrix, where the links emerging at time scales greater than W_0 are labeled with 1, and 0 otherwise.

Assuming that S is a set of nodes, a fully–connected network C exists if and only if:

$$W_{all;j_1,j_2}(\alpha, \eta_0, R_1, R_2) \leq w_0, \quad \forall j_1, j_2 \in C\,. \tag{5.3}$$

Moreover, we assume that C is the largest fully connected network that is possible to obtain with the given set of nodes. To avoid defining as a network a simple link between two nodes, the minimum number of nodes to make up a network is set to 3. Starting from the same set of nodes, the resulting fully–connected network configuration changes according to the choice of parameters.

5.4 Network robustness in multiple systems merging

The network configuration depends again on the α, η_0, R_1 parameter selection, and in addition on the R_2 choice. Lower values of α, R_1 and R_2 and higher η_0 value correspond to more conservative criteria. Again, it is reasonable to suggest that stricter criteria yield a decrease of the occurrence of phony correlations.The resulting network has to be robust against the choice of the parameters.
In the following, this point will be examined by means of the results obtained from the MEG dataset. To do this, the network configurations corresponding to three different set of parameter values are compared. According to the considerations discussed in Section 5.1, we set $R_1 = 1$ and $\eta_0 = 0.5$, whereas the significance level α and the order parameter R_2 assume different values (see Table 5.1). The largest networks obtained with a certain choice of parameters are listed in Table 5.1. If the first two columns are compared, it results that both the nodes involved in the networks and the time scales at which the links appear are very similar. Although this outcome can be partly justified by a compensation effect due to a less stringent level of significance and a more conservative condition on the order parameter ($R_2 = 2$), it also reflects an intrinsic robustness of the result. Looking at the third column, corresponding to an even more conservative value of the order parameter ($R_2 = 1$), it can be seen that the networks are fewer than in the previous cases and appear at longer time scales, but the configurations of the networks are consistent in most of the results. The correlation between 4 nodes (1, 5, 8 and 9) seems to be stable, because it emerges in most of the networks observed, regardless the selection of parameters used.

$\alpha = 0.01$ $R_2 = 3$		$\alpha = 0.05$ $R_2 = 2$		$\alpha = 0.05$ $R_2 = 1$	
32 s:	(1,5,8,9)	26 s:	(1,5,8,9)	45 s:	(3,5,9,11)
32 s:	(1,8,9,11)	26 s:	(1,5,9,11)	47 s:	(1,6,8,9)
32 s:	(5,8,9,10)	28 s:	(1,3,5,9,11)	47 s:	(5,6,8,9)
35 s:	(5,6,8,10)	33 s:	(5,6,8,10)		
		33 s:	(1,5,8,9,10)		

TABLE 5.1: Comparison between 4–nodes networks observed for 3 different configuration of parameters. In the examples proposed, the efficiency threshold η_0 and the first rank order parameter R_1 are kept constant to the values 0.5 and 1 respectively. The first configuration (left column) is that used to obtain the results discussed in the main text.

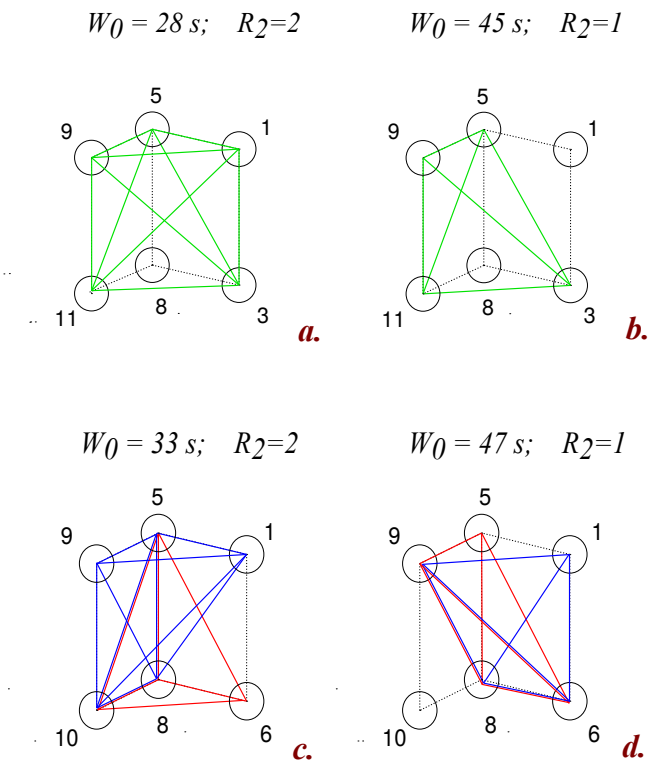

FIGURE 5.5: Graphical representations of some network structures in Table 5.1. In ***a.*** and ***b.*** panels are shown the largest network configurations for $R_2 = 2$ and $R_2 = 1$ at $W_0 = 28$ s and $W_0 = 45$ s respectively. For both configurations, $\alpha = 0.05$, η_0 and $R_1 = 1$. It is clearly visible that the two networks share almost the same set of nodes although the parameter R_2 has different values. The only difference by using a stricter order parameter (R_2=1) is the loss of 3 node, probably the weakest correlated one in the fully–connected network obtained with $R_1 = 2$. In ***c.*** and ***d.*** panels, other two network configurations of Table 5.1 are shown. The parameters α, η_0, R_1 and R_2 are the same as in the previous case, whereas other two window widths are observed (33 s and 47 s respectively). Two large fully–connected networks for each window width emerge: in both cases, each pair of networks are very similar, sharing three (5, 8 and 10) out of five nodes in the $R_2 = 2$ case and three (6, 8 and 9) out of four nodes in the $R_2 = 1$ case. Thus, for the sake of simplicity, it is reasonable to considered the two networks in ***c.*** as a single (although not fully-connected) network and to do the same for those in ***b.***. It results that the network structures in $R_2 = 2$ and $R_2 = 1$ are not so different, sharing five out six nodes involved. This fact confirms the general robustness of the network structure against the choice of parameters.

5.5 Discussion

As mentioned in Chapter 4, the work that makes up the core of this thesis was inspired by de Pasquale *et al*. [17].
The method estimates the optimal correlation window that maximizes the measure of interdependence between the nodes of the DMN, highlighting a non–stationary behavior of the connectivity between the nodes of the network. The temporal windows the authors identify to observe the switching on and off of the correlations is of order ~ 10 s.

Our method is conceptually the opposite and aims at identifying – by changing the temporal resolution – the time windows at which the correlation is stable and how many and which nodes such correlation involves.
In Figure 5.6 the fully connected networks identified from the initial set of 12 nodes in Table 4.1 at different window widths w are shown. The circles represent the nodes, connected among each others by different color segments that identify the different networks they belongs to. By enlarging w, the network can either remain unchanged or include other nodes. Moreover, two or more networks can merge together producing a *network coalescence*. Looking at Figure 5.6, the largest network emerges at relatively small $w \sim 25 - 35$ s.
The result is of the same order of magnitude as in Ref. [17] as well as in other results in the literature. For example, Hindriks et al. [36] find out an optimal window of about 50 s to observe functional connectivity modification by using MEG recordings, whereas Fransson [23] investigates spontaneous low–frequency BOLD signal fluctuations, limiting them in the frequency interval between 0.012 and 0.1 Hz (corresponding to temporal widths ranging from $\sim 10 - 80$ s).
Looking at the results shown in Figure 5.6 it emerges that the identified networks do not exactly correspond to the structure of the default mode network described by fMRI. The first fully–connected network emerging at 25 s includes three nodes, $\{1, 8, 11\}$, corresponding to the angular gyrus, the hippocampus and the frontal eye field. The last one is considered in the literature as being external to DMN, despite it appears here as to be one of the "most connected" nodes ($w \geqslant 25$ s). On the other hand, at this time resolution, the angular gyrus (AG) seems to be strongly involved in the communication between the various regions, since it is included in all the three fully connected networks emerging at 28 s, namely $\{1, 5, 8\}$, $\{1, 8, 11\}$, $\{1, 9, 11\}$. The AG is one of the regions belonging to DMN and it is physically connected to the hippocampus by one of the major occipitotemporal association tracts. For $w \geq 28$, two other nodes result to be strongly correlated, namely 5 and 9, which represent the ventral medial prefrontal cortex (vMPFC) and the inferior temporal gyrus (ITG). Both belongs to DMN and vMPFC is even one of the most characteristic of the DMN regions.
For larger windows, other two nodes are added to the previously described networks: the superior frontal sulcus (SFS, node 6) and the retrosplenial (RS, node 10). At $w = 32$ s, a less–connected network emerges, involving the node 7 and 12, the right medial prefrontal cortex and the superior frontal gyrus. The last one is the second node considered as being external in the present analysis. For $w = 35$ s, four fully–connected networks are shown in Figure 5.6, linked to one another and having four nodes each: $\{1, 5, 8, 9\}$, $\{1, 8, 9, 11\}$, $\{5, 8, 9, 10\}$ and $\{5, 6, 8, 10\}$. The fifth network, which includes nodes $\{7, 9, 12\}$ is separated and connected to the other ones only through the node 9. These last configurations highlight the ubiquitous presence of the hippocampus in the four largest networks.
Another important aspect in terms of DMN observation is the absence of the node 3 from all the previously mentioned networks. This nodes identifies the posterior cingular cortex (PCC), probably the most representative neural area of DMN along with MPFC. In this respect, there are other noteworthy results, as the absence of node 4, which belongs to the left dorsal MPFC, and the poor correlation of its right counterpart (node 7) with the other, larger networks.
From these results, it is not possible to identify a network having the same DMN configuration described in the literature, in particular with the network structure emerging from fMRI observations. However, this fact can be justified by several reasons.

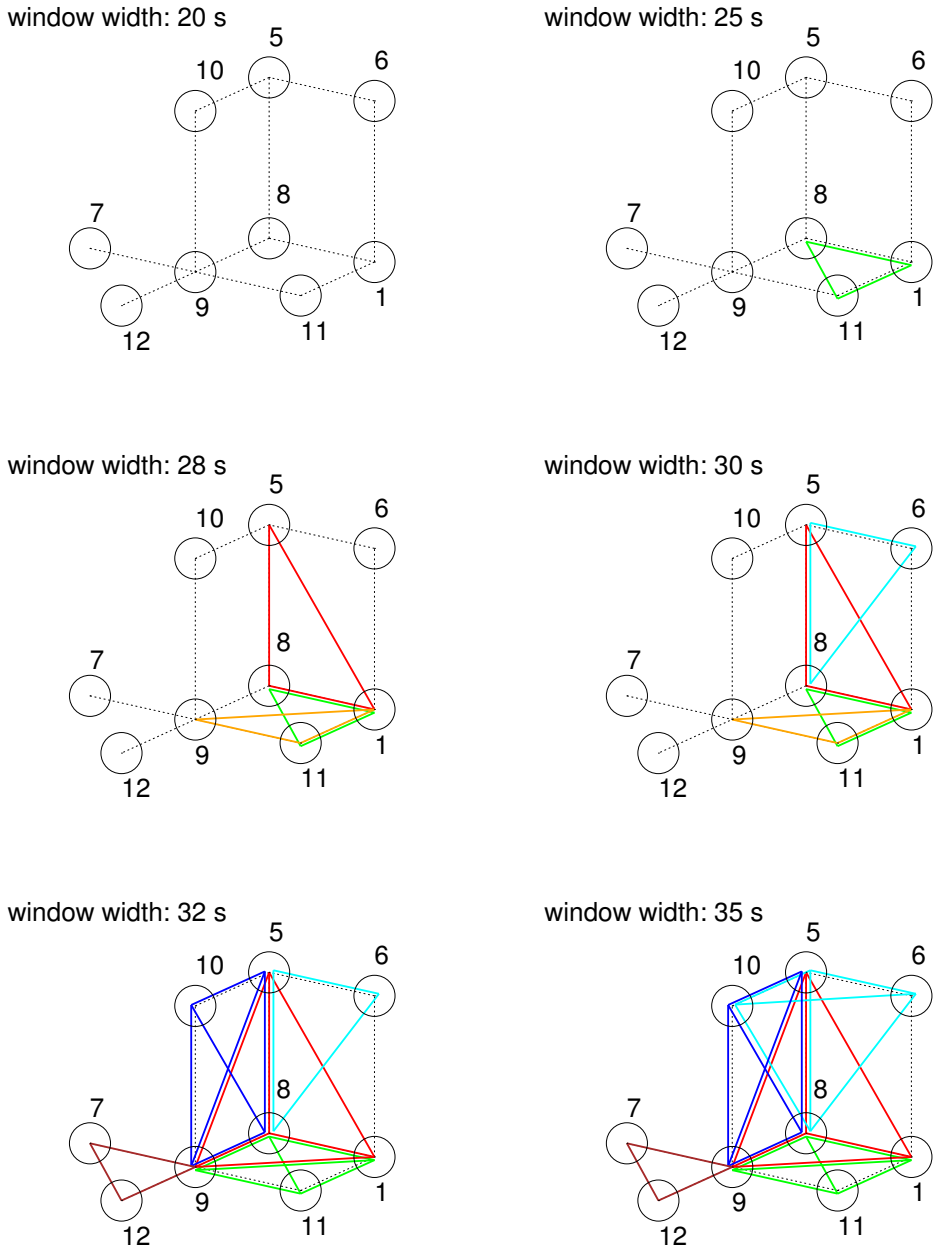

FIGURE 5.6: Schematic representation of fully–connected functional brain networks observed at different time scale resolution. Each network is highlighted by a different color and only minimum 3–nodes networks are considered. It is evident how the network configurations differ greatly changing the temporal resolution used to estimate the correlation between their nodes.

First, the differences between fMRI and MEG results can be due to a physiological response. As explained in Chapter 3, completely different physiological processes producing MEG and fMRI signals can be related to a similar neural activity. Hence, although their effects are reasonably correlated, differences in the morphology of the functional networks reconstructed with the two imaging techniques can occur.
Second, the configurations shown in Figure 5.6 are strictly dependent on the selection of parameters previously described (α, η_0, R_1, R_2). In this work they are chosen to guarantee results as conservative as possible. This choice probably explains the emerging of significant links only by using correlation windows larger than 25 s. In future developments of this work, the value of η_0 is going to be tuned according to the brain dynamics one wants to investigate: for example, the efficiency threshold can be lowered to take into accounts even sporadic couplings, for example associated with alternating brain states. This will allow to recognize a node pair as significantly linked even if the correlation is significant only in a small percentage of windows. The approach will be even more justified by enlarging the dataset both in terms of amount of subjects and recordings.
Another characteristic of the method that can limit the possibility to identify high frequencies correlations is the initial downsampling described in Section 4.1 to estimate the power time series: since it averages their contribution, it can compromise the identification of possible correlations at short window widths.
These considerations justify why the network morphologies obtained with the method described here and the results in Ref. [17] do not perfectly overlap. The two approaches rely on completely different assumptions: in Ref. [17], the identification of a window width showing a temporary absence of correlations for some nodes of the set (being correlated with the others for the remaining time); in our case, the determination of time scales at which the correlations exist, and the nodes involved, without any *a priori* knowledge. Moreover, the analysis performed in the work presented here is broadband, without previously filtering the signals in the α, β, γ, and δ bands.
A main goal of this work was to realize a simple, general, robust and versatile statistical test to assess significant correlations between the nodes of a network, independently of the nature of system. This result was fully achieved. To test the performance of the method, its characteristic parameters (α, η_0, R_1, R_2) were set in order to obtain a configuration as much conservative as possible, independently from any kind of neurophysiological considerations. Thus, it is possible to conclude that in Figure 5.6 are shown different networks of significantly related nodes, that correlates with a very stable dynamics. Moreover, they are surely belonging to a resting state network since the optimal observation windows ranges from 25 s to 35 s: this corresponds to the frequency interval $0.03 - 0.04$ Hz, completely included in the range of typical resting state frequencies $0.01 - 0.1$ Hz. Further neurophysiological interpretations are out of the scope of this thesis.
Once assessed the robustness of the method, it is possible to make some considerations about the correct selection of parameters according to the characteristic of the system. One of the strengths of this method is the possibility to tune the parameter values according to the needs: for example, a lower η_0 threshold would facilitate the observation of correlation events of low intensity and short temporal duration, as previously discussed.

5.5.1 Advantages and disadvantages of the method

The method described in this thesis is a new tool to assess correlation in network analysis. It can be applied to any kind of system, since the method does not impose any condition on the process underlying the production of the time series; it can merge the information obtained by multiple systems of the same nature or multiple occurrences of the same system; it is versatile, thanks to the presence of several degrees of freedom, given by the parameters that set the significance. Tuning their values allows to trim the results to more or less conservative conditions. Such parameters guarantees the robustness of the results obtained through a process to assess significance via generation of surrogates. Finally, the method is relatively simple, both in the application and in the interpretation of results. In addition, the estimation of the efficiency function provides information about the dynamics of the systems.
The core idea of the method is to estimate correlation at different window widths, allowing to investigate the dynamics of the system at different time resolutions. It is worth noticing that the method is *not* exactly a multiscale analysis, because it does not allow to observe the correlation at a specific time scale, identified by the window width of observation. The method described in this thesis is more similar to a *wide–band* analysis, where the band ranges from the minimum window width to the window width w of observation: the w value used for the correlation evaluation takes into account all the signal frequencies $\leqslant \frac{1}{w}$ and no filtering operation is performed to limit the analysis to a certain range of frequencies.

Many methods to study the interaction between a pair of variables exist, and many of them are based on correlation estimation. From this point of view, there is no novelty with regard to the method described in the thesis. On the other hand, it implements a new way to investigate the system dynamics compared to other existing statistical methods that rely on correlation. However, in the present form, the method shows several drawbacks, above all its being unsuitable to determine the indirect or direct nature of a link, and, in the direct case, which is its direction (see Paragraph 4.3.1). To address these questions other methods, as mutual information, partial correlation or entropy-based ones, are more appropriated [19, 24].

By exploiting its general applicability, in the next Chapter I discuss a completely different field of research in which the same method is applied.

Chapter 6

Cross–correlations in weather time series analysis

6.1 Introduction

In this Chapter I present an application of concepts introduced in the previous chapters to a problem belonging to climate research: the wind circulation network in Trentino region. In the first section I provide a general overview on the application of complex networks to climatic studies, in terms of examples, methods, advantages and methodological open issues. The second section concerns the preliminary results of our analysis, in which the methodology is highlighted and possible further developments are discussed.
In Chapters 4 and 5, the complex system object of our analysis was the human brain. As we saw, a widely used approach to model the brain functioning consists in identifying *communication networks* (or better, functional networks, see Chapters 3) between different cerebral areas. This is performed on the basis of how much their activity is correlated, no matter which kind of signal is used.
In many cases, complex networks are powerful tools to more easily investigate the dynamics of a complex system: the elements of the system are modeled as the nodes of the networks and their relations are outlined by means of links. Other examples of complex systems exist, such that neither their elements nor their links are easy to recognize. One of these systems is the climate. In the 60s, Lorentz was the first proposing to model the Earth climate as a complex system, ruled by non–linear dynamics. His pioneering works addressed non–periodic flows and their application to the atmosphere modeling and weather prediction [44, 45].
In the following, I describe the main characteristics of the climate system and the most used approaches to estimate the network structure.

6.1.1 State of the Art

Although the *climate system* is actually a set of elements interacting through physical relations, the use of a complex network to model the behavior of the $\sim 10^{44}$ atmosphere molecules is of course impracticable. Probably for this reason, the first network approach to model global climate was proposed only 15 years ago, in the seminal work by Tsonis and Roebber in 2004 [79]. In this work, the authors propose a new way to identify the elements (also known as agents, vertices or *nodes*) and their links. The Tsonis and Roebber method (that was going to be the standard one in the successive climate network studies) consists in defining a spatio–temporal grid on the whole globe (see an example in Figure 6.1), and thinking the climate system as a network of dynamical systems. The network nodes are the grid cells, connected

FIGURE 6.1: A schematic representation of a whole–globe grid. Each grid cell represents a node of the network. The grid resolution can change according to needs and data availability, and its extension can be reduced to localized regions.

to each other not on the basis of their spatial proximity but according to their statistical similarity in climate variability during the recording period. This approach is particularly suitable to investigate the system at different spatial and temporal scale resolutions as well as its temporal evolution.
The way with which both nodes and links are determined is not fixed and, according to their definition, the network morphology, dimension and complexity can considerably vary. In the following, I give a short overview of the applications of complex networks in meteorological studies, in terms of data, analysis, methods and significance tests.

6.1.2 Meteorological data and preprocessing

Case studies

As previously mentioned, the application of complex networks to climatic studies is quite recent and the literature covering this topic is still not very large.
Until now, the vast majority of the works uses the network approach to address large scale meteorological events. As already mentioned, the first were Tsonis and Roebber [79] who focused on the topological properties of the climate network. They discovered the existance of a *small–world* organization [81] in the network and the presence of two interacting sub–networks that cooperate in the general organization of the global climate. They also identified *supernodes*, which are hub nodes characterized by a great amount of links with very long connections, also known as *teleconnections*. In the following works by Tsonis and other collegues [76, 78] these topics were further investigated, highlighting the role of teleconnections in the stability of the climate network and in how rapidly information is transmitted.

Other works took into account specific global–scale phenomena and their role inside the general climatic network. Examples include El Niño [27–29, 84], La Niña [77], the communication between supernodes and the Rossby waves [80]. The favorite field of investigation on El Niño concern how it interacts and affects the overall network, temporarly disrupting connections between the various global regions, as in *blinking* links [28, 84]. Many other studies address the problem of the network structure and dynamics. As mentioned before, the presence of supernodes (as the NAO, the Pacific North American pattern or the Pacific South American pattern [76, 78] and teleconnections ensure an efficient and fast information transfer between far away geographical locations ($>$ 2000 km). Moreover, the knowledge of structural properties of the network makes possible to investigate the long–term temporal evolution of the whole system, which is very important in the field of meteorological forecasting [70, 71], and to understand the fluxes of dynamical information through the climate network [19, 21]. Concerning this, Boers *et al.* [8] recently proposed a global model to investigate the synchronicity of rainfall events.
Complex network approaches to non–global, limited geographical regions are less frequent. An important investigation topic is related to large local precipitation events. Concerning monsoons, for example, the most important issue is to understand the dynamics of wind circulation in the involved regions (India [46] and South America [26]) in order to realize a prediction model of rainfalls. A similar purpose, despite the different intensity of the phenomenon, was addressed by Rheinwalt *et al.* [65], who realized a model for precipitation forecast in Germany.

Meteorological parameters and preprocessing of data

A lot of meteorological parameters are periodically acquired all over the world thanks to weather satellites, since the 50s. The most used climatic parameters to realize climatic complex networks are the surface air temperature (SAT), meaning the temperature measured at ground level, and the geopotential height, which is the elevation at which the pressure equals a certain predefined value [4, 19, 27, 76, 78, 79]. Several other parameters are available, as the precipitation levels, the relative humidity, or the horizontal and vertical wind speed [26, 64]. Steinhaeuser *et al.* in 2011 [70] propose a multivariate predictive model by combining different meteorological variables. The method realizes networks by means of the information provided by each meteorological variable separately and then it compares such networks, identifying their interactions. It is worth noting that, unless in few cases, wind speed data are not frequently exploited in climate network reconstruction. However, some studies in the past addressed correlations in wind intensity between couples of meteorological stations, to obtain wind forecasting and information about their exploitation for energetic purposes. [cit]
Climatic data are organized in time series, acquired from different geographical locations and, often, over a period between 40 and 60 years. The acquisition nodes are identified over a spatial grid defined in different ways: sometimes it covers the whole globe [4, 19, 70, 71, 76, 78, 79], in other cases only particular regions of interest [6, 26, 64]. The grid resolution is also not fixed, but the most common is 5° longitude $\times$ 5° latitude.
As regards the sample frequency of time series, it is worth noticing that, in particular for global climate networks, the temporal resolution is quite low. In most cases, data are acquired on a monthly bases [4, 19, 70, 71, 76, 78, 79], but there are examples of daily acquisitions, both for global networks [8, 28, 30, 80] and for regional ones [29, 46, 64]. Higher temporal resolutions are very rare [85].

Most of the times, the meteorological time series are not used in their raw form but a preliminary pre–processing operation is necessary. Climatic data, in fact, are deeply affected by seasonality and annual trends that can produce spurious correlations between nodes. To avoid this risk, the series are detrended by removing all possible effects due to season cycles, turning them into *anomaly time series*. Only the values outside the seasonal mean are taken into account, and the similarities between the different geographical locations are estimated on the basis of these anomalies. In some works [26, 29, 76, 79] the authors decided not to consider the whole year to perform the analysis but only the winter months, to avoid the effects of the annual cycle. Donges *et al.* [19], however, claim that their results are not significantly affected by considering the entire year.

6.1.3 Time evolution, time scale resolution and topology of the networks

Almost all works focus on topological considerations about network structures. This is performed by estimating some well–known parameters of the graph theory (as clustering coefficient or betweenness centrality [19, 76, 79]) to obtain information about the dimension of the network, the amount of links and their distribution. In some cases, the network structure is analyzed at different spatial scale resolutions [20].
Many works also handle the problem of the dynamical evolution of networks. This is possible thanks to the great amount of data covering many decades. For example, Berezin *et al.* [6] and Guez *et al.* [29] address the problem of the stability of the climate networks; on the other hand, Erbert-Uphoff *et al.* [21] realize a network where the nodes are identified in*all* the geographical locations for *every* possible acquisition time. This way, every node i can be connected with any contemporary node j or with any other node in the future, itself included, allowing to understand the evolution of the network.
Each data of the network observation represents a time average over a temporal interval depending by the sampling rate of the time series. Evaluating "instantaneous similarities" (zero–lag, as we have seen in the Chapter 4) between the behavior of the nodes, effectively means to look at data over a time scale in the order of a day or a month.
However, to our knowledge, no study addressed the issue of how the network configuration changes by observing it at different time scale resolutions. This problem, as previously discussed in the case of functional brain networks, will be elaborated further in our preliminary work.

6.1.4 Link determination

The main issue in the complex network approach is identifying connections, or links, between nodes. The way in which these connections are identified does not rely on the geographical proximity of the locations, but on the behavior similarities of the observed parameters in those locations. There are a lot of methods that have been proposed to correctly estimate the communication paths between the network nodes. The vast majority are linear methods, as cross–correlation or covariance. For event–like parameters as the occurrence of heavy rainfalls, the event synchronization is often used as well (see below). Moreover, some authors [4, 20] proposed to use non–linear methods to highlight the presence of non–linear dynamics, likely present in a complex system like the climate.

In the following paragraphs, I will present the most frequently used techniques for link determination.

Linear methods

The most common linear method to identify similarities between two time series recorded from a pair of nodes is cross–correlation. Many works determine the presence of a link and, in some cases, its strength (or *weight*) by estimating the Pearson correlation coefficient [28, 30, 70, 76, 78, 80, 84, 85]. Another widely used method is the covariance[6, 27, 29]. Both techniques are covered in Chapter 2). In both cases, measures can be performed at zero–lag or by considering some delays. The use of zero–lag measures is often justified as a consequence of the sampling rate of the time series, as mentioned in the previous paragraph: especially for monthly values, the time scale of observation is not instantaneous, even if correlations or covariances are estimated without delay, but has the same order as the acquisition rate [76]. On the other hand, many studies investigate the time shift τ at which correlation or covariance are maximized. Knowing τ, some works identify the link direction – according to the sign of the shift – and/or its weight, often calculated as $[\mathrm{MAX}(C_{i,j}) - \mu(C_{i,j})]/\sigma(C_{i,j})$, where C can be the correlation or the covariance between two nodes (i, j) [6, 27–30]. Moreover, the analysis of different time lags allows to investigate the system evolution and the duration of the climatic phenomena.

Non–linear methods

In order to investigate the non–linear properties of the climate complex system, some authors proposed to use alternative methods instead of the linear ones previously described. The mutual information is a non–linear method measuring the mutual dependence between two time series. In other words, it quantifies the excess in the amount of information shared by two time series falsely assumed as independent. Donges *et al.* [20] compared the climate networks obtained by using a linear and a non–linear technique to identify the links on the same set of data: the zero–lag Pearson correlation and the zero–lag mutual information. Interestingly, despite the complex nature of the system, the results obtained with the two method in terms of link identification are to a large extent comparable, in particular, at a local and mesoscopic scale. This outcome justifies the strong preference towards linear methods also in the following works about climate networks [70].
However, despite the similarities, some differences are still present. This is particularly true for a topological parameter, the betweennes centrality (BC), especially when estimated on a global scale, because its values obtained with the two methods are not comparable. The betweenness centrality quantifies the amount of network information flowing through a node. The BC is a very sensitive parameter that identifies structures in a global network that are involved in the transport of dynamical information. It is possible that, at a global scale, the network structure is more affected by non–linear dynamics.
Few approaches propose to use symbolic dynamics to investigate the non–linearity of meteorological systems. Barreiro *et al.* in 2011 [4] reformulate the mutual information definition on the basis of another complexity measure, the Permutation Entropy. This is a method of symbolic dynamics used to investigate the presence of periodic patterns of oscillation in the global network behavior. Moreover, the work in Ref. [4]. is the only one that partially addresses the observation of the network at different time scales, even if by using an approach which is very different from ours.

Synchronization method

Meteorological time series are not all the same. Their characteristics are different not only according to their acquisition period or sampling frequency, but they might also represent different climatic parameters. Some of them are "event–like" time series, formed by *events* that can be defined in different ways, for example when the value of the observed parameter overcomes a certain threshold. In this case, the previously described techniques are not ideal and the event synchronization (ES) method is more efficient. ES checks how many events happen simultaneously: the more concomitant events occur, the more the time series can be considered as synchronized. Event synchronization is used by Malik *et al.* in 2010 [46] to model the rainfall dynamics during the monsoon in India, whereas Boers *et al.* in 2019 [8] address the problem of rainfall synchronicity on a global scale. Rheinwalt et al in 2016 [65] propose a modified version of the ES method to estimate isochrones of heavy precipitations in Germany.

6.1.5 Significance tests

The correct estimation of network links is a major issue in the complex network approach.
One of the most common methods to identify reliable links is by defining a threshold of significance: whenever an estimator such as the correlation coefficient r overcomes the threshold, the link is considered as real, conversely the correlation is considered to be due to noise fluctuations. The same applies to any other linear or non–linear method estimator. The way to identify the best threshold is, unfortunately, not fixed. In many of the Tsonis' works about climate networks [76, 79], t-test and Kolmogorov–Smirnov test are used to select the significance threshold of correlation, identifying it as equal to 0.5. If $r \geq 0.5$, the result is significant with 99% confidence (corresponding to a p–value of 0.01). A more stringent threshold is proposed by Steinheauser *et al.* [70] where, by using a two sided t-test and a confidence intervals based on Fisher transformation, the level of significance are fixed to the very conservative p–value of 10^{-10}.
Another common technique to estimate significance consists in producing surrogates of the original time series. Even in this case, there are many ways to create surrogates: the easiest one implies to shuffle the original time series, maintaining the same value distribution but disrupting the possible dependence between neighboring data [4, 6, 29, 80]. Few other papers provide the distribution from which surrogates are derived, according to a suitable null hypothesis. For instance, Boers *et al.* [8] assume that the original time series are randomly and uniformly distributed, whereas Donges *et al.* [19] compare different kind of surrogates method, such as randomly shuffled time series, Fourier surrogates and twin surrogates.
In other cases no threshold is defined: Gozolchiani *et al.* [28], for example, consider all links obtained as reliable, and the correlation coefficient is only used to determine the strength of the connection.
Guez *et al.* [29] commented on the fact that the topology of networks related to the same physical quantity can be very different depending on the link definition, although the diverse methods should all measure the similarity level between time series. One of the possible reasons they propose is the presence of strong autocorrelation in time series, which ultimately affects the analysis introducing spurious correlations.

As explained in details in Chapter 4, our method defines a new way to calculate the zero–delay cross–correlation between pairs of time series of generic nature at different time scale resolution. To our knowledge, this way to perform cross–correlation has never been used to reconstruct meteorological networks. Thus, we propose a preliminary study in which we analyze wind intensity time series recorded from a set of meteorological stations spread over the province of Trento, to highlight the presence of wind circulation networks across the region.

6.2 A preliminary study

6.2.1 Dataset and preprocessing

In the previous paragraphs, I highlighted the problem of node identification in climate network, because in many cases the acquisition of meteorological data is performed with satellites. In our case this is not a problem, because the wind intensity time series are recorded by terrestrial meteorological stations, thus the nodes correspond to the stations themselves. In Figure 6.2 the locations of the nodes chosen in the Trentino region are shown. All used data were taken from the open–access online dataset MeteoTrentino [49]. The website collects data from hundreds of meteorological stations, covering almost the whole region surface. A set of 25 stations (listed in Table 6.1) was selected so that it shows a sufficiently homogeneous distribution in term of geographical location.

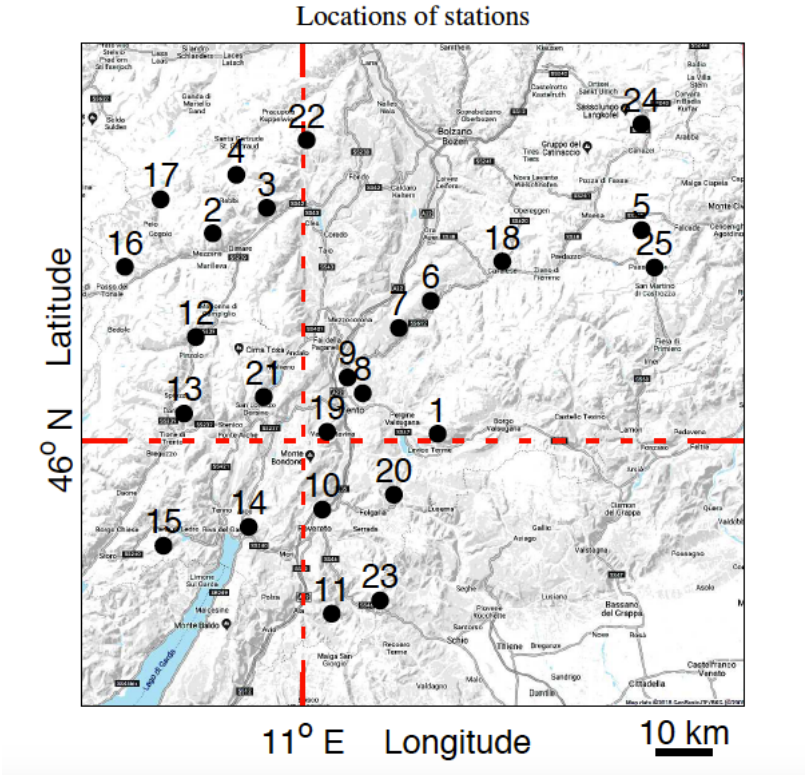

FIGURE 6.2: Geographical locations of the 25 meteorological stations. The red, dashed lines mark the point of coordinates 46° N, 11° E, used as reference in Table I.

For each station we have one recording spanning over a period of one year, from 15–09–2016 to 15–09–2017. The wind speed values is in m/s, recorded with a sampling

#	Name	Longitude	Latitude	Elevation [m]
11	Ala	3.90′	-15.66′	692
24	Canazei	45.96′	28.68′	1465
18	Cavalese	27.06′	17.10′	958
7	Cembra	13.02′	10.20′	652
1	Levico	18.30′	0.60′	502
3	Malé	-4.92′	21.06′	720
2	Mezzana	-12.30′	18.78′	905
19	Monte Bondone	3.24′	0.78′	1490
16	Passo Del Tonale	-24.24′	15.72′	1875
23	Passo Pian delle Fugazze	10.44′	-14.52′	1170
5	Passo Rolle	47.22′	17.88′	2012
20	Passo Sommo	12.36′	-4.92′	1360
17	Peio	-19.32′	21.84′	1585
12	Pinzolo	-14.58′	9.36′	760
4	Rabbi	-9.06′	24.06′	1132
10	Rovereto	2.58′	-6.24′	203
22	Rumo	0.48′	27.18′	1100
21	San Lorenzo	-5.34′	3.96′	685
6	Segonzano	17.34′	12.66′	660
25	S. Martino di Castrozza	47.76′	15.66′	1470
13	Tione	-16.20′	2.46′	533
14	Torbole	-7.38′	-7.80′	90
15	Tremalzo	-18.96′	-9.54′	1560
8	Trento (Laste)	8.10′	4.26′	312
9	Trento (Roncafort)	6.06′	5.70′	194

TABLE 6.1: Coordinates and elevations of the 25 meteorological stations used in this work Locations of the 25 weather stations. Latitude and longitude are expressed as the distance in minutes of arc from the point 46° N, 11° E, marked by the red, dashed lines in the map of Fig. 1. It is worth mentioning that a minute of arc of latitude corresponds to one nautical mile (1.86 km), while a minute of arc of longitude is about 0.695 miles at these latitudes. The number assigned to each station (# column) follows the numbering order provided by the archive from which the data have been retrieved [49].

rate of 10 minutes and a resolution of 0.1 m/s. Each time series is divided in two parts approximately corresponding to the "winter season" (15 September 2016 – 15 March 2017) and the "summer season" (15 March 2017– 15 September 2017). The final length of the series is of 26065 samples.
During the recording, some acquisition error often occurs, causing losses of data. In our dataset, the amount of failed measures is at most 0.2% of the series samples. However, to ensure time series comparability, we replace the missing points with a linear interpolation between the neighboring samples.
The poor resolution of 0.1 m/s can be another issue affecting the data. This characteristic, in case of very low wind intensity, can produce sequences of consecutive zeros in the time series. Whenever the correlation window width corresponds to one of these sequences, it induces a divergent correlation coefficient (see 4.4 in Chapter 4). To prevent this effect, we adjust data by adding a normally distributed random variable, with vanishing mean and standard deviation $\sigma = 0.01$ m/s (1/10 of the measure resolution). This adjustment overcomes the problem without affecting the correlation measure.

6.2.2 Looking for links

Once the time series corresponding to the set of nodes are preprocessed, it is possible to proceed with the identification of links. To do this, we follow basically the same steps as in Chapter 4, although with some slight modifications.
The sequence of $s_n[i]$ of wind intensity values, collected by the n-th station, corresponds to the time series $s_n(iT)$. The variable i runs from 0 to 26064 and $T = 10$ minutes is the sampling period. As we did for MEG analysis in Chapter 4, we are going to define the correlation window $F_w[k]$ to perform the correlation analysis:

$$F_w[k] = \{i | k_0 + 48k - 24w < i \leq k_0 + 48k + 24w\} \ . \tag{6.1}$$

Even in this case, k_0 is an offset – now corresponding to 2880 points – on the window center position, such that, even for the largest window width w, the running window is always inside the time series. The parameter w, which determines the window width, spans over the interval $\{1; 120\}$, whereas k, which identifies the window center position, goes from 0 to 419. As in the MEG case, running windows with the same k have the same window center position, regardless of w. The number of points inside a window is given by $N = 48\, w$ and ranges from a minimum of 8 hours (480 minutes) to a maximum of 40 days (57600 minutes).
The calculation of the Pearson correlation coefficient is carried out by considering a pair of stations (n, m), and using the same formula as in Eq. 4.3 to estimate the zero–delay cross–correlation term of the corresponding time series pair s_n, s_m:

$$C_{n,m}(w)[k] = \sum_{\forall i \in F_w[k]} \delta s_n[i] \cdot \delta s_m[i] \, , \tag{6.2}$$

where:

$$\begin{aligned} \delta s_n[i] &= s_n[i] - \langle s_n[i] \rangle_F \\ \delta s_m[i] &= s_m[i] - \langle s_m[i] \rangle_F \ . \end{aligned}$$

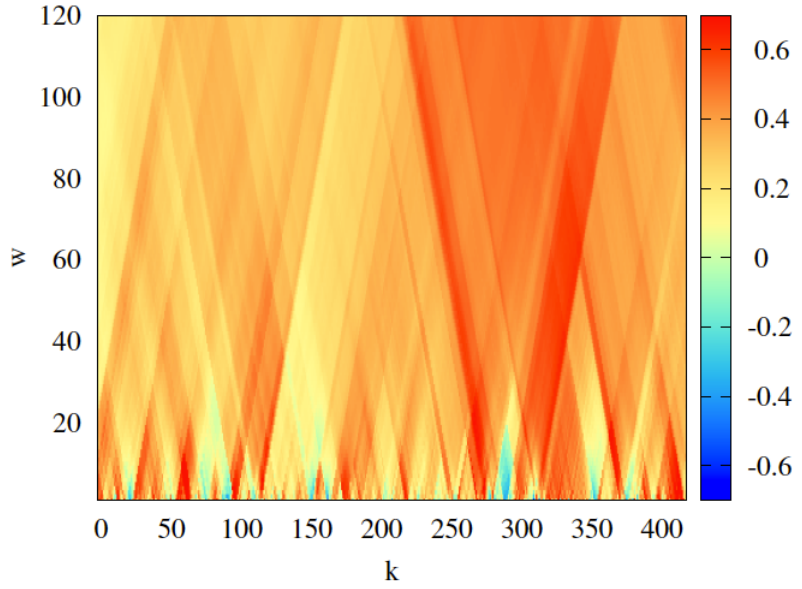

FIGURE 6.3: Correlation diagram for the winter time series of stations 8 and 9. The color scale shows r8,9(w)[k] as a function of k and w. The triangular structures are referred to as funnel–like structures.

The angular brackets $\langle\cdot\rangle_F$ represents the sample mean of the elements of the sequence inside the window $F_w[k]$. As in Eq. 4.4, the Pearson correlation coefficient is given by:

$$r_{n,m}(w)[k] = \frac{C_{n,m}(w)[k]}{\sqrt{C_{n,n}(w)[k] \cdot C_{m,m}(w)[k]}}. \tag{6.3}$$

Even in this case, we estimate the correlation at zero–delay because the wind orientation – and thus the "communication direction" – is not known. Conversely, there is obviously no need to average the correlation coefficient as we performed in Eq. 4.5, because there is no issue of spurious correlations due to source localization reconstruction. Once the correlation coefficient for every time series pair and window width is estimated the correlation diagrams, one for each pair, are computed similarly to those discussed in Chapter 4. An example is shown in Figure 6.3.

Test of significance

We use the method of surrogates previously discussed in Paragraph 4.2.2 to test the significance of the correlations. The null hypothesis $H_{0,S}$ assumes that a generic pair of the original time series, recorded by the n and m stations, are independent and each given by a Gaussian noise sources having the same wind speed distribution and approximately the same power spectrum. According to this hypothesis, we generate 1000 pairs of surrogates, estimating the coefficient diagram for each of these pairs. The p–value is calculated by ranking the correlation coefficient of the original pair with respect to the surrogates and then normalizing by 1000.
By looking at Figure 6.4, the *funnels*, namely triangular patterns similar to those observed during the MEG analysis, are visible. These structures are due to the effects of shared correlated events in the two sequences and their shape is justified by the same considerations explained in Chapter 4. As in MEG case, if the window width

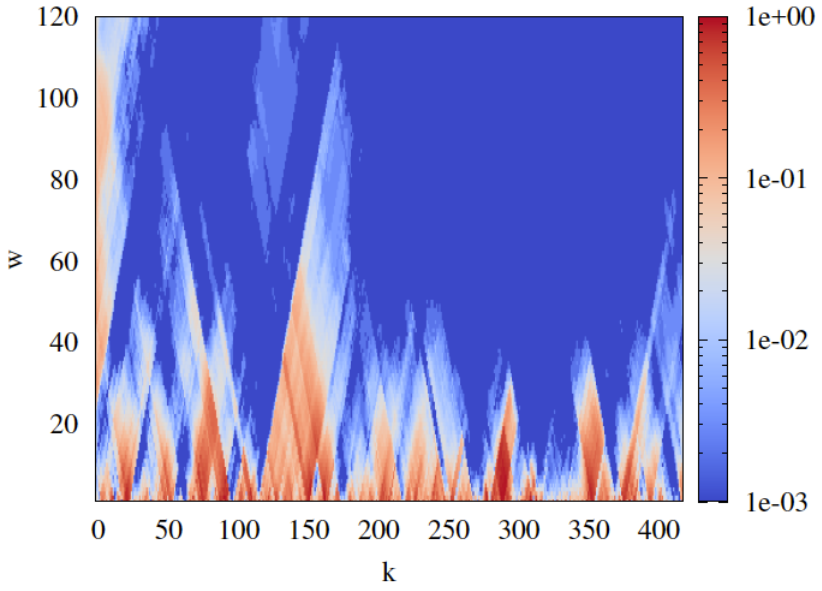

FIGURE 6.4: Diagram of p–values corresponding to the correlation diagram of Fig. 6.3

W is greater than the time scale of a correlation event, each value $w \geq W$ will still include the event, thus resulting in a significant correlation. However, increasing w, and thus the number N of points inside the correlation window, causes r to decrease as $1/N$, because of the increasing energy contribution of the noise component against the signal. This behavior, however, is not visible in the diagram in Figure 6.4. This fact has two explanations. The first one is that the window width interval is not large enough to measure the vanishing effect, discussed in Section 4.2.1. The second one comes from the contribution of multiple correlation events within the same correlation window in the case of a sufficiently large value of w, which slows down the attenuation of r.

Efficiency

Once the correlation diagrams and their corresponding p–value diagrams are estimated, the *efficiency* of each window w in finding significant correlations can be evaluated as discussed in Paragraph 4.2.3. The efficiency $\eta(w)$ quantifies the number of windows with the same width w whose correlation p–value is less than a certain threshold α. We choose $\alpha = 0.01$. Correlations with a greater p–value deemed to be produced by random fluctuations.
The existence of a link depends on a second threshold that is the minimum amount of significant windows to determine the presence of a link between the two nodes. In this case an even more stringent choice than that one performed in the MEG signal analysis is made, namely $\eta_0 = 0.75$, meaning that at least 75% of the running windows must be significantly correlated to determine the presence of a link.

6.2.3 Seasonality considerations

As we discussed in Section 4.2.3, climatic time series are deeply affected by periodicity effects, due to seasonal changes, solar irradiation, daily cycle, etc. The presence

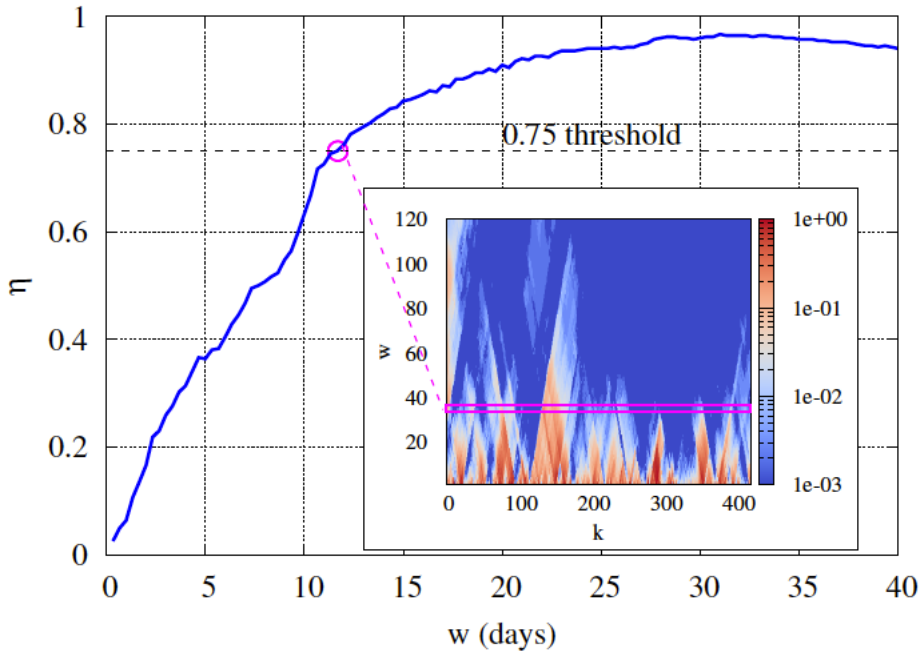

FIGURE 6.5: Graph of the efficiency η(w) corresponding to the p–value diagram of Fig. 6.4, which is replicated for clarity in the inset. The threshold $\eta_0 = 0.75$ threshold is shown as a dashed line. The diagram row corresponding to the window width W at which the threshold is reached is highlighted in the inset through the magenta border.

of these oscillations can produce spurious correlations, thus spoiling the process of network reconstruction. For these reasons, in the literature, a great effort is usually devoted to an extensive clean–up of the data, producing the so called *anomaly* time series (see 6.1.2).

We also observe this kind of periodical oscillations, in particular the 24 h cycle induced by the solar irradiation. The origin of the effect is confirmed by the fact that each station, independently of its location, has the same oscillation frequency, though with varying amplitude. The different amplitudes are a consequence of the different irradiation the stations receive, due, for example, to their geographical position. This effect is particularly strong in summer, as an obvious result of a larger solar irradiation, with respect to winter months.

The two behaviors are compared in Figure 6.6. The top graph shows the average efficiency curves estimated on data recorded in January: the red and blue colors refer to two different stations, 2 and 4 respectively. The bottom plot is structure in the same way but the curves are calculated by using the wind intensity values acquired in July. It is clearly visible that, during the summer month, the contribution of the daily oscillations is much more evident.

The effects of this dynamics are visible in Figure 6.7 as well. The two curves represent the average efficiency estimated for the "summer" and "winter" periods over the entire dataset. Both curves show the same behavior, however, during summer the contribution of the daily oscillations are more evident, thus enhancing the efficiency of smaller windows and leading to the presence of spurious correlations. In order to preserve the information as much as possible, we decided to process only the time series corresponding to the winter months.

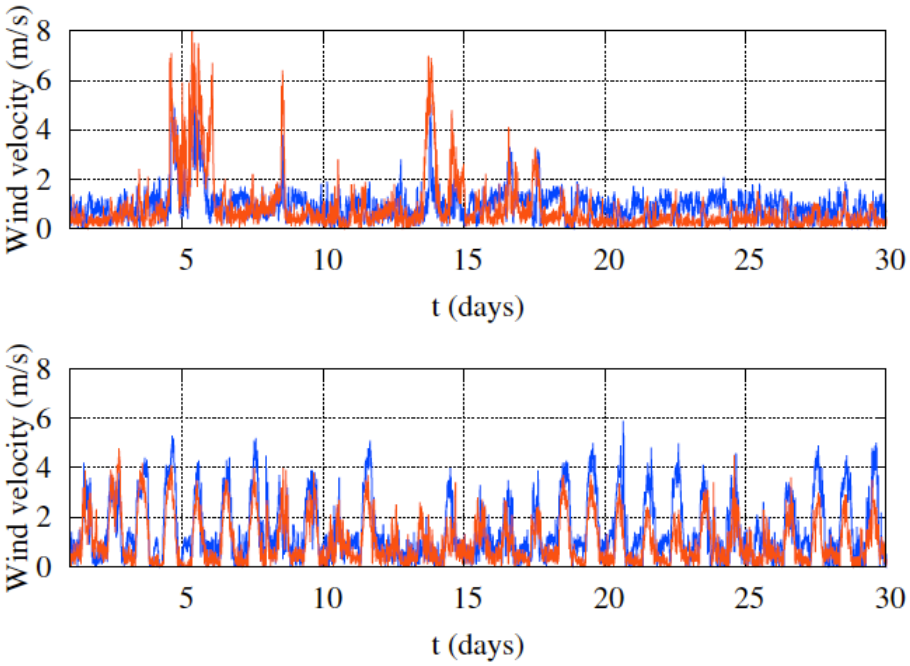

FIGURE 6.6: Comparison between the behavior of summer and winter time series for stations 2 and 4. The effects of different solar irradiation according to the season is clearly visible. The 24 h periodicity of the time series recorded in July 2017 (bottom) is much more evident than in January 2017 time series (top) where it is almost absent. The strong periodicity due to the solar forcing during summer can produce spurious correlations in links estimations, whence the decision to use only winter time series.

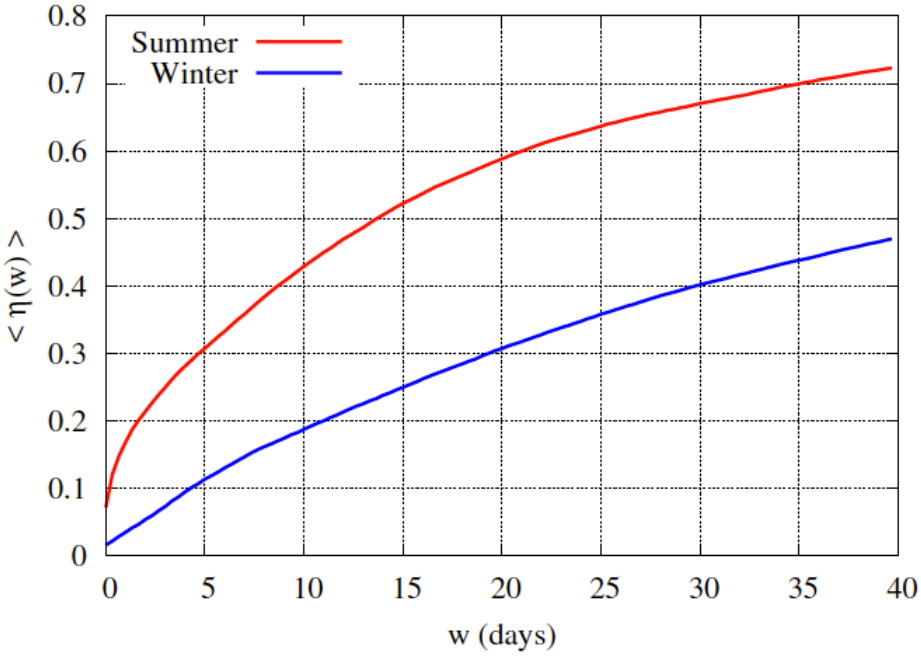

FIGURE 6.7: Comparison between the average efficiency curve estimated for the summer months (red curve) and the winter months (blue curve) over the whole dataset.

6.2.4 Networks

By means of the efficiency curves, the existence of a link and the minimum temporal window at which such link is observed can be determined. Again, the network structure is different according to the window width w of observation: temporal sequences that are uncorrelated at small time scale can be correlated if observed with larger window width, thus producing different network structures for the same set of data. For small value of w, there are few nodes showing a link, whereas by enlarging w more complex structures emerge and other connections appear.
In the graphical representation of Figure 6.8, the network structure at two different time scale, 15 and 30 days, are shown. At these time scales, only few nodes show significant connections, whereas by enlarging the correlation window more links appear, revealing a complex network structure. The emerging clusters of nodes are highlighted with different colors. As done with the brain functional networks, the algorithm identifies fully–connected networks, i.e. clusters of nodes in which each node shows a connection with every other node of the cluster. In this case, however, we decided to slightly relax this constraint, by merging fully–connected clusters that share all the links except one and considering them as a single network.
The final structure of the network shows two main clusters, colored in red and blue in Figure 6.8. In the red one, that forms a fully–connected network only with nodes 17, 22 and 24, nodes 2, 3, and 4 are added as well because they show links only with this cluster. Its main characteristic is that all stations involved are located at an altitude above 700 m, with an average elevation above 1000 m (see Figure 6.9). The blue cluster shows the first significant connection already at lower time scale resolutions. It also reveals a more complex cluster at 30 days of time scale, with all nodes distributed in the outskirts of the Adige Valley. Moreover, all the nodes belonging to this cluster are placed at relatively low altitude ($<$ 700 m), with an

average elevation lower than 500 m. Looking at the bottom graph of Figure 6.8, two particular nodes, the 18 and 25, are worth noticing that show connections with the red and the blue clusters, seeming to have a sort of "bridging" function between the two. All nodes having connections with 18 and 25 are marked in orange. Finally, links that could not be accounted for with this procedure are marked in light green.

6.2.5 Discussion

To our knowledge, a clear definition of the wind circulation patterns in Trentino does not exist, the emerging nodes clusterization seems to be reasonable according to some topological characteristic of the region.
Looking at Figures 6.9, the altitude and the latitude appear as the most relevant features to better separate the clusters. This can be a hint of the communication dynamics. Excluding, at this stage, the green cluster from the following considerations, the method identifies 3 main separated clusters. The red network is extended mainly along the longitudinal direction, with a mean internal communication direction along the east–west axis. The stations belonging to this network are located almost at the same latitude (46.4°N in Figure 6.9) and on high ground (above 700 m), despite being far away from each other (see Figure 6.8). Being the northernmost and the highest stations, they are likely to intercept the wind fronts as soon as they overcome the Alps. On the other hand, the blue network has a much more compact and symmetric diamond–like structure from both the latitudinal and longitudinal point of view, which can be a consequence of the valley orography.
The yellow network behaves as a sort of connector between the other two clusters. It has been built under different assumptions with respect to the other ones. In addition, it is not a fully connected network. After the identification of nodes 18 and 25 as the "bridges" between the other two clusters, all other nodes significantly linked with them are considered as belonging to the network. The nodes 18 and 25 can be seen as two gateways, able to transfer information between the red and blue clusters along the north–south axis. They also sort information between different altitude levels, e.g. connecting a low altitude network (blue) with a higher one (green). Node 25 seems to correlate its activity with both higher and lower altitude nodes, whereas the information through node 18 cannot reach the highest green nodes if not by passing through node 25.
In conclusion, this preliminary analysis highlights the presence of patterns of wind circulation across Trentino, showing the presence of relations between different geographic locations that do not generally correspond to spatial proximity, but, in the vast majority of cases, share some topographical characteristics as latitude, longitude or altitude.
However, these considerations are not sufficient to fully understand all the links we observe, nor the lacking of other expected links based on the same assumptions (e.g. nodes 20 and 23). The orography of the region is highly complex and of course produces local effects that influence the general circulation network and that cannot be measured with this kind of analysis. Climatic effects produced by neighboring regions might have an effect on the wind dynamics of Trentino.
In Chapter 4, we already presented how the parameter selection, as the efficiency level and the significance threshold, can potentially affect the resulting network structure. In this analysis, we presented results based on a reasonable choice of η_0 and α. However, being a preliminary study, we did not yet explore a large parameter space to test the robustness of the networks we found.

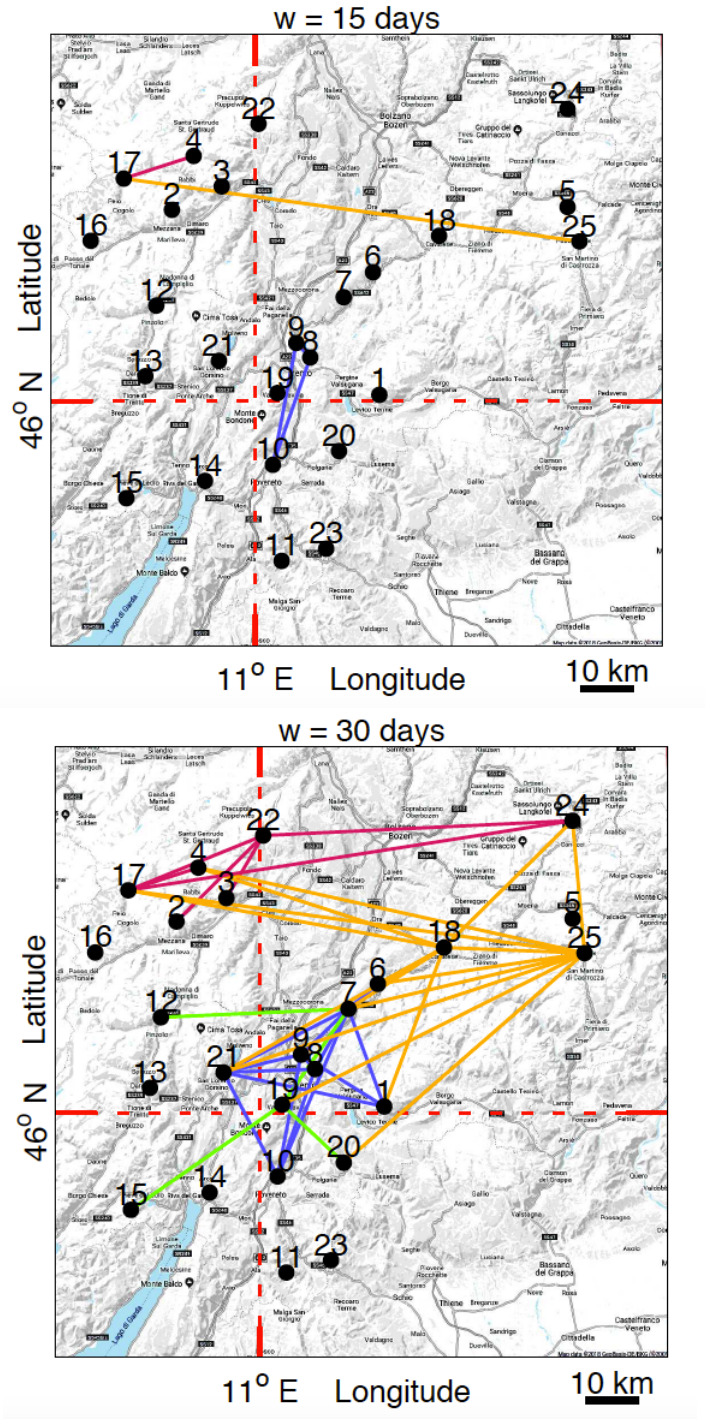

FIGURE 6.8: Links present at a time scale of 15 days (top) and 30 days (bottom). The meaning of colors is described in the main text. The red, dashed lines mark the point of coordinates 46° N, 11° E, as in Fig. 6.2

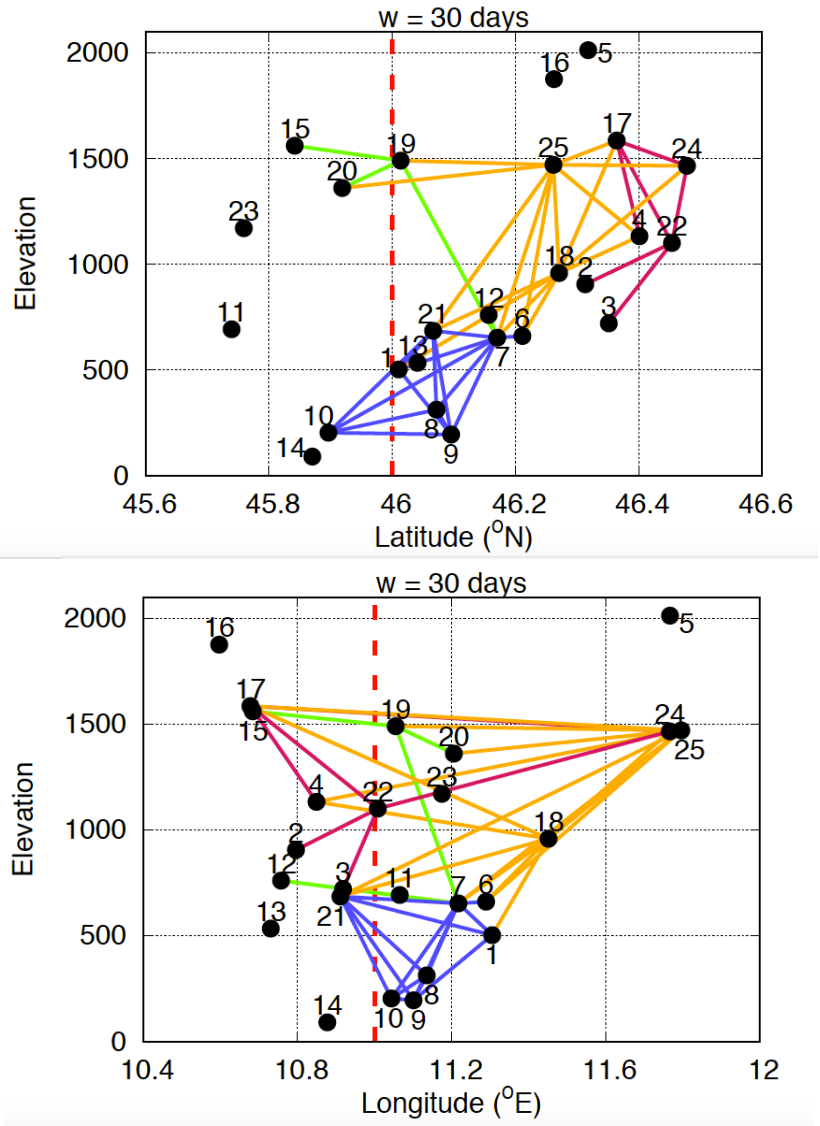

FIGURE 6.9: Links present at a time scale of 30 days, as in Fig. 6.8(bottom), with the stations shown in the latitude–elevation coordinate system (top) and in the longitude elevation one (bottom). The red, dashed lines delineate the 11° E and 46° N coordinates as in Fig. 6.2.

Chapter 7

Conclusions

In this thesis an innovative approach to assess connectivity in a complex network was proposed. In network connectivity studies, a major problem is to estimate the links between the elements of a system in a robust and reliable way. To address this issue, a statistical method based on Pearson's correlation coefficient was proposed. The former inherits the versatility of the latter, declined in a general applicability to any kind of system and the capability to evaluate cross–correlation of time series pairs both simultaneously and at different time lags. In addition, our method has an increased "investigation power", allowing to estimate correlation at different time scale–resolutions.
The method was tested on two very different kind of systems: the brain and a set of meteorological stations in the Trentino region. In both cases, the purpose was to reconstruct the existence of significant links between the elements of the two systems at different temporal resolutions.
In the first case, the signals used to reconstruct the networks are magnetoencephalographic (MEG) recordings acquired from human subjects in resting–state. The dataset consisted in 15 MEG recordings of 6–minutes length stemming from five different subjects. After a proper preprocessing of the data, zero–delays cross–correlations were estimated on a set of 12 MEG time series corresponding to as many brain locations. Ten regions of this set are deemed to belong to a well–known resting state functional network, the default mode network (DMN), whereas the other two are considered as external, according to the selection given in the work of De Pasquale *et al.* [17]. Our method was applied to estimate the structure of the fully–connected brain networks at different time scale resolutions. A great attention was devoted to test the correlation significance by means of two different approaches: the first one assumed as a null hypothesis that the sequences producing the correlation values are independent and identically distributed Gaussian white noise sources; the second one was based on the use of signal surrogates, starting from a much more realistic assumption, namely that each pair of sequences is generated by two independent noise sources with the same distribution of amplitudes and approximately the same power spectrum. Thanks to the larger conservativity of the second hypothesis, the surrogates method has been chosen as the best one to determine the significance of the correlation.
The resulting network structure is defined by means of the selection of four parameter values: the level of significance α, the efficiency η_0 (the amount of windows significantly correlated given a certain temporal resolution W_0), and two ranking parameters, R_1 and R_2, used to merge the results obtained from the whole dataset in a single average behavior. The possibility to tune these parameters gives a great versatility to the network reconstruction, which can be adjusted according to the conservativity requirements one wants to adopt.

In the case of MEG signals, once the functional fully–connected networks were estimated at different time scale resolutions, they were compared to identify the best observation window at which the network dynamics can be highlighted. The resulting best time scale of observation was $\sim$ 30 s, in line with the results present in the scientific literature.
The same method was also applied to meteorological time series to possibly assess wind circulation networks in the Trentino region. Although this study is preliminary, the first results identify an interesting clusterization of the meteorological stations used in the analysis, that seems to be correlated to their geographical positions in terms of latitude and altitude.

As emphasized many times in this thesis, the statistical method developed in this work has many "degrees of freedom" in terms of general applicability, temporal analysis and parameters tuning. All these characteristics makes it easily to extend to other kind of issues. One of the major problems that is still waiting for a clear answer is the assessment of the times series stationarity. It was only mentioned during this thesis because it was not in the scope of this work to address the problem. However, it is an important question even in the study of functional brain connectivity. In recent years, thanks to the great contribution of MEG in this field in terms of unparalleled temporal resolution, many works observed a non–stationarity behavior of resting state networks [17, 38, 55]. This result was hard to achieve by only using fMRI acquisition, because of its poor temporal resolution. The method described in this thesis can be applied to further investigate this problem, thanks to its capability to estimate correlation at different time–scale resolutions. Moreover, another interesting application can be the analysis of correlations at different time lags: this allows to investigated the directionality of the links, describing the flux of information through the network and the dependences between the nodes. This last observation applies in general to any kind of system, even the climatic one, where the "communication time" between distant stations are probably not simultaneous. In this case, the use of a time–lag in correlation analysis can give many information about the effective connectivity between the geographical locations and also provide some hints about system evolution. Finally, in both the case studies proposed in this work, a further extension of the analysis can be performed, for example by increasing the size of the dataset and the set of nodes considered, within the limits of the computational burden. Another kind of development can be the observation of other human brain states and functional networks, whereas, in the case of the climate, it can be interesting exploit the information given by other observables to identify the network structure, as the wind direction.

Bibliography

[1] See https://db.humanconnectome.org/ for public research data concerning the human brain.

[2] J. W. Bales, R. H. Bonow, and R. G. Ellenbogen. "Closed Head Injury". In: *Principles of Neurological Surgery (Fourth Edition)*. Ed. by R. G. Ellenbogen, L. N. Sekhar, N. D. Kitchen, and H. B. da Silva. Fourth Edition. Philadelphia: Elsevier Inc., 2018, 366 –389.e4. ISBN: 978-0-323-43140-8. DOI: https://doi.org/10.1016/B978-0-323-43140-8.00025-1. URL: http://www.sciencedirect.com/science/article/pii/B9780323431408000251.

[3] Soutir Bandyopadhyay, Carsten Jentsch, and Suhasini Subba Rao. "A Spectral Domain Test for Stationarity of Spatio-Temporal Data". In: *Journal of Time Series Analysis* 38.2 (2017), pp. 326–351. DOI: 10.1111/jtsa.12222. URL: https://onlinelibrary.wiley.com/doi/abs/10.1111/jtsa.12222.

[4] M. Barreiro, A. C. Marti, and C. Masoller. "Inferring long memory processes in the climate network via ordinal pattern analysis". In: *Chaos: An Interdisciplinary Journal of Nonlinear Science* 21.1 (2011), p. 013101. DOI: 10.1063/1.3545273. eprint: https://doi.org/10.1063/1.3545273. URL: https://doi.org/10.1063/1.3545273.

[5] E. Barzegaran and M. G. Knyazeva. "Functional connectivity analysis in EEG source space: The choice of method." In: *PloS one* 12 (7 2017), e0181105. DOI: https://doi.org/10.1371/journal.pone.0181105.

[6] Y. Berezin, A. Gozolchiani, O. Guez, and S. Havlin. "Stability of Climate Networks with Time". In: *Scientific Reports* 2.666 (2012), pp. 1–8. DOI: 10.1038/srep00666.

[7] B. Biswal, F. Zerrin Yetkin, V. M. Haughton, and J. S. Hyde. "Functional connectivity in the motor cortex of resting human brain using echo-planar mri". In: *Magnetic Resonance in Medicine* 34.4 (1995), pp. 537–541. DOI: 10.1002/mrm.1910340409. URL: https://onlinelibrary.wiley.com/doi/abs/10.1002/mrm.1910340409.

[8] N. Boers, B. Goswami, A. Rehinwalt, B. Bookhagen, B. Hoskins, and J. Kurths. "Complex networks reveal global pattern of extreme-rainfall teleconnections". In: *Nature* 566 (2019), pp. 373–377. DOI: https://doi.org/10.1038/s41586-018-0872-x.

[9] G. Bohm and G. Zech. *Introduction to Statistics and Data Analysis for Physicists*. Verlag Deutsches Elektronen-Synchrotron, 2010. DOI: https://10.3204/DESY-BOOK/statistics. URL: http://www-library.desy.de/elbook.html.

[10] S. Braeutigam. "Magnetoencephalography: fundamentals and established and emerging clinical applications in radiology". In: *ISRN radiology* (2013), p. 529463. DOI: 10.5402/2013/529463.

[11] J. W. Britton, L. C. Frey, J. L. Hopp, P. Korb, M. Z. Koubeissi, W. E. Lievens, E. M. Pestana-Knight, and E. K. St. Louis. *Electroencephalography (EEG): An Introductory Text and Atlas of Normal and Abnormal Findings in Adults, Children, and Infants*. Ed. by L. C. St. Louis E. K.and Frey. Chicago: American Epilepsy Society, 2016.

[12] M. J. Brookes, M. W. Woolrich, and D. Price. "Magnetoencephalography". In: ed. by S. Supek and C.J. Aine. Berlin: Springer–Verlag, 2014. Chap. An introduction to MEG connectivity measurements.

[13] M. J. Brookes, M. Woolrich, H. Luckhoo, D. Price, J. R. Hale, M. C. Stephenson, G. R. Barnes, S. M. Smith, and P. G. Morris. "Investigating the electrophysiological basis of resting state networks using magnetoencephalography". In: *Proceedings of the National Academy of Sciences* 108.40 (2011), pp. 16783–16788. ISSN: 0027-8424. DOI: 10.1073/pnas.1112685108. URL: https://www.pnas.org/content/108/40/16783.

[14] R. B. Buxton. "The physics of functional magnetic resonance imaging (fMRI)". In: *Reports on progress in physics.* 76 (9 2013), p. 096601. DOI: 10.1088/0034-4885/76/9/096601.

[15] D. Cohen. "Magnetoencephalography: Detection of the Brain's Electrical Activity with a Superconducting Magnetometer". In: *Science* 175.4022 (1972), pp. 664–666. ISSN: 0036-8075. DOI: 10.1126/science.175.4022.664. eprint: https://science.sciencemag.org/content/175/4022/664.full.pdf. URL: https://science.sciencemag.org/content/175/4022/664.

[16] D. Cohen, E. A. Edelsack, and J. E. Zimmerman. "Magnetogram taken inside a shielded room with a superconducting point-contact magnetometer". In: *Applied Physics Letters* 16.7 (1970), pp. 278–280. DOI: 10.1063/1.1653195. eprint: https://doi.org/10.1063/1.1653195. URL: https://doi.org/10.1063/1.1653195.

[17] F. de Pasquale, S. Della Penna, A. Z. Snyder, C. Lewis, D. Mantini, L. Marzetti, P. Belardinelli, L. Ciancetta, V. Pizzella, G. L. Romani, and M. Corbetta. "Temporal dynamics of spontaneous MEG activity in brain networks". In: *Proc. Natl. Acad. Sci.* 107.13 (2010), pp. 6040–6045. DOI: 10.1073/pnas.0913863107.

[18] M. Demuru, A. A. Gouw, A. Hillebrand, C. J. Stam, B. W. van Dijk, P. Scheltens, B. M. Tijms, E. Konijnenberg, M. ten Kate, A. den Braber, D. J. A. Smit, Boomsma D. I., and P. J. Visser. "Functional and effective whole brain connectivity using magnetoencephalography to identify monozygotic twin pairs". In: *Scientific Reports* 7 (2017), p. 9685. DOI: https://doi.org/10.1016/j.neuron.2013.10.017.

[19] J. F. Donges, Y. Zou, N. Marwan, and J. Kurths. "Complex networks in climate dynamics". In: *EPL (Europhysics Letters)* 87.4 (2009), p. 48007. DOI: 10.1209/0295-5075/87/48007. URL: https://doi.org/10.1209%2F0295-5075%2F87%2F48007.

[20] J. F. Donges, Y. Zou, N. Marwan, and J. Kurths. "The backbone of the climate network". In: *European Physical Journal Special Topics* 174 (2009), pp. 157–179. DOI: 10.1209/0295-5075/87/48007. URL: https://doi.org/10.1140/epjst/e2009-01098-2.

[21] I. Ebert-Uphoff and Y. Deng. "A new type of climate network based on probabilistic graphical models: Results of boreal winter versus summer". In: *Geophysical Research Letters* 39.19 (2012). DOI: 10.1029/2012GL053269. URL: https://agupubs.onlinelibrary.wiley.com/doi/abs/10.1029/2012GL053269.

[22] R. L. Fagaly. "Superconducting quantum interference device instruments and applications". In: *Review of Scientific Instruments* 77.10 (2006), p. 101101. DOI: 10.1063/1.2354545. eprint: https://doi.org/10.1063/1.2354545. URL: https://doi.org/10.1063/1.2354545.

[23] P. Fransson. "Spontaneous low-frequency BOLD signal fluctuations: An fMRI investigation of the restingstate default mode of brain function hypothesis". In: *Hum. Brain Mapp.* 26.1 (2005), pp. 15–29.

[24] P. Fransson and G. Marrelec. "The precuneus/posterior cingulate cortex plays a pivotal role in the default mode network: Evidence from a partial correlation network analysis". In: *NeuroImage* 42.3 (2008), pp. 1178 –1184. ISSN: 1053-8119. DOI: https://doi.org/10.1016/j.neuroimage.2008.05.059. URL: http://www.sciencedirect.com/science/article/pii/S1053811908007283.

[25] P. Garcés, E. Pereda, J. A. Hernández-Tamames, F. Del-Pozo, F. Maestú, and J. À. Pineda-Pardo. "Complex relationship between BOLD signal and synchronization/desynchronization of human brain MEG oscillations". In: *Human Brain Mapping* 28.9 (2007), pp. 805–816. DOI: 10.1002/hbm.20322. URL: https://onlinelibrary.wiley.com/doi/abs/10.1002/hbm.20322.

[26] M. Gelbrecht, N. Boers, and J. Kurths. "A complex network representation of wind flows". In: *Chaos* 27.3 (2017), p. 035808.

[27] A. Gozolchiani, S. Havlin, and K. Yamasaki. "Emergence of El Niño as an Autonomous Component in the Climate Network". In: *Phys. Rev. Lett.* 107 (14 2011), p. 148501. DOI: 10.1103/PhysRevLett.107.148501. URL: https://link.aps.org/doi/10.1103/PhysRevLett.107.148501.

[28] A. Gozolchiani, K. Yamasaki, O. Gazit, and S. Havlin. "Pattern of climate network blinking links follows El Niño events". In: *EPL (Europhysics Letters)* 83.2 (2008), p. 28005. DOI: 10.1209/0295-5075/83/28005. URL: https://doi.org/10.1209%2F0295-5075%2F83%2F28005.

[29] O. Guez, A. Gozolchiani, Y. Berezin, Y. Wang, and S. Havlin. "Global climate network evolves with North Atlantic Oscillation phases: Coupling to Southern Pacific Ocean". In: *EPL (Europhysics Letters)* 103.6 (2013), p. 68006. DOI: 10.1209/0295-5075/103/68006. URL: https://doi.org/10.1209%2F0295-5075%2F103%2F68006.

[30] O. C. Guez, A. Gozolchiani, and S. Havlin. "Influence of autocorrelation on the topology of the climate network". In: *Phys. Rev. E* 90 (6 2014), p. 062814. DOI: 10.1103/PhysRevE.90.062814. URL: https://link.aps.org/doi/10.1103/PhysRevE.90.062814.

[31] D. A. Gusnard and M. E. Raichle. "Searchin for a baseline: Functional imaging and resting human brain". In: *Nature* 2 (2001), pp. 685–694. URL: https://www.nature.com/reviews/neuro.

[32] M. Hämäläinen, R. Hari, R. J. Ilmoniemi, J. Knuutila, and O. V. Lounasmaa. "Magnetoencephalography: theory, instrumentation, and applications to noninvasive studies of the working human brain". In: *Rev. Mod. Phys.* 65 (2 1993), pp. 413–497. DOI: 10.1103/RevModPhys.65.413.

[33] A. Hashizume and N. Hironaga. "Clinical Applications of Magnetoencephalography". In: ed. by S. Tobimatsu and R. Kakigi. Japan: Springer, 2016. Chap. Principles of Magnetoencephalography. DOI: 10.1007/978-4-431-55729-6_1.

[34] D. J. Heeger, A. C. Huk, W. S. Geisler, and D. G. Albrecht. "Spikes versus BOLD: what does neuroimaging tell us about neuronal activity?" In: *Nature Neuroscience* 3 (2000), pp. 631 –633. DOI: https://doi.org/10.1038/76572.

[35] R. Hegger, H. Kantz, and T. Schreiber. "Practical implementation of nonlinear time series methods: The TISEAN package". In: *Chaos* 9.2 (1999), pp. 413–435.

[36] R. Hindriks, M. H. Adhikari, Y. Murayama, M. Ganzetti, D. Mantini, N. K. Logothetis, and G. Deco. "Can sliding-window correlations reveal dynamic functional connectivity in resting-state fMRI?" In: *NeuroImage* 127 (2016), pp. 242 –256. ISSN: 1053-8119.

[37] R. C. Jaklevic, J. Lambe, A. H. Silver, and J. E. Mercereau. "Quantum Interference Effects in Josephson Tunneling". In: *Phys. Rev. Lett.* 12 (7 1964), pp. 159–160. DOI: 10.1103/PhysRevLett.12.159. URL: https://link.aps.org/doi/10.1103/PhysRevLett.12.159.

[38] D. T. Jones, P. Vemuri, M. C. Murphy, J. L. Gunter, M. L. Senjem, M. M. Machulda, S. A. Przybelski, Gregg B. E., K. Kantarci, D. S. Knopman, B. F. Boeve, R. C. Petersen, and C. R. Jr. Jack. "Non-stationarity in the "resting brain's" modular architecture". In: *PLoS One* 7.6 (2012), e39731. DOI: 10.1371/journal.pone.0039731. URL: https://journals.plos.org/plosone/article?id=10.1371/journal.pone.0039731.

[39] Heller L. and Volegov P. "Magnetoencephalography". In: ed. by S. Supek and C.J. Aine. Berlin: Springer–Verlag, 2014. Chap. An introduction to MEG connectivity measurements.

[40] Neural Computational Lab. URL: http://www.dendrites.org/synthetic-neocortical-circuit/.

[41] Y. H. Lee and K. Kim. "Magnetoencephalography". In: ed. by S. Supek and C.J. Aine. Berlin: Springer–Verlag, 2014. Chap. Instrumentation for Measuring MEG Signals.

[42] Qinglei Li and Fu Zuntao. "Permutation entropy and statistical complexity quantifier of nonstationarity effect in the vertical velocity records". In: *Phys. Rev. E* 89 (1 2014), p. 012905. DOI: 10.1103/PhysRevE.89.012905. URL: https://link.aps.org/doi/10.1103/PhysRevE.89.012905.

[43] N. K. Logothetis. "What we can do and what we cannot do with fMRI". In: *Nature* 453 (2008), 869–878. DOI: https://doi.org/10.1038/nature06976.

[44] E. N. Lorenz. "Deterministic nonperiodic flow". In: *Journ Atm Science* 20 (1963), pp. 130–141.

[45] E. N. Lorenz. "The predictability of a flow which possesses many scales of motion". In: *Tellus* 21.3 (1969), pp. 289–307. DOI: 10.1111/j.2153-3490.1969.tb00444.x. URL: https://onlinelibrary.wiley.com/doi/abs/10.1111/j.2153-3490.1969.tb00444.x.

[46] N. Malik, N. Marwan, and J. Kurths. "Spatial structures and directionalities in Monsoonal precipitation over South Asia". In: *Nonlin. Processes Geophys.* 17 (2010), pp. 371–381. URL: https://doi.org/10.5194/npg-17-371-2010.

[47] M. Mattia, S. Ferraina, and P. Del Giudice. "Dissociated multi-unit activity and local field potentials: A theory inspired analysis of a motor decision task". In: *NeuroImage* 52.3 (2010). Computational Models of the Brain, pp. 812 –823. ISSN: 1053-8119. DOI: https://doi.org/10.1016/j.neuroimage.2010.01.063. URL: http://www.sciencedirect.com/science/article/pii/S1053811910000856.

[48] J. C. Mazziotta, A. W. Toga, A. Evans, P. Fox, and J. Lancaster. "A Probabilistic Atlas of the Human Brain: Theory and Rationale for Its Development: The International Consortium for Brain Mapping (ICBM)". In: *NeuroImage* 2.2, Part A (1995), pp. 89 –101. DOI: https://doi.org/10.1006/nimg.1995.1012.

[49] Meteotrentino. URL: https://www.meteotrentino.it/index.html#!/content?menuItemDesktop=143.

[50] A. Michael-Titus, P. Revest, and P. Shortland. *The Nervous System*. Churchill Livingstone, 2010.

[51] J. C. Mosher, R. M. Leahy, and P. S. Lewis. "EEG and MEG: forward solutions for inverse methods". In: *IEEE Transactions on Biomedical Engineering* 46.3 (1999), pp. 245–259. ISSN: 0018-9294. DOI: 10.1109/10.748978.

[52] D. R. Mosier. "CHAPTER 1 - Clinical Neuroscience". In: *Neurology Secrets (Fifth Edition)*. Ed. by Loren A. Rolak. Fifth Edition. Philadelphia: Mosby, 2010, pp. 7 –17. ISBN: 978-0-323-05712-7. DOI: https://doi.org/10.1016/B978-0-323-05712-7.00001-5. URL: http://www.sciencedirect.com/science/article/pii/B9780323057127000015.

[53] G. C. O'Neill, E. L. Barratt, B. A. E. Hunt, P. K. Tewarie, and M. J. Brookes. "Measuring electrophysiological connectivity by power envelope correlation: A technical review on MEG methods". In: *Phys. Med. Biol.* 60.21 (2015), R271.

[54] J. M. Palva, S. H. Wang, S. Palva, A. Zhigalov, S. Monto, M. J. Brookes, J.-M. Schoffelen, and K. Jerbi. "Ghost interactions in MEG/EEG source space: A note of caution on inter-areal coupling measures". In: *NeuroImage* 173 (2018), pp. 632 –643. ISSN: 1053-8119. DOI: https://doi.org/10.1016/j.neuroimage.2018.02.032. URL: http://www.sciencedirect.com/science/article/pii/S1053811918301290.

[55] F. de Pasquale, S. Della Penna, A. Z. Snyder, L. Marzetti, V. Pizzella, G. L. Romani, and M. Corbetta. "A cortical core for dynamic integration of functional networks in the resting human brain". In: *Neuron* 74.4 (2012), pp. 753–764. DOI: 10.1016/j.neuron.2012.03.031.

[56] L. Pauling and C. D. Coryell. "The Magnetic Properties and Structure of Hemoglobin, Oxyhemoglobin and Carbonmonoxyhemoglobin". In: *Proceedings of the National Academy of Sciences* 22.4 (1936), pp. 210–216. ISSN: 0027-8424. DOI: 10.1073/pnas.22.4.210. URL: https://www.pnas.org/content/22/4/210.

[57] J. Paz and M. West. *Acute Care Handbook for Physical Therapists*. Saunders, 2013.

[58] APS Physics. *The Ubiquitous SQUID: History and Applications: John Clarke*. 2018. URL: https://www.youtube.com/watch?v=7PJguB3Y8L8&t=182s (visited on 05/14/2018).

[59] V. Pizzella, L. Marzetti, S. Della Penna, F. de Pasquale, F. Zappasodi, and G. L. Romani. "Magnetoencephalography in the study of brain dynamics". In: *Functional Neurology* 29.4 (2014), 241–253.

[60] W. H. Press, S. A. Teukolsky, W. T. Vetterling, and B. P. Flannery. *Numerical Recipes in C*. Cambridge University Press, 1997.

[61] Human Connectome Project. *WU-Minn HCP 1200 Subjects Data Release Reference Manual*. 2017. URL: https://www.humanconnectome.org/storage/app/media/documentation/s1200/HCP_S1200_Release_Reference_Manual.pdf (visited on 03/01/2017).

[62] D. Prêle, M. Piat, L. Sipile, and F. Voisin. "Operating Point and Flux Jumps of a SQUID in Flux-Locked Loop". In: *IEEE Transactions on Applied Superconductivity* 26.2 (2016), pp. 1–5. ISSN: 1051-8223. DOI: 10.1109/TASC.2015.2510606.

[63] M. E. Raichle, A. M. MacLeod, A. Z. Snyder, W. J. Powers, D. A. Gusnard, and G. L. Shulman. "A default mode of brain function". In: *Proc. Natl. Acad. Sci.* 98.2 (2001), pp. 676–682. DOI: 10.1073/pnas.98.2.676.

[64] A. Rheinwalt, N. Boers, N. Marwan, J. Kurths, P. Hoffmann, F.-W. Gerstengarbe, and P. Werner. "Non-linear time series analysis of precipitation events using regional climate networks for Germany". In: *Phys. Rev. Lett.* 111 (13 2013), p. 138501. DOI: 10.1103/PhysRevLett.111.138501. URL: https://link.aps.org/doi/10.1103/PhysRevLett.111.138501.

[65] A. Rheinwalt, N. Boers, N. Marwan, Kurths J., P. Hoffmann, F.-W. Gerstengarbe, and P. Werner. "Non-linear time series analysis of precipitation events using regional climate networks for Germany". In: *Clim. Dyn.* 46.3 (2016), pp. 1065–1074.

[66] T. Schreiber and A. Schmitz. "Improved Surrogate Data for Nonlinearity Tests". In: *Phys. Rev. Lett.* 77 (4 1996), pp. 635–638.

[67] T. Schreiber and A. Schmitz. "Surrogate time series". In: *Physica D* 142.3 (2000), pp. 346 –382.

[68] H. H. Shen. "Core Concept: Resting-state connectivity". In: *Proceedings of the National Academy of Sciences* 112.46 (2015), pp. 14115–14116. ISSN: 0027-8424. DOI: 10.1073/pnas.1518785112. eprint: https://www.pnas.org/content/112/46/14115.full.pdf. URL: https://www.pnas.org/content/112/46/14115.

[69] F. Lopes da Silva. "EEG and MEG: Relevance to Neuroscience". In: *Neuron* 80 (5 2013), pp. 1112–1128. DOI: https://doi.org/10.1016/j.neuron.2013.10.017.

[70] K. Steinhaeuser, N. V. Chawla, and A. R. Ganguly. "Complex networks as a unified framework for descriptive analysis and predictive modeling in climate science". In: *Statistical Analysis and Data Mining: The ASA Data Science Journal* 4.5 (2011), pp. 497–511. DOI: 10.1002/sam.10100. eprint: https://onlinelibrary.wiley.com/doi/pdf/10.1002/sam.10100. URL: https://onlinelibrary.wiley.com/doi/abs/10.1002/sam.10100.

[71] K. Steinhaeuser, A. R. Ganguly, and N. V. Chawla. "Multivariate and multiscale dependence in the global climate system revealed through complex networks". In: *Clim Dyn* 39 (2012), pp. 889–895. DOI: 10.1007/s00382-011-1135-9. URL: https://doi.org/10.1007/s00382-011-1135-9.

[72] A. M. R. Taylor. "Robust Stationarity Tests in Seasonal Time Series Processes". In: *Journal of Business & Economic Statistics* 21.1 (2003), pp. 156–163. DOI: 10.1198/073500102288618856. eprint: https://doi.org/10.1198/073500102288618856. URL: https://doi.org/10.1198/073500102288618856.

[73] A. Tharwat. "Independent component analysis: An introduction". In: *Applied Computing and Informatics* (2018). ISSN: 2210-8327. DOI: https://doi.org/10.1016/j.aci.2018.08.006. URL: http://www.sciencedirect.com/science/article/pii/S2210832718301819.

[74] J. Theiler, S. Eubank, A. Longtin, B. Galdrikian, and J. D. Farmer. "Testing for nonlinearity in time series: the method of surrogate data". In: *Physica D: Nonlinear Phenomena* 58.1 (1992), pp. 77–94. ISSN: 0167-2789. DOI: https://doi.org/10.1016/0167-2789(92)90102-S. URL: http://www.sciencedirect.com/science/article/pii/016727899290102S.

[75] M. J. Thorpy and I. Ahmed. "Chapter 2 - Approach to the Patient with a Sleep Disorder". In: *Therapy in Sleep Medicine*. Ed. by T. J. Barkoukis, J. K. Matheson, R. Ferber, and K. Doghramji. Philadelphia: W.B. Saunders, 2012, pp. 10 –27. ISBN: 978-1-4377-1703-7. DOI: https://doi.org/10.1016/B978-1-4377-1703-7.10002-7. URL: http://www.sciencedirect.com/science/article/pii/B9781437717037100027.

[76] A. A. Tsonis, K. Swanson, and S. Kravtsov. "A new dynamical mechanism for major climate shifts". In: *Geophysical Research Letters* 34.13 (2007). DOI: 10.1029/2007GL030288. eprint: https://agupubs.onlinelibrary.wiley.com/doi/pdf/10.1029/2007GL030288. URL: https://agupubs.onlinelibrary.wiley.com/doi/abs/10.1029/2007GL030288.

[77] A. A. Tsonis and K. L. Swanson. "Topology and Predictability of El Niño and La Niña Networks". In: *Phys. Rev. Lett.* 100 (22 2008), p. 228502. DOI: 10.1103/PhysRevLett.100.228502. URL: https://link.aps.org/doi/10.1103/PhysRevLett.100.228502.

[78] A. A. Tsonis, K. L. Swanson, and P. J. Roebber. "What do networks have to do with climate?" In: *Bull. Am. Meteorol. Soc.* 87.5 (2006), pp. 585–595.

[79] A.A. Tsonis and P.J. Roebber. "The architecture of the climate network". In: *Physica A: Statistical Mechanics and its Applications* 333 (2004), pp. 497 –504. ISSN: 0378-4371. DOI: https://doi.org/10.1016/j.physa.2003.10.045. URL: http://www.sciencedirect.com/science/article/pii/S0378437103009646.

[80] Y. Wang, A. Gozolchiani, Y. Ashkenazy, Y. Berezin, O. Guez, and S. Havlin. "Dominant Imprint of Rossby Waves in the Climate Network". In: *Phys. Rev. Lett.* 111 (13 2013), p. 138501. DOI: 10.1103/PhysRevLett.111.138501. URL: https://link.aps.org/doi/10.1103/PhysRevLett.111.138501.

[81] D. J. Watts and S. H. Strogatz. "Collective dynamics of 'small-world' networks". In: *Nature* 393 (1998), pp. 440 –442. DOI: https://doi.org/10.1038/30918.

[82] G. Winterer, F. W. Carver, F. Musso, V. Mattay, D. R. Weinberger, and R. Coppola. "Complex relationship between BOLD signal and synchronization/desynchronization of human brain MEG oscillations". In: *Human Brain Mapping* 28.9 (2007), pp. 805–816. DOI: 10.1002/hbm.20322. URL: https://onlinelibrary.wiley.com/doi/abs/10.1002/hbm.20322.

[83] A. Witt, J. Kurths, and A. Pikovsky. "Testing stationarity in time series". In: *Phys. Rev. E* 58 (2 1998), pp. 1800–1810. DOI: 10.1103/PhysRevE.58.1800. URL: https://link.aps.org/doi/10.1103/PhysRevE.58.1800.

[84] K. Yamasaki, A. Gozolchiani, and S. Havlin. "Climate Networks around the Globe are Significantly Affected by El Niño". In: *Phys. Rev. Lett.* 100 (22 2008), p. 228501. DOI: 10.1103/PhysRevLett.100.228501. URL: https://link.aps.org/doi/10.1103/PhysRevLett.100.228501.

[85] M. Zeng, M. Zhao, Q. Meng, and J. Wang. "Community structure detection in complex networks for characterizing atmospheric boundary-layer wind speed time series". In: *2016 12th World Congress on Intelligent Control and Automation (WCICA)*. 2016, pp. 2660–2665.